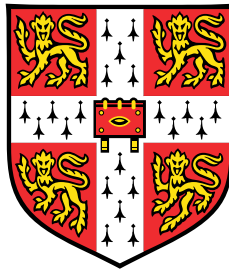# A system-theoretic approach to global and local regulation in neuron morphologies

Saeed M. Aljaberi

Department of Engineering
University of Cambridge

This dissertation is submitted for the degree of
Doctor of Philosophy

St. Edmund's College   March 2021

Declaration

I hereby declare that except where specific reference is made to the work of others, the contents of this dissertation are original and have not been submitted in whole or in part for consideration for any other degree or qualification in this, or any other university. This dissertation is my own work and contains nothing which is the outcome of work done in collaboration with others, except as specified in the text and Acknowledgements. This dissertation contains fewer than 65,000 words including appendices, bibliography, footnotes, tables and equations and has fewer than 150 figures.

<div align="right">

Saeed M. Aljaberi
March 2021

</div>

Abstract

Title: A system-theoretic approach to global and local regulation in neuron morphologies
Author: Saeed M. Aljaberi

Synaptic plasticity is a crucial neuronal mechanism for learning and memory. It allows synapses to change their strength over time. This dissertation focuses on a particular form of synaptic plasticity called synaptic scaling, a homeostatic mechanism that preserves relative synaptic strengths in an activity-dependent manner. Synaptic scaling is fundamental for neuronal stability, regulating other plasticity mechanisms like Hebbian plasticity or long-term potentiation (LTP).

The aims of this dissertation are to explore the implications of synaptic scaling (and other forms of plasticity, such as structural plasticity) on the overall behavior of neurons. This is done using system-theoretic tools and feedback control. We first formulate a biophysical closed loop model of synaptic scaling. We then study how synaptic scaling affect neurons' behavior in both abstract and reconstructed morphologies. This study reveals important tradeoffs between robustness, convergence rate, and accuracy of scaling.

We first look at synaptic scaling as a "global control action" whose main role is to guarantee a steady level of neural activity. We then consider activity-dependent degradation as a "local control action" whose role is to assist the neuron in fine-tuning different desirable spatial concentration profiles. We show that, in extreme scenarios, it can promote a level of competition between synapses that has a destabilizing effect on the overall behavior.

At the methodological level, we use compartmental modeling and we focus on the interaction between feedback and transport, in linear and nonlinear settings. Using classical system-theoretic tools like Bode and Nyquist analysis and singular perturbation arguments, and more recent tools like contraction and dominance theory, we derive parameter ranges under which synaptic scaling is stable and well-behaved (slow regulation), stable and oscillatory (aggressive regulation), and unstable (pathological regulation). We also study the system robustness against static and dynamics uncertainties.

Finally, to understand how different plasticity mechanisms simultaneously affect the neuron behavior, we study synaptic scaling in the presence of activity-dependent growth

(mimicking a structural plasticity mechanism). This is a third layer of control action shaping the neuron morphology. We find that activity-dependent growth improves the neuron's performance when synaptic scaling is insufficient.

إلى ميرة

" و ألقت عصاها، و استقرّ بها النوى
كما قرّ عينًا بالإياب المسافرُ "

Acknowledgements

I'm forever grateful and indebted to my supervisor Fulvio Forni who helped and supported me in almost all aspects of this Ph.D. journey. It has been a privilege to be under the mentorship of a dedicated and passionated researcher. His creativity and rigorous approach to problem solving had a profound impact on my character as a scholar. Fulvio, I learnt a lot from you during these years, and it is unfortunate that this journey has come to an end with so much left to learn from you.

I'm equally indebted to Timothy O'Leary. This dissertation would not have been possible without his guidance. I benifited immensely from his research in homeostasis in neurons. Tim's vision, grasp, and mastery of various topics of neuroscience was truly inspiring and motivational. I'd also like to thank the O'Leary lab, specially Adriano Bellotti. Adriano and I worked closely on the synaptic scaling project, and the numerous discussions we had were very useful to me.

I'm also thankful to members of the Control Group in Cambridge. The group has been a wonderful and an intellectually stimulating environment. Being surrounded by smart and passionate people about research has been a rewarding experience. I specially thank Khalid Laib, Illario Cirillo, Felix A Miranda-Villatoro, and Alberto Padoan for the numerous fun coffee discussions and chats.

My friends in Abu Dhabi have made this journey easier. Sa'd, Abdulrahman, Ahmed, Zain, Nawwaf, Ibrahim, Bader, Ameen, and Ali. Thank you guys.

Above all, I devote the greatest gratitude to my family. My parents, my brothers Saleh, Abdulla, and Mohamed, my sister Alia, my wife Sara, my kids Meera, Suhail, and Mansour. I was only able to do this because of your endless support, encouragement, sacrifices, and unconditional love.

Table of contents

Chapter 1

Introduction

> *"Every object that biology studies is a system of systems."*
>
> Francois Jacob, *The Logic of Living Systems*

The chapter gives a succinct overview of homeostatic synaptic plasticity and scaling. We show why homeostatic plasticity is needed, how it is implemented, and briefly describe the underlying molecular mechanisms. We identify the current gap in the existing literature and how this dissertation, from a control theoretic perspective, fills that gap given the current status of the literature.

1.1   Regulation in biological systems

Regulation gives biological entities their capacity to sustain and cope with endogenous and exogenous perturbations. From cells to organisms, the prevalence of regulatory processes in biology conforms Claude Bernard's quote "all vital mechanisms, however varied, have but one objective, that of maintaining the unity of life functions in the internal medium". He believed that, to survive, living systems need to maintain their *internal milieu* [17, 16]. Regulation in biology, or *homeostasis* as Cannon named it [29], is unique in that it is autonomous, or operates within an organism itself. Homeostatic mechanisms are responsible for keeping certain properties, such as body temperature, near a physiologic set-point despite being in a thermodynamically open state and in a continuous undergo of non-equilibrium conditions.

To understand how homeostatic mechanisms generally occur in biology, we need to look at a biological entity from the perspective of its (abstract) components and relationship [86]. From this perspective, a biological phenomenon emerges from the interconnection of several physiological processes where each entity performs a specific function. Those entities communicate among themselves through signals. At the cellular level, those signals are transmitted by changes in the concentration of substrates or products. At the organism level, this can be done through hormones. The system, or the biological organization, senses the deviations from a set-point and counteract these perturbations by modulating its sub-dynamics to stay around the desired steady-state. This is often implemented in a negative feedback manner. Examples of such include the regulation of gene expression in the *lac* operon [82], movement control in the chemotaxis [49], and glucose levels control in the blood stream.

The aforementioned examples emphasize the fact that, in typical biological systems, deviations from a set point are undesirable and pathological. However, homeostasis of neural firing rates is a unique and an intricate process. The complexity stems from the fact that variability in neural activity is crucial to process and transmit information. Therefore, a typical homeostatic mechanism would strip away the variability that neurons need to function. Alternatively, a neuron homeostatically regulates the *average* neuronal activity over a slower timescale than that of the firing rate. By doing so, the variability in the firing rates are maintained in a range, rather than a fixed set point. This dissertation will deal with homeostasis of average neuronal activity, or firing rates in single neurons.

Before describing in details how such a homeostatic process takes place, we will cover a few facts about neuronal systems. In the next section, we give a brief overview of neurons, from their anatomy to how they communicate and transmit signals. Finally, we focus on the cellular manifestation of the process of learning and memory formation, which is their remarkable *plasticity* property.

1.2   Regulation of neuronal activity

1.2.1   Neurons and synapses

Our brains are highly complex and sophisticated machines that are responsible for arguably the most important aspects of our lives, from forming memories and behavior, to learning a new hobby and making decisions. The building block of brains are networks that are formed by neurons. Neurons constitute the computational units of the brain that process information by receiving, integrating, and transmitting electrochemical signals. This is manifested

by a continuous interaction among roughly 10^9 neurons, comprising approximately 10^{14} neuron-to-neuron connections. Neurons can be easily distinguished from other cells, due to their complex morphologies. Figure 1.1 shows a variety of neurons from different brain areas. Despite their extreme difference in shape, neurons can be anatomically described as a composition of three primary parts: cell body (soma), axon, and dendrites. The dendrites extend from the soma and they are responsible for receiving inputs from other cells, through their axons. Dendrites are the tree-like structures that award neurons their unique intricate geometries, which distinguish them from other cells.
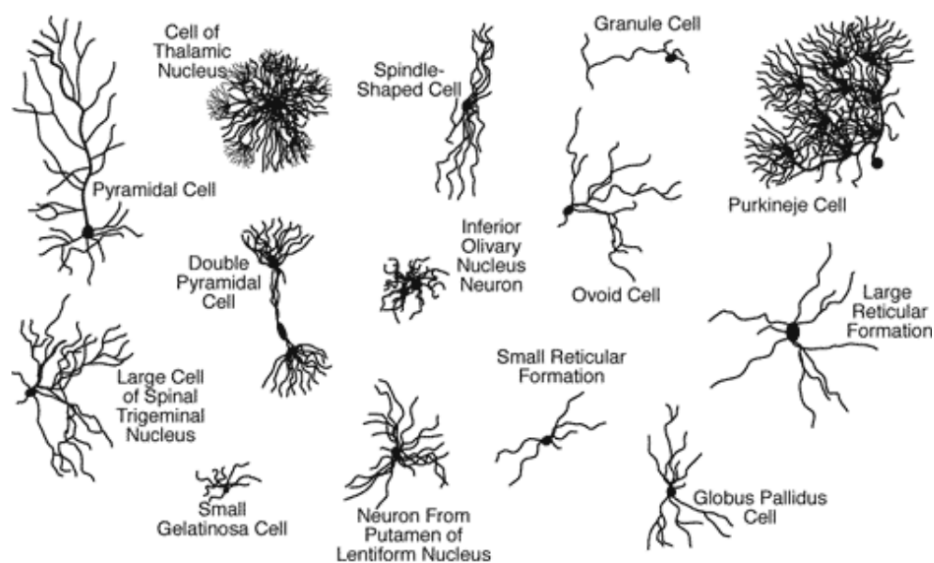
Fig. 1.1 Richness in neuron morphologies demonstrated Ramon y Cajal's drawings.

If we can reduce the brain into a collection of interacting biophysical neural networks, then synapses represent the atoms of this picture. A synapse[1] is a connection which is established by the close contact of an axon of a neuron, called a presynaptic neuron, and a dendrite of another, called a postsynaptic neuron. Synapses bear and transmit signals between cells in an electrochemical fashion. An action potential, or a spike, in the presynaptic terminal causes the vesicles carrying neurotransmitters to attach to the membrane and release those neurotransmitters in the vicinity, or the synaptic cleft. Then the free neurotransmitters diffuse and bind on certain receptors that are attached to the membrane of the postsynaptic cell. If the neurotransmitter is excitatory, then ions will flow into the cell making it more likely to

---

[1]In this dissertation, we are interested in chemical synapses rather than electrical synapses. In chemical synapses, the information flow is directional and always moves from the presynaptic to postsynaptic neuron.

fire, i.e. send an action potential. Conversely, if the neurotransmitter is inhibitory, then ions will flow out of the cell making it less likely to fire. The process is summarized in Figure 1.2.
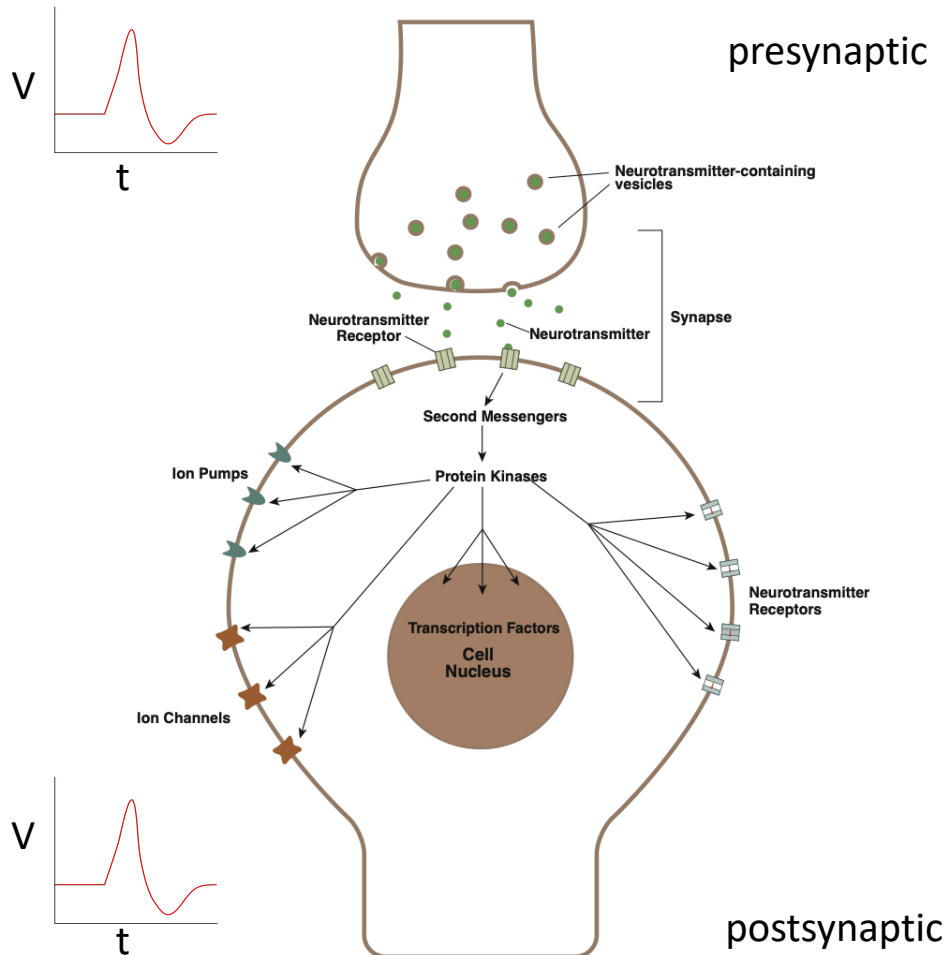
Fig. 1.2 Synaptic transmission (adapted from [67]): an action potential in the presynaptic neuron triggers neurotransmitters release in the synaptic cleft. Those neurotransmitters attach to the receptors on the postsynaptic neuron causing them to open, and ions start to flow in. This causes the postsynaptic neuron to depolarize until it reaches a threshold.

1.2.2 Synaptic plasticity

Synapses are endowed with an utterly important property that has attracted an immense amount of research from neuroscientists; they are *plastic*, i.e. dynamic. This property enables our brain to retain and form new memories, and process information. This is known as *synaptic plasticity*. It refers to the mechanism that modifies the efficacy of synaptic transmission and connection strengths in response to changes in the brain's function due to experience. In other words, synaptic plasticity is an *activity-dependent* phenomenon. In addition, synaptic

plasticity plays an important role in early neuronal circuitry development. Therefore, understanding this phenomenon will reveal insights into the causes of neuropsychiatric disorders. Ultimately this will lead to unveiling the neural basis surrounding numerous aspects of healthy and pathological neuronal functions.

Synaptic plasticity encompasses a number of mechanisms that are inherently different, and those differences are manifested at a number of levels. These mechanisms differ temporally, which led to their categorization into short-term and long-term mechanisms. Short-term plasticity mechanisms last from milliseconds to minutes, and they are thought to be responsible for short-lasting forms of memory, short-term adaptations to sensory inputs, and transient changes in behavioral states. Short-term plasticity primarily depends on short bursts that cause an elevation in calcium levels in the presynaptic terminal that subsequently vary the probability of neurotransmitter release by promoting exocytosis-endocytosis of synaptic vesicles. The coordination of the two processes is crucial for synaptic function. It is short-term plasticity that warrants synapses their filtering characteristics and information processing capabilities. For instance, a synapse with low initial probability release would respond to high-frequency action potential bursts and not with low-frequency bursts, thereby acting as high-pass filters, and vice versa [1].

On the other hand, long-term plasticity mechanisms last from hours to days. They are intimately linked to long-lasting changes in the spatio-temporal patterns in neural circuits, which amounts to the electro-physiological manifestation of information storage. Under this category of plasticity comes metaplasticity, which can be (crudely) understood as "plasticity of plasticity". It does not affect synapse efficacy directly, but rather acts on a higher-level [2], with possible functional roles [32]. One example is the shifts in long-term potentiation (LTP) and long-term depression (LTD) thresholds as a result of past activity, as observed in the hippocampus [80, 159]. Figure 1.3 shows how different short- and long-term plasticity mechanisms are related to different forms of memory.

1.2.3 Hebbian plasticity: the need for homeostasis

There happens to be a different classification of plasticity mechanisms that we refer to. We will organize those mechanisms in two groups: Hebbian and homeostatic. In control-theoretic terminology, these are analogous to positive and negative feedback, respectively. This is due to their long-term influence on the neuron's stability, as we will see next.

The most studied forms of Hebbian plasticity mechanisms are LTP and LTD. The first property of this class of plasticity is that they are input-specific, i.e. they take place locally as a result of correlated firing between pre and postsynaptic neurons, or more famously, "Cells that fire together, wire together" [74]. The positive feedback nature reflects the fact
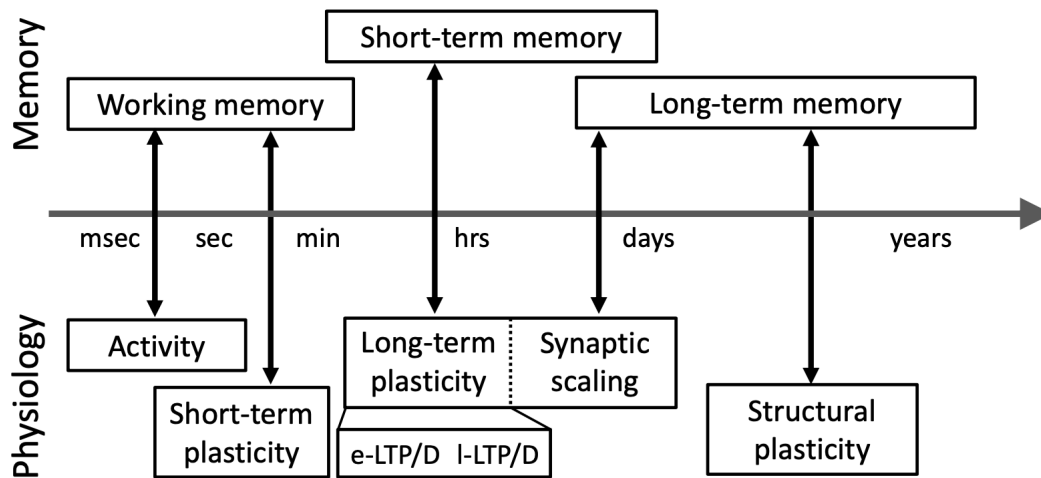
Fig. 1.3 Synaptic plasticity and memory retention: different plasticity mechanisms constitute the physiological bases for various types of memory. Taken from [146].

that strengthened synapses gets excessively stronger, and weakened synapses gets weaker. If this cycles continues, then it leads to runaway (unstable) dynamics. The physiological manifestation of this is hyperexcitability for LTP, and quiescence for LTD.

Thus, a number of compensatory and regulatory mechanisms have been theorized to add a stabilizing effect to mitigate the undesired instability associated with Hebbian plasticity. A homeostatic, compensatory mechanism is needed to keep the overall neuron activity within a functional range, which is achieved by implementing a negative feedback mechanism. This is schematically summarized in Figure 1.4.

Homeostatic plasticity can be employed in two different ways, intrinsically and synaptically [149]. An intrinsic mode of homeostatic plasticity involves varying the distribution of voltage-gated ion channels, thereby shifting the relationship between synaptic input and firing rate [54, 40, 150]. A synaptic homeostatic mechanism, on the other hand, involves the adjustment of synaptic strengths in indivisual synapses with the goal to maintain stability by averaging the neuronal firing rates [151–153]. The bidirectional change in synaptic strength can happen either by controlling the presynaptic neurotransmitter release, or postsynaptic neurotransmitter receptors. In this dissertation we will focus on postsynaptic homeostatic plasticity.
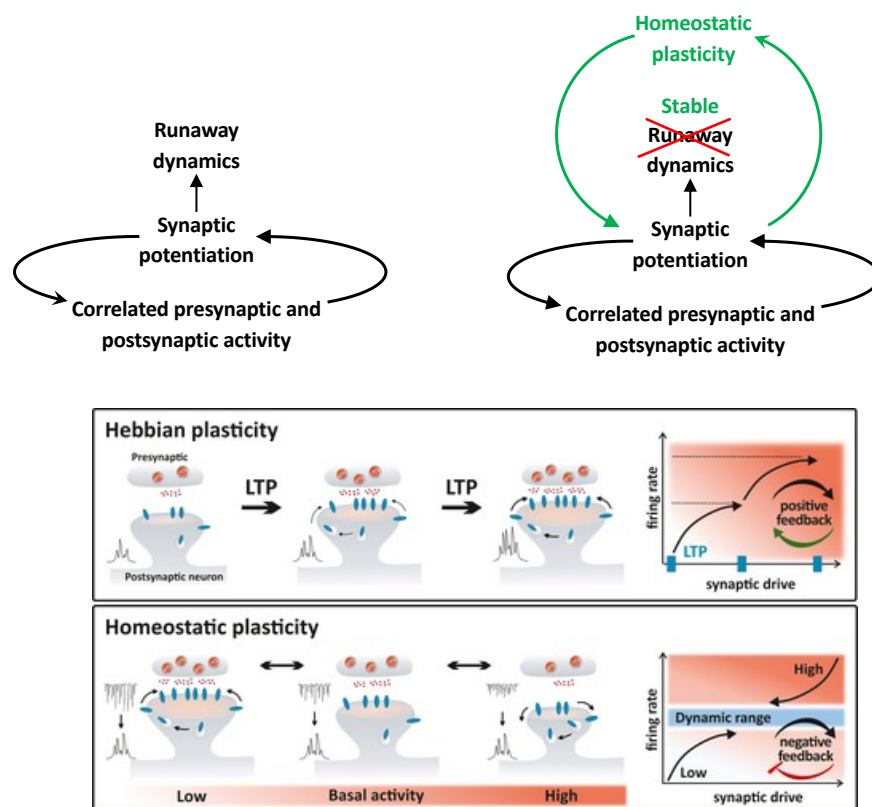
Fig. 1.4 Synaptic scaling maintains stability: A persistent activity leads to runaway dynamics without synaptic scaling (left), while on the other hand, the presence of homeostatic scaling keeps the network stable by maintaining the average activity in a dynamic range, which is achieved by up- or down-regulating the concentration of synaptic molecules (bottom). Bottom figure taken from [54].

1.2.4   Homeostatic synaptic scaling

Synaptic scaling [151, 153] is the most studied form of postsynaptic homeostatic plasticity mechanisms. It globally scales up or down all the synapses in response to variations in the overall set-point [153]. This is achieved by adjusting the strength of individual synapses in response to prolonged changes in parts of the network. In comparison to Hebbian plasticity, LTP and LTD for instance, synaptic scaling operates at slower timescales [32]. Synaptic scaling exists in two forms. The first one, called subtractive, occurs when the synapses are adjusted by the same amount. The second one, called multiplicative, occurs when synapses are adjusted proportionally to their strength.

The pivotal role of synaptic scaling as a stabilizing mechanisms is noticeable when considering LTP and LTD as the only activity-dependent mechanism present in the network. As we saw before, without synaptic scaling or other homeostatic mechanism present, a neural network is destined to either epileptogenic excitation or complete quiescence. One crucial characteristic of synaptic scaling is that it takes place at the neuron level, unlike LTP and LTD [32]. This gives synaptic scaling a *global* influence. This is schematically portrayed in Figure 1.5.

1.2.5   Molecular mechanism

What are the biological mechanisms that underly synaptic scaling? In other words, how is this phenomena implemented physiologically? Experimental studies revealed that glutamate receptors, and in particular the α-amino-3-hydroxy-5-methyl-4-isoxazolepropionic acid (AMPA) receptor (AMPAR) type, play an important role [152, 100, 120]. A plethora of *in vivo* and *in vitro* studies reported a bidirectional activity-dependent change of functional AMPAR concentration. For example, studies of the visual cortex showed experience-dependent scaling of glutamergic synaptic response, where AMPA receptors increased during deprivation of light, and decreased during light exposure [39, 61]. Another set of experimental studies showed that activity-dependent manipulations also affected both AMPA and NMDA receptors [123, 153, 160].

Synaptic scaling is a cell-autonomous process, where a neuron's senses perturbations to its activity. This is modulated by variations in the depolarization and somatic calcium influx which in turn triggers a signaling pathway that changes the accumulation of AMPA receptors in the synapse [81] (Figure 1.6a). However, the complete picture and the identification of molecules involved in the scaling of AMPA receptors remains unclear [149, 124, 54]. An example of other experimentally recognized scaling molecules are neurotrophin brain-derived neurotrophic factor (BDNF), the immediate early gene *Arc*, the cytokine TNFα, and the
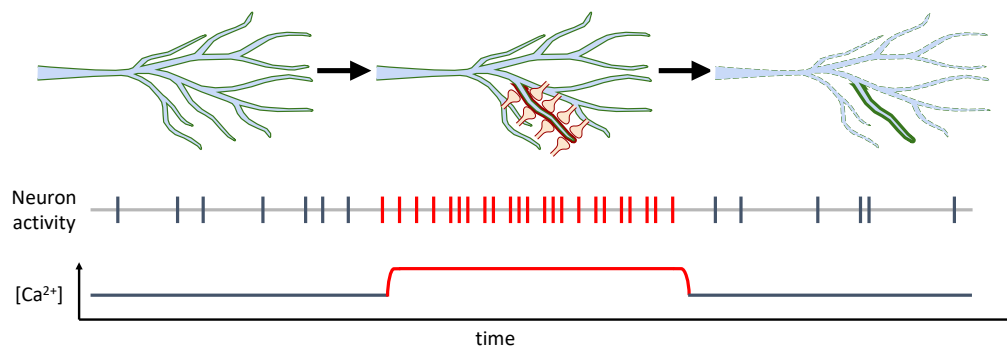
Fig. 1.5 Synaptic scaling is a global phenomena: after potentiation, synaptic scaling down-regulates the rest of the network in order to compensate for the increase in activity. The green line enclosing the neuron represents the synaptic strength of synapses, The bold line represents an increase in synaptic strength, and the dashed line represents a decrease in synaptic strength.

associated molecular mechanism and signaling pathways are numerous (Figure 1.6b). More comprehensive accounts of this subject can be found in [149, 124, 54] and references therein.

1.2.6   Intracellular Transport

It comes as no surprise that the regulation of neuronal activity involves a myriad of physiological processes that vary both in their spatiotemporal scale and mechanism. Either in a cell or a network of cells, the change in efficacy of synapses depends on the movements of a number of molecules such as mRNA, ion channels, and receptors. Therefore, the neurons depend on a functional transportation apparatus to successively regulate their neuronal activity in a healthy manner. In fact, neurological disorders have been associated with impaired transport mechanisms, such as Alzheimer's disease and other dementias [38]. Thus, a healthy neuron requires a functional trafficking system that is able to transport different molecular cargo to their demand sites [3].

Different vesicles and proteins vary in size, and also their transport mechanism. Intracellular transport can be performed passively, or actively. Diffusion is an example of passive transport as it depends on the concentration gradient, i.e. molecules move from higher to lower concentration regions. This form of transport takes place in the cell cytoplasm or across the cell membrane. In neurons, and more specifically in the context of plasticity, diffusion is too slow to deliver the proteins in time. Active transport, however, is significantly faster for long distances than diffusion and is believed to be responsible for axonal and dendritic transport.
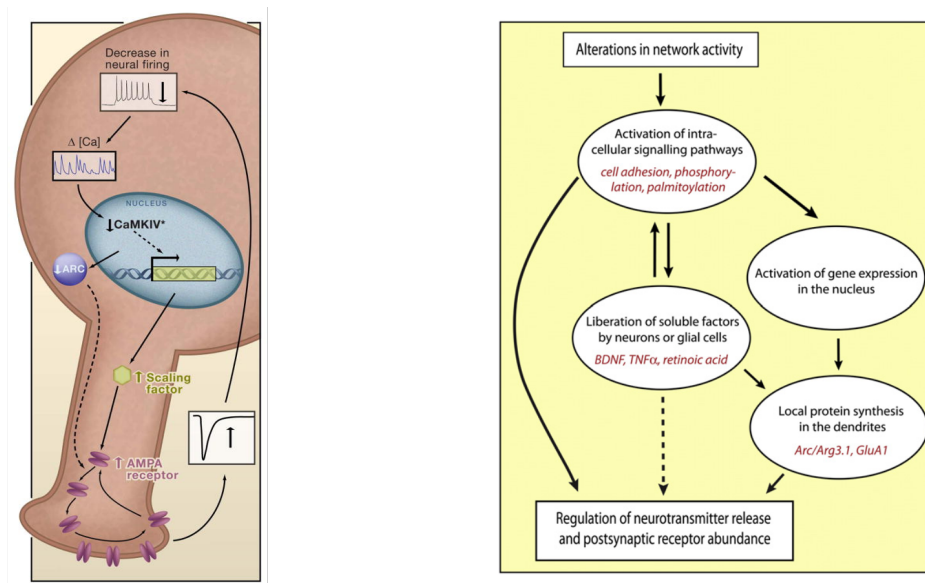
(a) Regulation of synaptic strength.

(b) Molecular mechanisms underlying plasticity.

Fig. 1.6 Synaptic scaling is a biological complex process that depends on alteration in network activity: AMPA receptors (and potentially other scaling factors) trafficking is responsible for the variations in synaptic strength (left, taken from [151]). The molecular mechanisms of homeostatic plasticity involves a number physiological complex processes (right, taken from [124]).

Contrary to passive transport, active transport is significantly faster and metabolically active, i.e. it requires cellular energy in the form of ATP. It is mediated by special cytoskeletal structures called microtubule and actin filaments, shown in Figure 1.7. Actin serves as a track for myosin, a family of motor-protein. Actin filaments exist in high concentration near synapses and they play an important role during synaptic function and plasticity. For instance, interfering with myosin II in the postsynaptic site caused morphological changes to the AMPA receptor submit Glu A1 [131], and loss of myosin VI was found to be correlated to reductions in synapse numbers [119]. Importantly, myosin is heavily involved in the postsynaptic trafficking and regulation of AMPA receptor [119, 113, 165]. A more detailed overview of the different myosin families with their respective roles in synaptic morphology and function can be found in this review [93].

While actin filaments are responsible for the short-distanced trafficking, i.e. from the intracellular dendritic space to the spine neck or head, microtubules are responsible for the bulk transport. Microtubules have plus-ends and minus-ends, and this provides the directionality to the main motor-protein families: dynein and kinesin. Dynein is a minus-end directed motor and kinesin is a plus-end directed motor. This will have nontrivial implications that will differentiate axonal from dendritic transport.
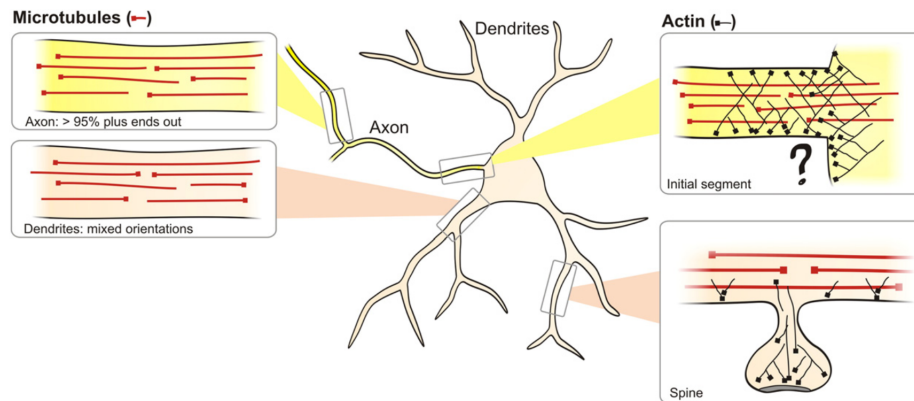
Fig. 1.7 Cytoskeletal organization of the neuron: microtubules are almost uniformly oriented in axons, and mixed on dendrites. Actin filaments are rich near synapses (taken from [88]).

Beside their geometry, axons differ from dendrites in their microtubulal organization, too. In axons, microtubules are uniformly oriented with plus-ends directed away from the soma. In axons, kinesins and dyneins thus generally move in different directions (anterograde and retrograde, respectively). Kinesins are largely responsible for transporting cargo to the periphery, whereas dyneins carry cargo toward the soma for recycling [110, 71]. Dendrites differ in that microtubules have mixed orientation. In dendrites, all motor protein families carry cargo toward or away from the soma. Two distinct hypotheses have been proposed regarding directed transport in dendrites. One hypothesis suggests that motors act cooperatively, where the motor-cargo complex responds to stimuli for forward movement, backward movement, attachment, and detachment [110, 71]. The second hypothesis, called the tug-of-war model of bidirectional transport describes both active kinesins and dyneins, and the cargo moves in the direction of the dominant motor type. Net movement thus depends on the number of kinesins and dyneins motors attached to the cargo, and quantitative predictions are based on observations of single motor proteins [22]. Both hypotheses predict that the motor-cargo complex experiences bidirectional, stochastic movement [22, 23].

In this dissertation, we will study this active mode transport, but under two different models. In chapters 3-6, we deal with a simple linear model of transport, where we will assign fixed forwards and backward rates. In chapters 7-8, we adapt a nonlinear form of active transport where these rates are state-dependent to reflect more biologically complex phenomena and capture the effects of finite capacities.

1.3   Aims

We have briefly described the anatomy of neurons, how they interact, and the importance of activity regulation. From that short overview, we can make the following observations regarding the regulation of neuronal activity in neurons:

1. Neurons exist in numerous and complex geometries (Figure 1.1).

2. The composition of the different molecular processes that make up neuronal activity regulation in neurons and their interconnection are nontrivial (Figure 1.6).

3. Any long-term change necessary requires, in an activity-dependent manner, a continuous interplay between biosynthesis, transport, and degradation of molecules.

Considering regulation as a requirement that neurons need to fulfill, their morphologies will play a critical role in such a task. Specifically, the transport of molecular cargo over dendritic trees imposes significant constraints on the success of regulation. A number of papers have tackled this from a theoretical and computational viewpoint [161, 148, 21, 45], and revealed a number of interesting observations, from speed-accuracy tradeoffs to competition among synapses. Nevertheless, the work disregards the nature of feedback in synaptic scaling that we anticipate to be of crucial importance and has the capability to alter some of these observations. Using feedback and integral control has proven successful in achieving homeostasis in neuronal systems [117, 28, 96, 136, 63, 25], and biological systems in general. In Table 1.1, we list papers that serve as the starting point of this dissertation.

The central theme of this dissertation is to *understand the role and effects of morphology, and therefore transport, on the problem of homeostasis of average neuronal activity*. To answer this, we split this central theme into the following objectives:

1. *Understanding the effect of real morphologies on synaptic scaling.* Since long-term plasticity mechanisms, including synaptic scaling, require a permanent change of proteins concentration in the synapse, it is only feasible by regulating gene expression. This cycle entails the production, transportation, demand and maintenance of postsynaptic molecules. This poses severe logistical constraints on performance given the complex geometry of dendrites.

2. *Understanding the effect of nonlinearities and timescale.* Dendrites are filled with microtubules and other cytoskeletal structures that keep bombarding trafficked cargo due to the confined space. This requires a nonlinear version of an active transport model to account for crowding and saturation effects. Moreover, what are the consequences of

variations in gene expression rates, i.e. transcription-translation timescales, on synaptic scaling?

3. *Understanding the effect of other activity-dependent phenomena.* Synapses are complex as they run various types of plasticity form simultaneously where each one has its own mechanism, which might pose a challenge to experimental studies and force an undesired oversimplified view [99]. Therefore, to unveil some of the structural properties of synaptic scaling, we study homeostatic synaptic scaling in the presence of other activity-dependent physiological processes, such as degradation and growth.

Table 1.1 Relevant literature

Papers	Summary
Intracellular transport of cargo: [148, 161, 23, 46, 167]	[148]: a simple open-loop neuron model that focuses on endocytosis-excocytosis of receptors into and out of synaptic slots. The model exhibits a multiplicative from of scaling.
	[161]: a mathematical implementation of the *sushi-belt model* [44] that studied transport on real dendritic morphologies. The study reveals a speed-accuracy tradeoff imposed by logistic of linear transport. Fine-tuning of attachment-detachment rates was the mean to spatially vary demand signals.
	[23, 46]: a drift-diffusion PDE model of AMPA receptor transport over $1-$dimensional lines. The solution produces an exponentially decreasing concentration of receptor away from the soma.
	[167]: an ODE version model of *totally asymmetric exclusion process* from statistical physics [125]. The model was used to study mRNA translation.
Use of negative-feedback to achieve regulation: [117, 28, 96, 136, 63, 25]	Use of integrators to regulate ion channels distribution. In these papers, homeostasis was implemented as a negative-feedback mechanism.

1.4   Dissertation outline and associated publications

This dissertation establishes a step towards understanding the burgeoning research area of homeostatic plasticity and regulation in neurons, but rather from a *control and system-theoretic perspective*. We believe this should provide a different perspective to complement existing theoretical and experimental work done on the subject. Firstly, we develop a class of biological mathematical models from first principles. Then, we present a theorem that establishes the conditions under which this class of models is stable. Finally, we study, analyze, and discuss the emergent behaviors and properties that arise by modifying biochemical parameters to mirror different physiologically-relevant settings.

The dissertation is structured in the following way:

- **Chapter 2:** this chapter summarizes the mathematical background needed for the dissertation. We start by justifying the modeling formalism adapted in the dissertation. This chapter largely depends on feedback systems and control. It begins with classical control notions such as transfer functions and Nyquist stability criterion. Then it moves to the recently developed theory of dominance, which is a nonlinear analysis tool that studies systems differentially. The chapter concludes with singular perturbation theory as a technique to study slow-fast systems.

- **Chapters 3-5:** these chapters represent the first contribution of the dissertation. We formulate a biophysical closed loop synaptic scaling model based on the regulation of AMPA receptor synthesis, transport, and insertion, called the **CLSS**. We derive conditions under which the system is exponentially stable. Next, we define relevant performance measures to investigate the effect of arbitrary and biological dendritic trees. The main conclusion is that there is an inevitable tradeoff imposed by the network topology that restricts the performance of the neuron. We define three performance attributes: convergence rate, system robustness, and scaling accuracy. The main message is that a neuron cannot improve one attribute without worsening one or the other two.

  These chapters are the offspring of a fruitful collaboration with my Ph.D. colleague Adriano Bellotti. The collaboration led to the following research materials:

  1. Abstract in the 29th Annual Computational Neuroscience Meeting *CNS*[*]2020 [14].

  2. A preprint for publication to eLife, in preparation.

- **Chapters 6:** from this chapter onwards, we replace parts in the **CLSS** model in order to steer the attention to particular biological processes. This chapter analyzes the effect of activity-dependent degradation on synaptic scaling. The main focus on this chapter is to understand the global-local interplay of different regulation mechanisms. Synaptic scaling is a centralized or global phenomenon that senses the average functional cargo concentration in the network while on the other hand, activity-dependent degradation is a distributed (i.e. takes places locally in individual compartments). The interesting interplay exhibits both a competitive (destabilizing) and cooperative (stabilizing) effect depending on the system parameters.

  This chapter is largely based on a publication to the 24th International Symposium on Mathematical Theory of Networks and Systems (MTNS 2020, peer reviewed) [4].

- **Chapter 7:** in this chapter, we study the effect of nonlinear trafficking on homeostasis, along with variations in the timescale cargo synthesis. Using dominance theory, we break down the regulation regimes into three distinct regimes: nominal, stable and oscillatory, and pathological. Moreover, we derive parameter ranges that respect each regime, and assess the model robustness against static and dynamic uncertainties. We show that the features of the **CLSS** model are generally preserved.

  This chapter is largely based on a publication to the 58th IEEE Conference on Decision and Control (CDC 2019, peer reviewed) [5].

- **Chapters 8:** we study two forms of plasticity simultaneously. In addition to synaptic scaling, we model structural plasticity as activity-dependent growth. Synaptic scaling in the presence of activity-dependent growth improves the neuron's performance significantly, in comparison to a neuron with synaptic scaling alone. This is primarily due to the slow timescale nature of growth processes, which allows it to exhibit a low-filtering characteristic.

  This chapter is largely based on a publication to the 2021 European Control Conference (ECC 2021, peer reviewed) [6].

- **Chapters 9:** this chapter concludes the dissertation. It summarizes the results presented in the previous chapters, and outlines potential extensions and future research directions.

Figure 1.8 shows the hierarchal structure of the dissertation. Chapter 2 equips the reader with the necessary mathematical tools to navigate and access the later chapters.
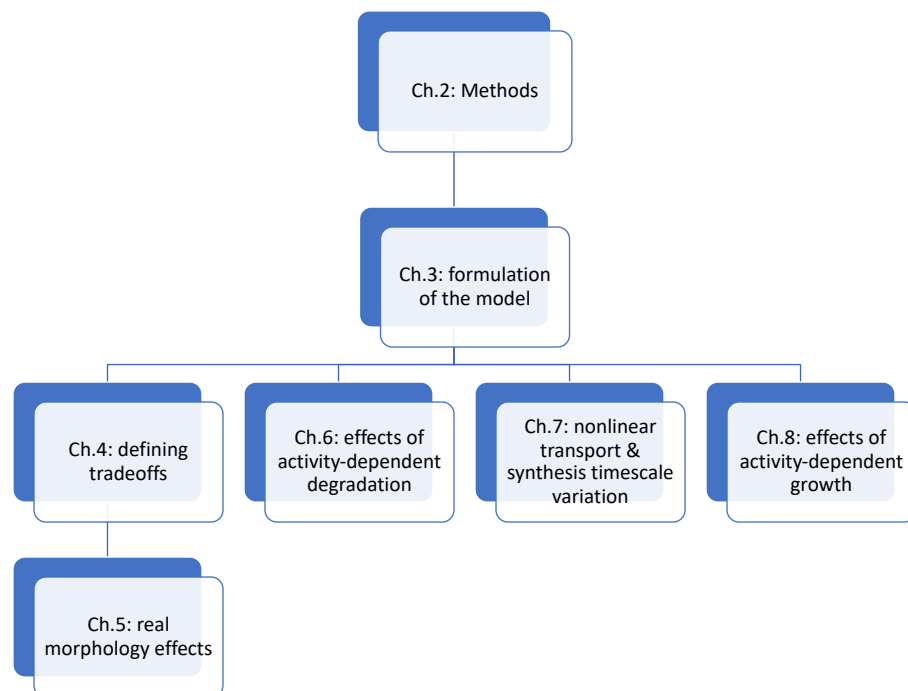
Fig. 1.8 Dissertation roadmap: the main contributions were written and grouped in self-contained, stand-alone chapters or group of chapters. Chapters 4-5 are grouped together, while other chapters deliver independent messages.

Chapter 2

Methods: system theory and feedback control

"But in my opinion, all things in nature occur mathematically."

Rene Decartes

We first justify using deterministic ordinary differential equation as the modeling approach of this dissertation. Next, we introduce the mathematical machinery that will use to study the problem of activity regulation in neurons. This primarily depends on system theory and feedback control. Starting from classical tools such as transfer functions to the novel tools of p-dominance. We conclude with singular perturbation techniques as a mean to study systems with multiple timescales. Along the exposition, we allude to how these different tools will be used.

2.1   Modeling: deterministic compartmental systems

We will be using mathematical models in place of actual neurons, and exploit those models to facilitate intuitions, mimic certain conditions, or test predictions. The set of rules that govern the model, thereby reflecting processes in the real world, are expressed mathematically. To use mathematical models of neurons, we first need to state a few assumptions regarding the modeling formalism and setting.

We use ordinary differential equations (ODEs) to describe the instantaneous change in species concentration. Furthermore, we do this in a deterministic setting. These two choices define the mathematical formalism or stance that we take in this dissertation, and this is justified by embracing the following assumptions:

1. *Continuum hypothesis:* this assumption allows us to treat and measure concentrations of molecules as a continuous quantity, rather than a discrete one. This assumption is justified if molecules number is sufficiently large. If not, a stochastic framework is required.

2. *Well-mixed assumption:* this simply means that the spatial distribution of biological molecules is homogeneous, or uniform. Otherwise, the use of partial differential equations (PDEs) is required to relax this assumption.

There are multiple sources of stochasticity in biological processes. One is the constant buffeting of molecules that gives rise to noise and randomness. Another is the uncertainties associated with the experimental data acquisition. To take into account stochasticity in biological models, we will often study robustness to static and dynamics uncertainties using tools from control theory, that were developed in a deterministic ODE setting. In this context, a system is robust if it is able to preserve its function/property in spite of worst case perturbations

We will be using compartmental models as a framework to study the transport of biological molecules. Compartmental models proved to be successful in studying transportation problems in congestion control, epistemology, and ecology [83, 70, 20, 13, 34, 33, 106]. In compartmental systems, mass balance is used to capture the transport of material between individual compartments. For instance, let $x(t) := [x_1(t) \ldots x_n(t)]^T \in \mathbf{R}^n$ be a compartmental system [1]. Then we can schematically model the exchange of mass between x_i and x_j as shown in Figure 2.1.
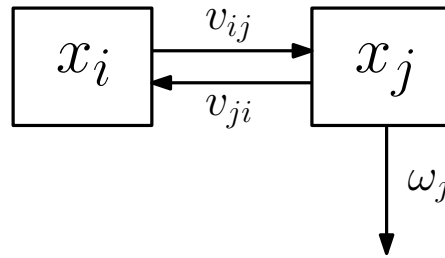
Fig. 2.1 An example of a compartmental system: two compartments showing exchange of mass. Compartment x_j is subject to dissipation.

The exchange of mass between compartments can be linear ($\dot{x} = Ax$) or nonlinear ($\dot{x} = f(x)$). Specifically, v_{ij} and v_{ji} can be constants where they describe a fixed transport rate. Conversely, they can be nonlinear and state-dependent in a way the captures more realistic or biologically plausible situations, such as congestion or finite capacities. Throughout this

---

[1]from now on, we drop the dependence in time, i.e. we write x for $x(t)$.

dissertation, we will implement both scenarios. In both modes, however, the compartmental system is cooperative [137], i.e. A and $\frac{\partial f}{\partial x}$ are positive/Metzler matrices [52]. Systems of that form always converge to an equilibrium, if trajectories are bounded (other behaviors may be present in the system, like oscillations and chaotic attractor, but those are unstable).

In the limit as $n \to \infty$, compartmental systems become diffusion/drift-diffusion partial differential equations. Using $||H||_\infty$ control, and with the proper scaling, we can track at what level of resolution the compartmental system at hand captures the same qualitative behavior as its PDE counterpart. By doing so, we minimize the limitation or gap that arises from the second assumption.

2.2   Classical control theory

2.2.1   From autonomous ODEs to transfer functions

In order to be able to answer the questions laid out in the introduction, we need to dissect the vector x into inputs, states, and outputs. We do so to properly assign biological processes and study them with respect to their functional role. For example, we will often consider biomolecule synthesis as an input, and functional synaptic molecules as the observed species. Therefore, we consider the following representation of dynamical systems:

$$\dot{x} = f(x, u) \tag{2.1}$$
$$y = h(x).$$

Throughout this dissertation, we will use the following terminology: u as input, x as a state, and y as an output. The first part of equation (2.1), $f(x, u)$, describes the evolution of the state x over time, while the second part, $h(x)$, describes the observed or measured signal. The first step is to obtain a linear state-space representation of (2.1). To express nonlinear functions in this form, we take the Taylor series expansion around an operating point, typically the equilibrium. Let (x^*, u^*) be the equilibrium, i.e. $f(x^*, u^*) = 0$. Then we take the Taylor expansion around (x^*, u^*) and truncate the expression after the first term to obtain the following first order approximation

$$\dot{x} := f(x^*, u^*) + \left(\frac{\partial f}{\partial x}\right)\bigg|_{(x=x^*, u=u^*)} (x - x^*) + \left(\frac{\partial f}{\partial u}\right)\bigg|_{(x=x^*, u=u^*)} (u - u^*)$$
$$y := h(x^*) + \left(\frac{\partial h}{\partial x}\right)\bigg|_{(x=x^*, u=u^*)} (x - x^*).$$

Since $f(x^*, u^*) = 0$, the above expression becomes:

$$\dot{\bar{x}} = A\bar{x} + B\bar{u} \qquad (2.2)$$
$$\bar{y} = C\bar{x}$$

where we made the following coordinate change:

$$\bar{x} := (x - x^*), \quad \bar{u} := (u - u^*), \quad \bar{y} := (y - y^*) = y - h(x^*)$$

and the following substitutions:

$$A := \left(\frac{\partial f}{\partial x}\right)\Bigg|_{(x=x^*, u=u^*)}, \quad B := \left(\frac{\partial f}{\partial u}\right)\Bigg|_{(x=x^*, u=u^*)}, \quad C := \left(\frac{\partial h}{\partial x}\right)\Bigg|_{(x=x^*, u=u^*)}.$$

The linearization is justified by Grobman-Hartman Theorem, which states that the *local* behavior of a nonlinear dynamical system near the equilibrium is captured by its linearization around that point [30]. It is important to note that this is a local result and does not necessarily give insight about the global behavior of the nonlinear system far away from its equilibrium. In the next section, we will see how to evade this limitation to study global and non-equilibrium behaviors.

Equations (2.2) are referred to as a *state-space representation*. Lastly, the transfer function in the Laplace domain is obtained by taking the ratio of the Laplace transforms of input and output signals

$$G(s) = \frac{Y(s)}{U(s)} = C(sI - A)^{-1}B. \qquad (2.3)$$

where s is a complex variable, thus G is a complex function. The transfer function as expressed here shows the input-output relationship of the system in the complex plane. Transformation back and forth between time and s domain is common. Notably, although there exists multiple state-space representations, the transfer function is unique. In Chapter 5, we will use this fact to link Rall's equivalent cylinders and reduced-order models to transfer functions.

2.2.2   Nyquist plot and stability margins

In general a process will consist of multiple transfer functions representing different dynamical models and how the signals of each transfer function are related. Figure 2.2a shows a generic block diagram of a controller and a plant, showing a reference signal $R(s)$, error

(a) Block diagram.

(b) A generic Nyquist plot.
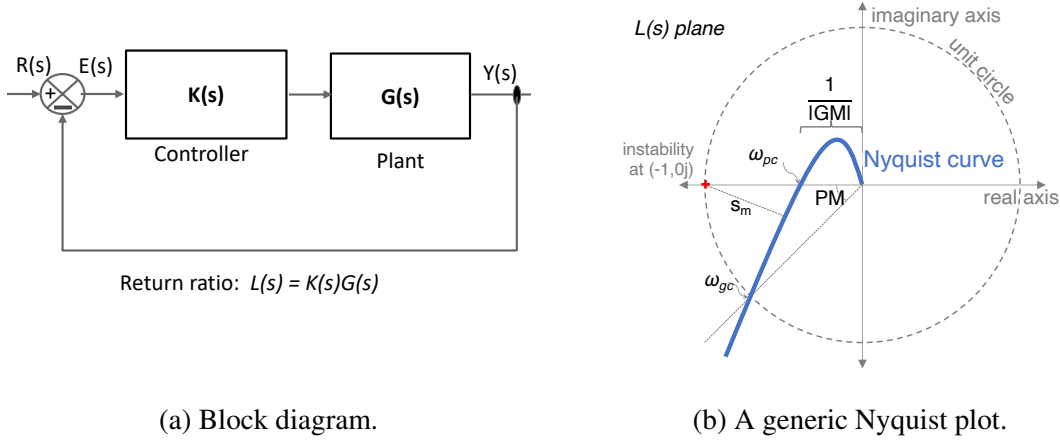
Fig. 2.2 A block diagram showing a controller and a plant in closed loop (left). Nyquist plot and a geometric definition of stability margins (right).

signal $E(s)$, and an output signal $Y(s)$. The goal of feedback is to achieve regulation; in other words, we want the plant output to follow the reference signal, which will drive the error to zero. Feedback guarantees the performance in the presence of parameter uncertainties, disturbances, and unmodeled dynamics.

The return ratio is a transfer function that encompasses all the terms around the loop. For example, the return ratio of the block diagram in Figure 2.2a is $L(s) = K(s)G(s)$. This is also the open-loop transfer function. This important object is crucial in determining the stability and robustness of the closed loop system. We will achieve this via the Nyquist stability criterion.

Before stating the Nyquist stability criterion, we need to obtain the Nyquist curve. This is done in the frequency domain by parameterizing the return ratio into into real $(\mathrm{Re}(L(j\omega)))$ and imaginary $(\mathrm{Im}(L(j\omega)))$ parts plotted on the x- and y-axes, respectively. The result is a Nyquist plot, where a generic one is depicted in Figure 2.2b. Then the stability criterion informally states that if $L(s)$ is asymptotically stable and the Nyquist plot does not encircle $(-1+0j)$, then, the closed loop transfer function $\frac{L(s)}{1+L(s)}$ is asymptotically stable as well. This is stated formally below

Theorem 1 *Let $L(s)$ be an asymptotically stable system, the feedback system is asymptotically stable if and only if the Nyquist diagram does not encircle the $(-1,0j)$ point.*

This is especially powerful since we are able to infer the stability of the closed loop system from information about the open loop one. Moreover, the proximity to the point $(-1+0j)$ will be the fundamental feature in defining margins of stability. This is also relevant

when discussing notions related to performance, such as robustness. This will be one of performance attributes that we will consider.

The gain margin (GM) is the reciprocal of the gain at a phase frequency of -180 degrees. The phase margin (PM) is the difference in phase between the system phase and 180 degrees computed at the point of unity gain. These margins are computed using the following equations:

$$\mathrm{GM} = 20\log\frac{1}{|L(j\omega_{cp})|} \quad \text{(in dB)} \tag{2.4}$$

$$\mathrm{PM} = 180 + \arg\{L(j\omega_{cg})\} \quad \text{(in degrees)}$$

where ω_{cg} is the gain crossover frequency, and ω_{cp} is phase crossover frequency. ω_{cg} is the frequency at which the magnitude of $L(s)$ is unity, while ω_{cp} is the frequency at which the phase angle of $L(s)$ is -180. Stability margins geometrically correspond to the distance between the trace of a transfer function on a Nyquist plot from the point $(-1 + 0j)$, as shown in Figure 2.2b. The stability margin s_m is another robustness measure. It measures the shortest distance of Nyquist plot from the $(-1, 0j)$. It is computed from the sensitivity function, which is obtained from the loop gain $L(s)$ as:

$$S(s) = \frac{1}{1 + L(s)} \tag{2.5}$$

then s_m, or the shortest distance between Nyquist plot and $(-1 + 0j)$ point, is computed from the following relation

$$s_m = \frac{1}{M_s} \tag{2.6}$$

$$\text{where} \quad M_s = \sup_{\omega} |S(j\omega)|.$$

Equation 2.5 provides a single number to measure robustness, unlike the previous case where we needed to keep track of both the gain and phase margins.

Nyquist analysis provides a simple graphical test for stability and robustness of systems. This mitigates a lot of the difficulties caused by the complexity of interconnections between the subdynamics, and their high dimensionality. We will see that these tools will allow us to asses the robustness of a Purkinjie cell, which has a state vector of order 10^3, and with dynamics happening over multiple timescales, with a simple 2-d curve. Frequency-domain tools are primarily used in chapters 3-5.

2.3   Beyond stability: p-dominance analysis

2.3.1   Non-equilibrium behaviors in biology

The biology is rich of systems that are not monostable. For example, a plethora of biological systems can operate in two stable modes, depending on their response to particular inputs. The *lac operon* and toggle switch are examples of systems that exhibit such a motif. Sustained oscillations are another motif in biology where species do not rest at a steady-state concentration, such as *repressilator*. This is also the case in neuronal systems. Conductance-based models are biophysical models that describe the excitability of cells, a highly nonlinear phenomenon. The model can be in equilibrium or a limit cycle, depending on the injected current.

Hence there is a pressing need for an apparatus that has the capacity to analyze systems beyond monostability. To this end, we use differential analysis in order to leverage the existing tools from linear theory. The linearization, which is often used to perform local analysis of nonlinear systems, is used in differential analysis to answer non-local questions about the system behavior.

2.3.2   Differential analysis and p-dominant systems

In what follows, we give a brief summary of the novel tools of dominance theory. The interested reader is referred to [58] for a thorough presentation of the theory.

A *p*-dominant linear system with rate $\lambda \geq 0$ has exactly p slow/dominant modes, whose decay rate is slower than $-\lambda$, and $n-p$ fast decaying modes, where n is the system dimension. The trajectories of the system rapidly converge to a p-dimensional invariant subspace capturing the steady-state of the system. In state space representation $\dot{x} = Ax$, $A \in \mathbb{R}^{n \times n}$, linear *p*-dominance with rate λ is certified by the Lyapunov inequality $A^T P + PA + 2\lambda I < 0$ constrained to symmetric matrices P with inertia $(p, 0, n-p)$, that is, p negative eigenvalues and $n-p$ positive eigenvalues. *p*-dominance can be extended to nonlinear systems of the form $\dot{x} = f(x)$ using the system linearization $\dot{\delta}x = \partial f(x)\delta x$ along arbitrary trajectories [58] ($\partial f(x)$ is the Jacobian of f).

Definition 1 A nonlinear system $\dot{x} = f(x)$ is *p*-dominant with rate $\lambda \geq 0$ if there exists a symmetric matrix P with inertia $(p, 0, n-p)$ and a positive constant ε such that

$$\partial f(x)^T P + P\partial f(x) + 2\lambda P \leq -\varepsilon I \tag{2.7}$$

for all $x \in \mathbb{R}^n$.

(2.7) provides a tractable condition for p-dominance through convex relaxation, as shown in [58, Section VI.B] and [18, Chapter 4]. It enforces a uniform splitting among the eigenvalues of $\partial f(x)$ into p slow eigenvalues to the right of $-\lambda$ and $n - p$ fast eigenvalues to the left. Our interest in the property stems from the fact that p-dominance strongly constrains the system asymptotic behavior, as clarified by the following proposition from [58, Corollary 1]

Proposition 1 Every bounded trajectory of a p-dominant system $\dot{x} = f(x)$, $x \in \mathbb{R}^n$, asymptotically converges to

    - a unique fixed point if $p = 0$;

    - a fixed point if $p = 1$;

    - a simple attractor if $p = 2$, that is, a fixed point, a set of fixed points and connecting arcs, or a limit cycle. ⌟

[58, Theorem 2] shows that the asymptotic behavior of a p-dominant system is captured by a p-dimensional dynamics, which thus guarantees simple attractors for $p \leq 2$. We observe that a system can be p_1-dominant and p_2-dominant, $p_1 \leq p_2$, for different rates $\lambda_1 \leq \lambda_2$. In using the theory, wee are typically interested in finding the smallest degree of dominance, which corresponds to the simplest asymptotic behavior.

2.3.3 p-gain and small gain interconnections

Differential dissipativity [58], [109] extends dominance theory to open systems. We refer the reader to these publications for details. We will use the following notion of p-gain.

Definition 2 An open system $\dot{x} = f(x) + Bu$, $y = Cx$, with input u, output y, and state x, has p-gain γ with rate $\lambda \geq 0$ if there exists a symmetric matrix P with inertia $(p, 0, n - p)$ and a positive constant ε such that

$$\begin{bmatrix} \partial f(x)^T P + P \partial f(x) + 2\lambda P + C^T C - \varepsilon I & PB \\ B^T P & -\gamma^2 I \end{bmatrix} \leq 0 \qquad (2.8)$$

for all $x \in \mathbb{R}^n$. ⌟

A straightforward specialization of [58, Theorem 4], see also [121], provides a differential version of the small gain theorem, which allows us to use the p-gain of a system to characterize its robustness in presence of model uncertainties, as in classical robust control theory [41, 170, 155].

Proposition 2 For $i \in \{1, 2\}$, let Σ_i be systems with input u_i, output y_i, and p_i-gain γ_i with rate $\lambda_i = \lambda \geq 0$. If $\gamma_1 \gamma_2 < 1$ then the closed loop system given by $y_1 = u_2$ and $y_2 = u_1$ is $(p_1 + p_2)$-dominant. ⌟

Proposition 2 opens the way to the study of robust attractors that are not fixed points. This is particularly relevant in system biology. In what follows we will take advantage of the tractability of (2.7) combined with Proposition 1 to characterize the steady state behavior of dendritic traffic regulation. Then, we will use the notion of p-gain in combination with Proposition 2 to study its robustness.

The p-dominance framework will prove very useful to study the regulation problem in more detail. Specifically, unlike the stereotypical stable vs unstable classifications, we will separate the regulation phenomena into three distinct regimes: nominal, aggressive, and unstable. Furthermore, dominance theory also provides another mean to study robustness, beyond monostability, using state-space representations. We use dominance theory in Chapter 7.

2.4   Timescale separation and singular perturbation

An important technique that is used throughout this dissertation is the use of timescale separation. Systems in nature, and more dominantly in biology, occur in multiple time or length scales. Timescale separation is an important tool that helps elucidate the complexity of the phenomena of interest and gives insights about the underlying structure. One way to do this mathematically is by "freezing" the slow dynamics or setting the fast dynamics to steady-state, which is done by setting a small parameter to zero. A slow-fast system can have the following form

$$\dot{x} = f(t,x,z,\varepsilon) \tag{2.9}$$
$$\varepsilon\dot{z} = g(t,x,z,\varepsilon)$$

where $0 < \varepsilon \ll 1$. In equation (2.9) x is the slow variable and z is the fast one. In setting $\varepsilon = 0$, one can derive a dependence of the fast variable z on the slow variable x, $z = h(t,x)$ which is called the boundary-layer system. In other words, $h(t,x)$ is a solution to the *slow manifold* $g(t,x,z,0) = 0$. Motion on this manifold evolves according to the equation $f(x,h(x,t),t,0)) = 0$, which is called the *reduced system*.

We use [90, Theorem 11.4] to prove exponential stability of the equilibrium of proposed models. The theorem is stated below.

Theorem 2 *Consider the singularly perturbed system* (2.9). *Assume the following assumptions are satisfied for all* $(t,x,\varepsilon) \in [0,\infty) \times B_r \times [0,\varepsilon]$

- $f(t,0,0,\varepsilon) = 0$ *and* $g(t,0,0,\varepsilon) = 0.$

- *The equation $0 = g(t,x,z,0)$ has an isolated root $z = h(t,x)$ such that $h(t,0) = 0$.*

- *The functions f, g, h and their partial derivatives up to the second order are bounded for $z - h(t,x) \in B_\rho$.*

- *The origin of the reduced system $\dot{x} = f(t,x,h(t,x),0)$ is exponentially stable.*

- *The origin of the boundary-layer system $\frac{dy}{d\tau} = g(t,x,y+h(t,x),0)$ is exponentially stable, uniformly in (t,x).*

Then, there exists $\varepsilon^* > 0$ such that for all $\varepsilon < \varepsilon^*$, the origin of (2.9) *is exponentially stable.*

Theorem 2 will be used throughout this dissertation to prove exponential stability of the equilibrium of different closed loop systems. Typically these theorems will provide bounds on parameters, such as time constants, that guarantee stable behavior. In Table 2.1, we summarize the mathematical tools introduced in this chapter, and where we will employ them.

Table 2.1 Methods summary

Mathematical tool	Chapter	Notes
Linear compartmental systems	3-6	Model of AMPA trafficking
Nonlinear compartmental systems	7-8	Model nonfunctional cargo transport
Nyquist stability criterion	$3-5$	Analysis of the synaptic scaling model
p-dominance	7	Analysis of the regulation of with nonlinear transport
Singular perturbation techniques	3-8	Used to prove exponential stability of multiple mathematical models

Chapter 3

The closed loop synaptic scaling model

*"Somehow the unstable stuff of which we
are composed has learned the trick of
maintaining stability."*

Walter Cannon, *The Wisdom of the Body*

In this chapter we formulate a biophysically-motivated mathematical model of synaptic scaling from first principles. In particular, we model the synthesis, transport, insertion, and regulation of AMPA receptors in the presence of a homeostatic scaling mechanism.

3.1   Model overview

We begin with an abstract visualization of a neuron (soma and its dendritic tree), and we will describe the main biophysical processes of interest (Figure 3.1a): AMPAR transport and insertion, local and global feedback, and cargo production. We will refer to the model as the *closed loop synaptic scaling* model, and **CLSS** for short.

Active transport is the assumed mode of trafficking for AMPARs. They are trafficked on microtubules throughout the dendrites (Figure 3.1b). Internal, inactive AMPARs m are transported with forward rate v_f and backward rate v_b. Active, external AMPARs on the surface are denoted g. AMPARs activation ($m \to g$) occurs within synaptic sites on the plasma membrane. The capacity of a synaptic site is denoted by c, which represents the number of available slots for AMPARs. We impose an abrupt change in c to emulate long term potentiation or depression (LTP or LTD). This is consistent with the physiologic increase in structural proteins that support AMPARs on the plasma membrane during potentiation [105, 114].

(a) Components of the **CLSS** model.

(b) Trafficking of AMPA receptors.

(c) Attachment and detachment of AMPA receptors.

(d) average activity and AMPA synthesis.
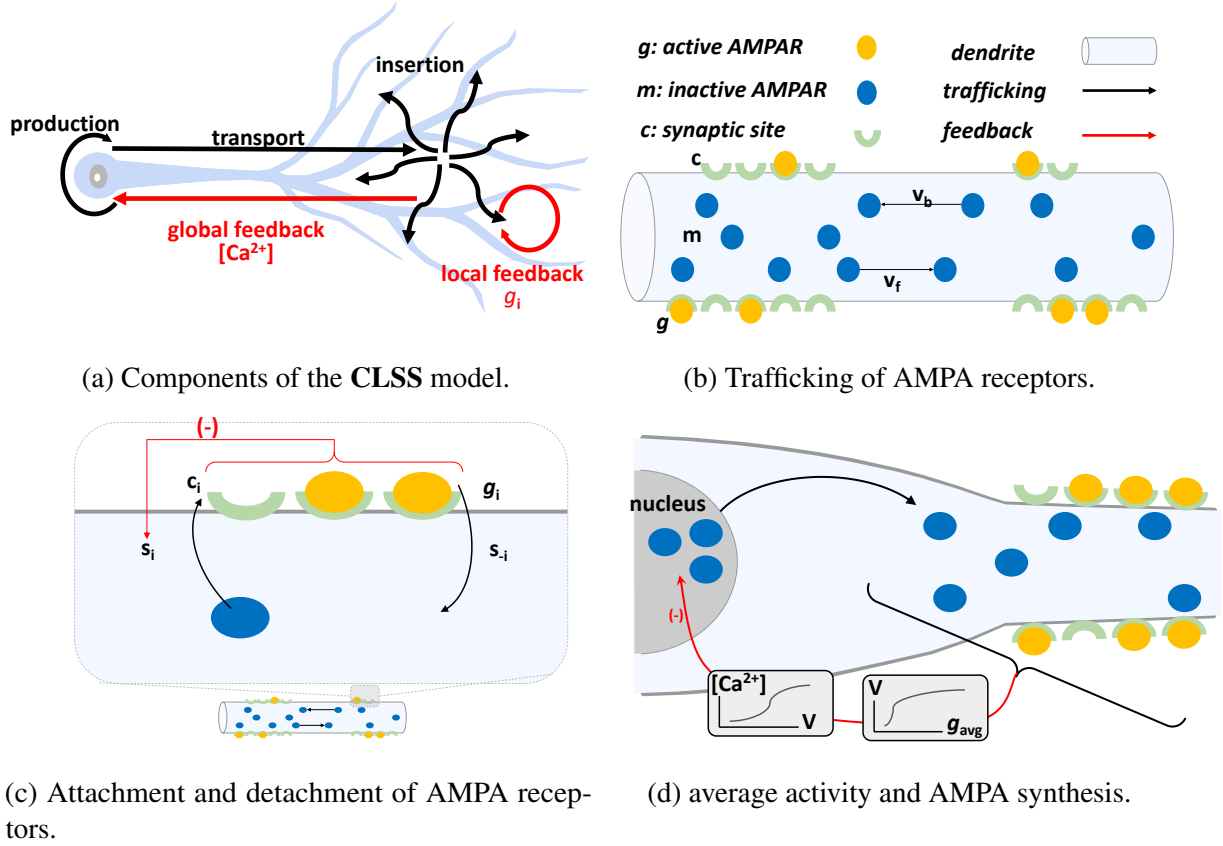
Fig. 3.1 A schematic description of the components of the **CLSS** model: in (a), we show where the different processes take place, (b) shows dendritic transport of AMPA receptors, (c) shows the activation and inactivation of AMPARs, and (d) the feedback signal is computed.

Cargo insertion is illustrated in Figure 3.1c. Cargo is activated ($m_i \rightarrow g_i$) with activation rate s_i and inactivated ($g_i \rightarrow m_i$) with rate s_{-i} in each ith compartment (a compartment represent a small section of the dendritic tree, as discussed in the next section). Homeostatic local feedback occurs in each synapse, where local g regulates s_i based on $[Ca^{2+}]_{target}$. Local gain k_L is the sensitivity of the local controllers to perturbations in local g, and s_i increases or decreases in accordance with variations in g_i. AMPARs transport with global and local feedback are incorporated into a compartmental model of a discretized dendritic arbor, which will explained thoroughly over the next sections.

Combined to forms of potentiation (such as LTP and LTD), a neuron maintains its level of excitability through global regulation mechanism, which occurs in the soma (Figure 3.1d). The mean of all active AMPARs $\frac{1}{n}\sum g_i$ produces an average membrane potential V, representing a change in neural firing rate. This modulates the concentration of internal $[Ca^{2+}]$, which in turn regulates biosynthesis and release u of new receptors into circulation.

The global gain k_G is the sensitivity of the global regulator to perturbations in $[Ca^{2+}]$ based on some set point $[Ca^{2+}]_{target}$. The effect of this homeostatic mechanism is that if neuron activity is too low, more AMPARs are produced; if activity is too high, AMPAR production is slowed. We will show that global regulation is sufficient for normalization of synaptic strengths [151, 148]. In the following section, we formulate the **CLSS** model mathematically starting from first principles and stating the relevant assumptions when necessary.

The mathematical description of the **CLSS** model begins with a discussion of the two species in the system: *m* and *g*. *g* is the effective form of AMPA receptors (AMPARs), active and located in their functional sites. *g* affects neuron properties (like intrinsic excitability, synapse strength, etc.). *m* is the precursor to *g*. *m* can take the form of pro-protein, pre-pro-protein, protein endocytosed in vesicles, or other internalized pool of the protein. We refer to *m* and *g* as "cargo", to emphasize the fact that they are transported within the dendrite, although in different forms.

3.1.1   Dendritic trafficking of AMPA receptors

We discussed in the introduction the different modes of trafficking that occur in the cell, namely active and passive transport. Modeling this phenomena as an active transport process, we assign to *m* forward trafficking rate v_f and backward trafficking rate v_b. Forwards trafficking rate v_f will denote movement away from the soma, while backward trafficking v_b will denote movement towards the soma. We dissect and compartmentalize the neuron into separate segments, as portrayed in Figure 3.2. The dendritic tree is divided in small sections, each associated with an index *i*. m_i and g_i will denote the concentrations of cargo in the ith section. Therefore, trafficking between adjacent compartments can schematically depicted as

$$m_i \; \underset{v_b}{\overset{v_f}{\rightleftarrows}} \; m_j$$

.
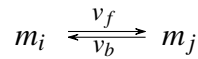
In this way, the neuron is composed *n* compartments. The number of compartments reflects the resolution of system. $\dot{m}_i$, is thus affected, among other factors, by the "transport" term:

$$f(m_i) = v_f m_{i-1} - (v_f + v_b)m_i + v_b m_{i+1} \tag{3.1}$$

We assume that transport among synapse compartments occurs for the cargo precursor *m* only. In this study, we set all the forward trafficking rates to be uniform, as well as the backward rates. The linear model in Equation (3.1) is adopted for simplicity. In a more detailed model,

one could vary trafficking rates after each branching point to account for dendritic diameter changes. Moreover, one can transcend this linear model by adopting a nonlinear version of transport that captures finite capacities and crowding effects. This is done in Chapters 7-8.
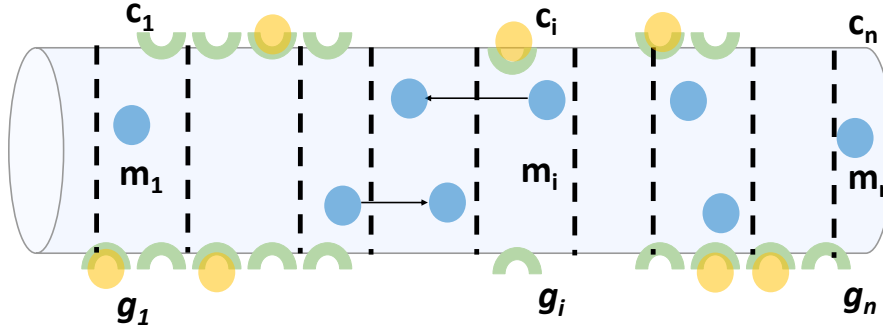
Fig. 3.2 Linear compartmental model of transport: the dendritic tree is discretized into smaller compartments of equal size, and mass balance between compartments is used to capture the trafficking of material.

3.1.2   Activation and inactivation of AMPA receptors

Experimental studies reveal inactive pools of AMPAR receptors located internally or anchored to nanodomains. These inactive AMPARs are available to cycle to and from post-synaptic sites [78]. We therefore implement a reversible reaction between m and g:

$$m_i \xrightleftharpoons[s_{-i}]{s_i} g_i$$
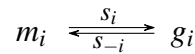
where s_i and s_{-i} are the transfer rates from m_i to g_i, and g_i to m_i, accordingly. The subscript i indexes the spatial compartment of the species. Dendritic compartments are discretized into n compartments. g_i are located in the postsynaptic terminals of dendritic spines.

A dendritic spine consists of a neck that connects the dendritic shaft to a spine head containing ion channels, receptors, and other proteins. Spines are heterogeneous throughout a dendritic tree, with variable size, volume, and number of receptor slots. We assume that spines are significantly smaller than the dendritic shafts. Therefore, g_i have finite capacity which limits g_i concentration. Spine size and number of receptor slots are plastic, which impacts synaptic activity and strength [72]. We capture this property of spines, synapses, and postsynaptic densities in a single term for capacity c_i. Taking inspiration from [148], we

model the interaction between m_i and g_i as follows:

$$\dot{m}_i = u + f(m_i) - s_i m_i (c_i - g_i) + s_{-i} g_i - \omega_i^m m_i \tag{3.2}$$
$$\dot{g}_i = s_i m_i (c_i - g_i) - s_{-i} g_i - \omega_i^g g_i$$

Parameters ω_i^m and ω_i^g represent degradation rates for m_i and g_i, respectively. $f(m_I)$ summarizes the transport that occur among the m species, discussed previously, and u is AMPARs biosynthesis. The nonlinear term $m_i(c - g_i)$ can be interpreted as a saturation that arise from modeling the transition from m_i to g_i as a mean-field approximation of a *Partially Asymmetric Exclusion Process* (PASEP) [125]. This allows us to model the finite capacity of a spine/synapse, to simulate perturbations in synaptic expression and plasticity, all while maintaining the driving force of mass action.

The previous processes can be written more compactly in the a matrix form

$$\dot{m} = (L_m - \Omega_m)m - S(g)m + Ag + Bu \tag{3.3}$$
$$\dot{g} = -\Omega_g g + S(g)g - Ag,$$

where $L_m \in \mathbb{R}^{nxn}$ describes the trafficking of m_i's, $\Omega_m = \text{diag}\{\omega_m^i\}$ ($\Omega_m \in \mathbb{R}^{nxn}$) captures the degradation of m_i's, $S(g) = \text{diag}\{s_i(t)(c_i - g_i)\}$ ($S(g) \in \mathbb{R}^{nxn}$) is the activation matrix, $A = \text{diag}\{s_{-i}\}$ ($A \in \mathbb{R}^{nxn}$) is the inactivation matrix, and $B = [1; 0; \ldots; 0]^T$, and $B \in \mathbb{R}^{nx1}$. It is worth noting that L_m bears the information of network structure.

3.2   A system-theoretic view on synaptic scaling

3.2.1   AMPA receptor synthesis as global control

In line with experimental data and existing models [115–117], we assume that channel mRNA synthesis, which occurs only in the first compartment, is dependent on calcium concentration, $[Ca^{2+}]$. Existing models posit that biochemical pathways modulate mRNA synthesis according to the deviation of calcium concentration from an effective set-point, $[Ca^{2+}]_{\text{target}}$. The form of process that transforms the error signal, $e_G = [Ca^{2+}]_{\text{target}} - [Ca^{2+}]$, into the control signal/variable u in Equation (3.2) is the subject of ongoing research. In particular, the question of whether perfect set point tracking is achieved is of great interest. Here we adopt a basic model for this complex process, based on a leaky integral controller:

$$\dot{u} = k_G e_G - \omega_u u \tag{3.4}$$

$$e_G = [\text{Ca}^{2+}] - [\text{Ca}^{2+}]_{\text{target}}$$

where k_G is the feedback gain that captures the controller sensitivity to deviation in the error term e_G, $\omega_u > 0$ sets the degradation. In the limit of $\omega_u \to 0$, (3.4) becomes a pure integrator.

We assume that the calcium influx occurs on a substantially faster timescale than cargo production and transport [144]. We also assume that the calcium influx varies due to voltage-dependent channels and may be related to the (quasi-steady state) membrane potential via the saturating monotonic relationship:

$$[\text{Ca}^{2+}] = \frac{\alpha}{1 + \exp V/\beta}. \tag{3.5}$$

The parameters α and β capture calcium buffering and the voltage sensitivity of calcium channels [116]. Finally, to model the effect of channel protein concentration on the membrane potential, V, we consider the standard single compartment membrane equation

$$C\dot{V} = g_{leak}(E_{leak} - V) + g_{avg}(E_g - V),$$

where C is membrane capacitance, g_{leak} is a fixed, leak conductance, and the E_{leak} and E_g terms are equilibrium potentials for each type of ionic conductance, and g_{avg} is the averaged sum of g_i in the neuron. By using a single compartment membrane equation we are assuming that the neuron is equipotential (V is independent of compartment index). This is justified by the timescale separation between the fast voltage fluctuations and the mRNA synthesis and trafficking mechanisms. We therefore set the membrane potential to its quasi-steady state

$$V := V_{\text{ss}} = \frac{g_{avg}E_g + g_{leak}E_{leak}}{g_{leak} + g_{avg}}, \quad g_{avg} = \frac{\mathbf{1}^T g}{n} = \frac{\Sigma g_i}{n}. \tag{3.6}$$

This simple model of conductance averages the fast, computationally-expensive dynamics for electrical signal transmission in a neurite. Rather than simulating excitatory postsynaptic potential (EPSP) input and initiation/propagation of dendritic spikes, membrane potential in the soma is computed as an average of electrical activity over a timescale closer to that of AMPAR production and trafficking. In this scheme, the global feedback and regulation are dependent on the average amount of AMPARs throughout the neurite: g_{avg}. We assume that these dynamics converge quickly compared to cargo production and transport and occur at a similar timescale to $[\text{Ca}^{2+}]$ influx in Equation (3.2).

The regulation mechanism modelled in Equation (3.4) drives the production of cargo with the goal of attenuating the mismatch between the desired calcium target and the actual average calcium. Ideally, perfect regulation is achieved when $[Ca^{2+}] = [Ca^{2+}]_{target}$. For this to be feasible, we make the following assumption.

Assumption 1 *The parameters of* (3.5)-(3.6) *satisfy*

$$E_g + \beta \ln \frac{\alpha}{[Ca^{2+}]_{target}} \neq 0 \ and \ g_{leak} \neq 0 \ .$$

The quantities in Equations (3.5) and (3.6) are combined and integrated in (3.4) to achieve regulation. For readability, we will refer to their aggregate contribution by using the non-decreasing function $h : g \to [Ca^{2+}]$ to be the composition of the static maps (3.5)-(3.6):

$$[Ca^{2+}] = h(g_{avg}). \tag{3.7}$$

Figure 3.3 shows the monotonicity of (3.7).
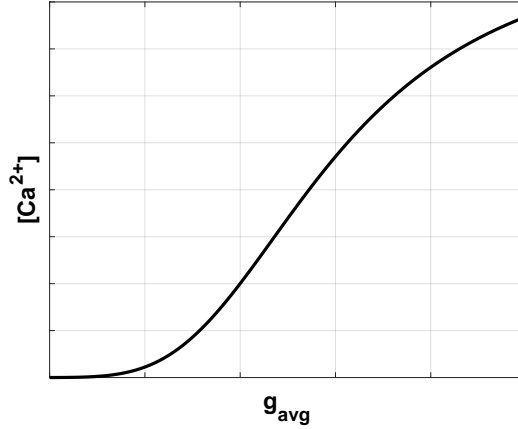
Fig. 3.3 Monotonicity of the feedback signal $h(g_{avg})$.

Before proceeding to the next part of the model, we will clarify some of the modeling choices and assumptions that are related to (3.5)-(3.6). Firstly, in the above model we used intracellular calcium concentration as the homeostatic signal of the closed loop system, and this was experimentally identified [150, 147, 115] and further used in other computational studies [166]. It is worth highlighting here that this setting exemplifies known instances in neuronal systems where the signal that is being explicitly regulated is not necessarily the observed phenomenon (e.g. spiking) [118]. In other words, and on a more fundamental level,

we are using calcium concentration as an error signal that correlates to the fast changes in excitatory input.

Secondly, we used a leaky-integrator model as opposed to a Hodgkin–Huxley model, i.e. a one that incorporates voltage-dependent conductances. At the first sight, the latter model appears to be more suitable and interesting to study homeostatic regulation. Nevertheless, it was shown that the qualitative behavior of a simple leak model matched those obtained for a conductance-based model [116]. Therefore, we expect the presented model above to be informative, and can indeed reveal a number of relevant physiological properties of homeostatic regulation. Moreover, we expect the behavior to not drastically vary when a conductance-based model is inserted in place of the leaky-integrator one, specially near equilibrium [116].

3.2.2   Adaptive AMPA receptor activation as local control

As we discussed before, both short- and long-term synaptic plasticity in neurons have been associated with information processing and memory formation [94]. At the molecular level, the presynaptic probability of neurotransmitter release for individual synapses is dynamic [19]. Postsynaptic terminals undergo long-term plasticity, in which AMPARs are inserted or removed from post-synaptic sites. These neural tasks are enabled by the filtering characteristics of synapses, in which synapses with varying release probabilities act as low-pass or high-pass filters. This property can be changed according to the presynaptic action potential. Long-lasting changes allow neurons to form spatiotemporal patterns as a result of activity-dependent changes. In our model, such changes are achieved by fine-tuning individual g_i while also maintaining overall neuron activity level around $[\mathrm{Ca}^{+2}]_{\mathrm{target}}$. By fine-tuning g_i, a neuron can vary synaptic strengths while maintaining average neural activity.

We model these post-synaptic changes by enforcing a change in synpatic capacity c_i. This results into a fluctuation of active AMPAR g_i with LTP and LDP events [104, 103]. Local activity-dependent regulation also modifies intraspinal AMPAR trafficking rates, such as interactions with the scaffolding protein Stargazin [134]. Further, experiments reveal activity-dependent regulation of AMPAR in and out of the dendritic spines. For instance, phosphorylation or phosphorylation-induced changes in synapses can activate AMPARs [79]. In our model, we lump these complex mechanisms and interactions into synaptic capacity c_i and rates s_i and s_{-i}.

We augment the dendritic trafficking model with local activity-dependent regulation. Local regulation is faster than the other model dynamics (cargo production and transport). This captures the local biological processes that take place at the synapse level. In contrast to the broad averaging of the global feedback, local feedback tunes individual g_i's. This

allows for regulation at high spatial resolution, such as homeostatic plasticity of individual compartments or branches. We assume that individual synapses measure a local error signal e_L that compares local activity g_i to the global target activity level $[Ca^{2+}]_{target}$ to modify local AMPAR activation s_i. Mathematically,

$$\varepsilon \dot{s}_i = k_L e_L - \omega_L(s_i - \bar{s}_i) \tag{3.8}$$
$$e_L = [Ca^{2+}]_{target} - H(g_i)$$
$$H(g_i) = \frac{s_{max} g_i^h}{g_i^h + k_A^h}$$

where ε is a time constant that reflects the fast dynamics of $\dot{s}_i$ (typically $\varepsilon \ll 1$), k_L is the sensitivity of the local controller, ω_L is the degradation/dissipation rate of s_i, and $\bar{s}_i$ is the uncontrolled/basal value of s_i. In the local regulation scheme (3.8), $H(g_i)$ takes the form of a Hill equation, where s_{max} defines the upper limit, k_A is the apparent dissociation constant, and h is the Hill coefficient that describes the degree of cooperativity. $H(g_i)$ captures the structural and conformational changes that AMPARs undergo to transform into an active state [10, 169, 35].

Equation (3.8) shows that g_i affects s_i in a negative feedback manner. Whenever $k_L > 0$, this scheme will have an opposing effect on g_i. This adds a stabilizing effect on the steady-state value of g_i, which opposes runaway dynamics of unconstrained Hebbian plasticity.

In Figure 3.4, we emphasize the system-theoretic view by showing a conceptual block diagram that portrays synaptic scaling as a controller at the global level (Figure 3.4a), and adaptive-activation is portrayed as a local control action (Figure 3.4b). The red lines distinguish the path of the feedback signal.

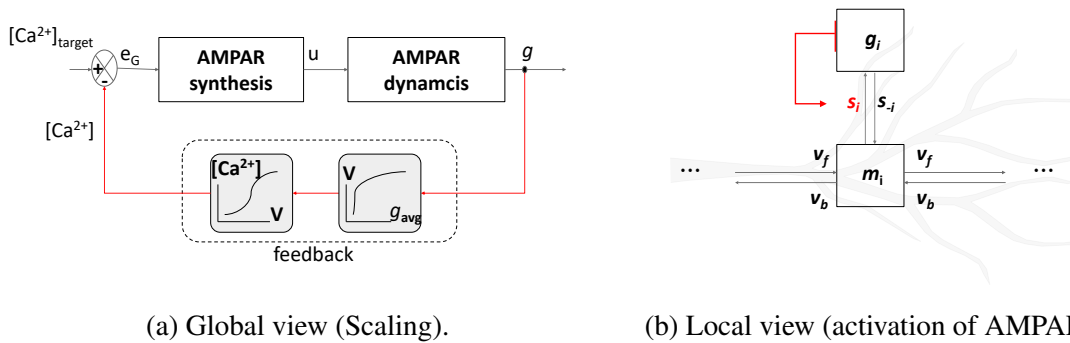(a) Global view (Scaling).   (b) Local view (activation of AMPARs).

Fig. 3.4 A system-perspective on regulation: showing the two different layers of control, the global one (homeostatic synaptic scaling), and local one (adaptive activation of AMPA receptors).

3.3   Stability of the synaptic scaling model

Now that we have formulated the model, we state the stability result which guarantees homeostasis under certain conditions.

Theorem 3 *Under Assumption 1, there exists a $\bar{k}_G > 0$, and $\bar{\varepsilon} > 0$ such that, for every $0 < k_G \leq \bar{k}_G$ and $0 < \varepsilon \leq \bar{\varepsilon}$, the closed loop system (3.3)-(3.8) has a globally exponentially stable equilibrium.*

How is homeostasis implied from Theorem 3? Firstly, the exponential stability of the equilibrium point of (3.3)-(3.8) indicates that the equilibrium point is unique. This means all physiologically initial conditions will converge to this unique equilibrium. At steady-state, Equation (3.4) guarantees that $[Ca^{2+}] \approx [Ca^{2+}]_{target}$, and hence achieving homeostasis. More importantly, by changing the model parameters while keeping $[Ca^{2+}]_{target}$ fixed, homeostasis is maintained but now for a different steady-state concentration profile of g. This means that the neuron can spatially change individual synaptic efficacies, while maintaining the average activity level around its set-point; we attribute this feature of the model to homeostatic synaptic scaling. This feature, as we will see in the next section, is profoundly linked to feedback.

The conditions of Theorem 3 reveal an inherent limitation of the closed loop system. As far as the gain is less than $\bar{k}_G$, stable regulation is achieved. However, once this condition is violated, stability is not necessarily preserved. This is due to the subdynamics of transport of the **CLSS** model. The constraint is caused by the interplay of synthesis, transport, and degradation of AMPARs. Hence, an upper bound on gain k_G is required to limit how rapid AMPAR production can be, due to a limit on how fast they can be transported and degraded. This means that the overall system suffers from a severe limitation on how fast it can deliver AMPARs to demand sites. In fact, this is not the only limitation as we will see in the next chapter where we introduce three performance measures that we will use to study the effects of morphology on the regulation problem.

Similarly, $\bar{\varepsilon}$ establishes a limit on how slow AMPARs activation can be. In other words, activation of AMPARs needs to be sufficiently fast in order for proper regulation to occur. If the activation dynamics (3.8) is slow, then m will accumulate in the system before properly being utilized in synaptic sites in the form of g. Next, once g is at the level where $[Ca^{2+}] \approx [Ca^{2+}]_{target}$, production of m slows down causing a shortage of m which subsequently deprive synaptic sites of g. This, in turn, increases the mismatch (higher e_G). In principle, the same asynchrony happens as in the case of high k_G.

Theorem 3 affirms that two regulatory mechanisms (local and global) can coexist and support homeostasis. However, the exact contribution of each mechanism, and whether it is a

cooperative or competitive effect remains unclear. Through simulations, we uncover this in the next chapter.

3.4 Chapter summary and concluding remarks

This chapter can be summarized in the following key points:

1. We have presented a model of neuronal activity regulation which comprehends transport, activation, averaged voltage and calcium dynamics, and local and global regulation mechanisms.

2. Theorem 3 shows that the closed loop system is stable if the global gain is limited to a defined interval. This makes clear that the action of the global controller is somehow limited and high gain feedback leads to potential instabilities. This discussion will be extended in the next chapter.

Table 3.1 Parameter Values

(3.5)-(3.6)	(3.1), (3.2), (3.4)	(3.8)
$g_{leak} = 0.25 \ \mu S$	$v_f = 1 \ \mu m s^{-1}, \ v_b = 0.5 \ \mu m s^{-1}$	$\bar{s}_i = 1 \ s^{-1}$
$E_{leak} = -50 \ mV$	$\omega_i^g = \omega_i^m = 0.1 \ s^{-1}$	$\omega_L = 1 \ s^{-1}$
$E_g = 20 \ mV$	$\omega_u = 1 \times 10^{-5} \ s^{-1}$	$s_{max} = 2$
$\alpha = \beta = 1$	$s_{-i} = 0.5 \ s^{-1}$	$k_L = h = 1$
$[Ca^{2+}]_{target} = 0.5 \ \mu M$	$c = 1, k_G = 0.3$	$\varepsilon = 0.1$

To have a glimpse over the content of the next chapter, we conclude this chapter with the following simulation. To examine the transient and steady-state behavior of **CLSS** system, we simulate a $10-$compartmental cascading neuron model with parameter values from Table 3.1[1] As laid out before, we model permanent structural changes due to LTP events through changes in c_i. Figure 3.5 shows the timecourse of g_i's where an LTP event took place halfway through the simulation in the synapses with the red traces. The simulation portrays the performance measure we partially alluded to earlier. Firstly, consistent with LTP events recorded in experiments, the efficacy of synapses that were subject to such events increased. This was accompanied by a global decrease in the efficacy of unpotentiated ones. However,

---

[1]The parameters in Table 3.1 are well within reported numbers in the literature, both in computational and experimental studies. For example, the electrophysiological parameters in the left column match those in [117, 115, 116] and references therein. The trafficking and synthesis parameters in the middle column are within the used and reported parameters ranges [148, 22, 161, 122]. The adaptive activation parameters in the right column where chosen to produce values of s_i close to those used in [148, 23].

the ratio of increase (and decrease) of individual synapses in inhomogeneous. Secondly, the transient response is oscillatory and this can be undesired as this is an energy-expensive process, and it is reasonable to assume that a biological system, like a neuron, ideally needs to minimize energy expenditure. Lastly, the time it takes the neuron to deliver AMPARs to where they are needed is of crucial importance, too. In the next chapter, we define, quantify, and study these aspects of the regulation problem to reveal an inevitable tradeoff imposed by neuron geometry.
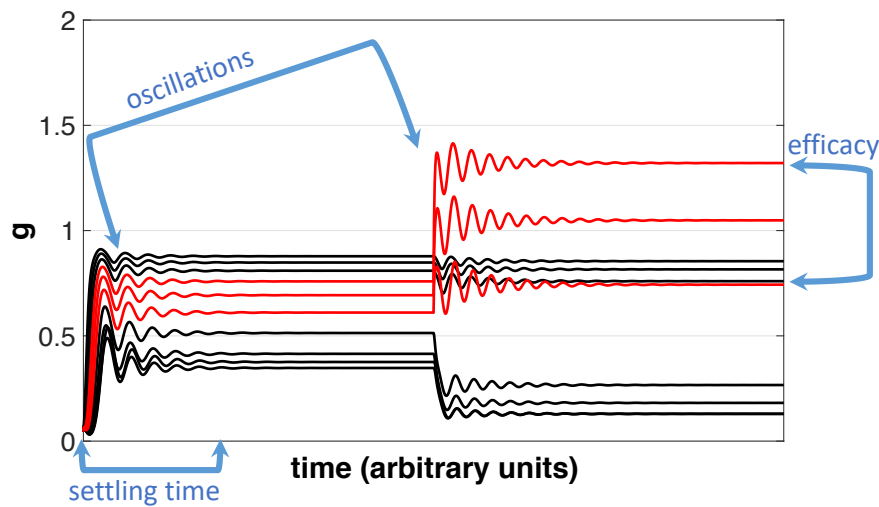
Fig. 3.5 Simulation of a $10-$compartmental system: time response of g_i where an LTP event occurs in red compartments halfway through the simulation. Black (unponentiated) synapses are globally scaled down as a result of scaling.

3.5   Proof of theorem 3

Part 1 and Part 2 below satisfy the conditions of Theorem 11.4 in [90]. By doing so, we can conclude the exponential stability of the equilibrium point of the closed loop system. This is done by analyzing two subsystems, namely the boundary layer and reduced subsystems.

Part 1: stability of the boundary layer system

We first obtain the solution of $\dot{s}_i = 0$, which is $s_i = \frac{k_L([Ca^{+2}]_{\text{target}} - H(g_i))}{\omega_L} + \bar{s}_i$. Then we introduce the new variable $z_i = s_i - \left(\frac{k_L([Ca^{+2}]_{\text{target}} - H(g_i))}{\omega_L} + \bar{s}_i\right)$. Taking the time-derivative of both sides holds:

$$
\begin{aligned}
\dot{z}_i &= \frac{d}{dt}\left[s_i - \left(\frac{k_L([Ca^{+2}]_{\text{target}} - H(g_i))}{\omega_L} + \bar{s}_i \right) \right] \\
&= \dot{s}_i - \frac{d}{dt}\left[\frac{k_L([Ca^{+2}]_{\text{target}} - H(g_i))}{\omega_L} + \bar{s}_i \right] \\
&= -\frac{\omega_L}{\varepsilon} z_i - \frac{d}{dt}\left[\frac{k_L([Ca^{+2}]_{\text{target}} - H(g_i))}{\omega_L} + \bar{s}_i \right]
\end{aligned}
$$

By introducing $\tau = \frac{t}{\varepsilon}$, the boundary layer system is obtained in the limit of $\varepsilon \to 0$

$$
\frac{dz_i}{d\tau} = -\omega_L z_i. \tag{3.9}
$$

Since $\omega_L > 0$, the equilibrium of the boundary-layer system is exponentially stable.

Part 2: Stability of the reduced-order system

We proceed by making the following substitution or coordinate change. Let $\eta := [m, g]^T$, then equation (3.3) can be re-written as

$$
\begin{aligned}
\dot{\eta} &= f(\eta) + u \\
\dot{u} &= k_G e_G - \omega_u
\end{aligned} \tag{3.10}
$$

where $f(\eta)$ captures the transport dynamics of m, degradation of m and g, and activation and inactivation between m and g ($m \rightleftarrows g$), and transport between the g's (lateral diffusion) if modeled. All the entries of $f(\eta)$ are constants except the ones that describe the interaction

between *m* and *g*. The differential system reads:

$$\delta\dot{\eta} = \frac{\partial f(\eta)}{\partial\eta}\delta\eta + \delta u$$

$$\delta\dot{u} = -k_G\partial\psi(c^T\eta)c^T\delta\eta - \omega_u\delta u \tag{3.11}$$

Since $f(\eta)$ describes how the matter/molecules is being transported, exchanged, and degraded , the Jacobian $\frac{\partial f(\eta)}{\partial\eta}$ enjoys a number of structural properties that will utilized later on in the proof (in other words and loosely speaking, $f(\eta)$ is the Laplacian matrix of network). Firstly, $\frac{\partial f(\eta)}{\partial\eta}$ represents a positive system. This means that the off-diagonal entries are always positive, and the diagonal are always strictly negative. Another feature is that the some of column is always ω_i^m or ω_i^g, which has a strong bound on the dominant or Perron-Frobenius eigenvalue at each linearization, i.e. $\lambda_{pf} = -\min\{|\omega_m^i|, |\omega_g^i|\}$. Considering the uncontrolled dynamics only, i.e. $\dot{\eta} = f(\eta)$, the prolonged system is $\delta\dot{\eta} = \frac{\partial f}{\partial\eta}(\eta)\delta\eta$. This can be written equivalently as $\delta\dot{\eta} = -\frac{\partial g}{\partial\eta}(\eta)\delta\eta$, where $\eta \in \mathscr{R}^{2n}$, $\frac{\partial g}{\partial\eta}(\eta) = -\frac{\partial f}{\partial\eta}(\eta)$, and $\frac{\partial g}{\partial\eta}(\eta) + \frac{\partial g}{\partial\eta}(\eta)^T \geq -\lambda_{pf}I > 0$. Therefore, for the Lyapunov function $V = \frac{1}{2}\delta\eta^T\delta\eta$ the time derivative reads:

$$\dot{V} = -\delta\eta^T(\frac{\partial g}{\partial\eta}(\eta)^T + \frac{\partial g}{\partial\eta}(\eta))\delta\eta \leq \lambda_{pf}\delta\eta^T\delta\eta < 0.$$

$$\tag{3.12}$$

The above property is preserved even after obtaining the reduced-order system, that is $\frac{\bar{\partial}g}{\partial\eta}(\eta) + \frac{\bar{\partial}g}{\partial\eta}(\eta)^T \leq -\lambda_{pf}I < 0$, where $\frac{\bar{\partial}g}{\partial\eta}$ is obtained after replacing $s_i(t)$'s with s_i^*. Next, we consider the Lyapunov function $V = \frac{\rho_\eta}{2}\delta\eta^T\delta\eta + \frac{1}{2}\delta u^T\delta u$. ρ_η is a positive parameter that will be constructed later to satisfy certain relations necessary for stability. The time-derivative of the V

$$\dot{V} = \rho_\eta\delta\eta^T(\frac{\partial\bar{f}(\eta)}{\partial\eta}^T + \frac{\partial\bar{f}(\eta)}{\partial\eta})\delta\eta + \rho_\eta\delta\eta^T\delta u$$
$$- k_G\partial\psi(c^T\eta)c^T\delta\eta\delta u - \omega_u\delta u^T\delta u$$
$$\leq \rho_\eta\lambda_{pf}\delta\eta^T\delta\eta + \rho_\eta\delta\eta^T\delta u - k_G\partial\psi(c^T\eta)c^T\delta\eta\delta u - \omega_u\delta u^T\delta u$$
$$\leq -\rho_\eta|\lambda_{pf}||\delta\eta|^2 + \rho_\eta|\delta\eta||\delta u| + k_G|\partial\psi(c^T\eta)c^T||\delta\eta||\delta u| - \omega_u|\delta u|^2$$

or

$$\dot{V} \leq \begin{bmatrix} |\delta\eta| \\ |\delta u| \end{bmatrix}^T \underbrace{\begin{bmatrix} -\lambda_1 & 0 \\ \lambda_2 & -\lambda_3 \end{bmatrix}}_{-Q} \begin{bmatrix} |\delta\eta| \\ |\delta u| \end{bmatrix}$$

where

$$\lambda_1 = \rho_\eta |\lambda_{pf}|$$
$$\lambda_2 = \rho_\eta + k_G |\partial \psi(c^T \eta) c^T|$$
$$\lambda_3 = \omega_u.$$

The problem now reduces to proving that $Q > 0$. Firstly, we write the equivalent symmetric problem $\frac{Q+Q^T}{2} > 0$, that is,

$$\begin{bmatrix} \rho_\eta |\lambda_{pf}| & -\frac{1}{2}(\rho_\eta + k_G |\partial \psi(c^T \eta) c^T|) \\ -\frac{1}{2}(\rho_\eta + k_G |\partial \psi(c^T \eta) c^T|) & \omega_u \end{bmatrix} > 0$$

Next, by Sylvester's criterion, the above matrix is positive-definite provided that its leading principal minors are positive. For the first minor is

$$\rho_\eta |\lambda_{pf}| > 0 \iff \boxed{\rho_\eta > 0} \tag{3.13}$$

For the second minor we get

$$\omega_u |\lambda_{pf}| \rho_\eta - \frac{1}{4}(\rho_\eta + k_G |\partial \psi(c^T \eta) c^T|)^2 > 0$$

which can be written in the following way

$$\omega_u |\lambda_{pf}| \rho_\eta - \frac{1}{4}\rho_\eta^2 >$$
$$\frac{1}{2}k_G |\partial \psi(c^T \eta) c^T| \rho_\eta + \frac{1}{4}k_G^2 |\partial \psi(c^T \eta) c^T|^2. \tag{3.14}$$

The above inequality can by met by making the RHS terms arbitrarily small by setting $0 < k_G \ll 1$. On the other hand, the LHS can be positive if the following condition is met:

$$\boxed{4\omega_u |\lambda_{pf}| > \rho_\eta}. \tag{3.15}$$

Therefore, we conclude that the reduced-order system satisfies $\dot{V} \leq -\bar{\lambda}V$ for some $\bar{\lambda} > 0$, by selecting $\rho_\eta, k_G > 0$ that satisfy

1. $\rho_\eta < 4\omega_u|\lambda_{pf}|$.

2. k_G is sufficiently small.

exponential stability of the reduced system. The exponential decay of the differential Lyapunov function guarantees incremental exponential stability of the reduced system, [57, Theorem 1]. This implies exponential stability of the equilibrium of the reduced system.

Remarks: The above proof can account for

- **Arbitrary topologies:** this means that a stability conditions shall apply also for real dendritic morphologies, which are the topic of focus of chapter 5.

- **Lateral diffusion:** although lateral diffusion was not implemented (this resembles trafficking among the g species), it does alter the stability condition since the (linearized) dominant eigenvalue will not be effected. The biological influence, however, is discussed in the following chapter.

- **Nonlinear trafficking rates:** a linear trafficking model was adapted for AMPA receptor. In chapters 7 and 9, we consider more complicated models of transport, such as $v_{ij} = v_f(c_j - m_j)$ where c_i now models compartment j capacity, that incorporate saturation and crowding effects.

Chapter 4

Analysis of the closed loop synaptic scaling model

"Any man could, if he were so inclined, be the sculptor of his own brain."

Santiago Ramon y Cajal, *Advice for a Young Investigator*

We define three relevant performance measures to investigate the physiological effects of particular variations in **CLSS** model parameters. We show that there is an inevitable tradeoff among these performance measures.

4.1 Defining performances

We start by defining three performance measures that will be used to elucidate how activity-dependent (local and global) mechanisms alter the behavior of the system. The three measures are: robustness, convergence rate, and accuracy of synaptic scaling. Here, we will use robustness to capture and quantify the stability of the system. This property will assess the system's ability to handle uncertainties. Convergence rate captures how fast the system reaches its steady-state. Accuracy captures how well the synaptic strength, i.e. its efficacy, responds to potentiation.

4.1.1 Robustness of the scaling model

Robustness pertains to the stability of the model and to its preservation under potential system perturbations (parameters variations, dynamic uncertainties, disturbances). At the

formal level, the stability margin introduced in Chapter 2 provides an exact quantification of robustness. The stability margin measures the distance of the Nyquist curve from the point -1. Why is this a measure of robustness? Using the Nyquist criterion, this tells us how much we can perturb the system before losing stability in closed loop. In fact, the perturbation of the system induces a deformation on its Nyquist curves. Therefore, a larger distance from the point -1 means that a larger perturbation is needed to destabilize the closed loop. In this sense, a system with a large stability margin is "far away" from instability and can cope with larger perturbations.
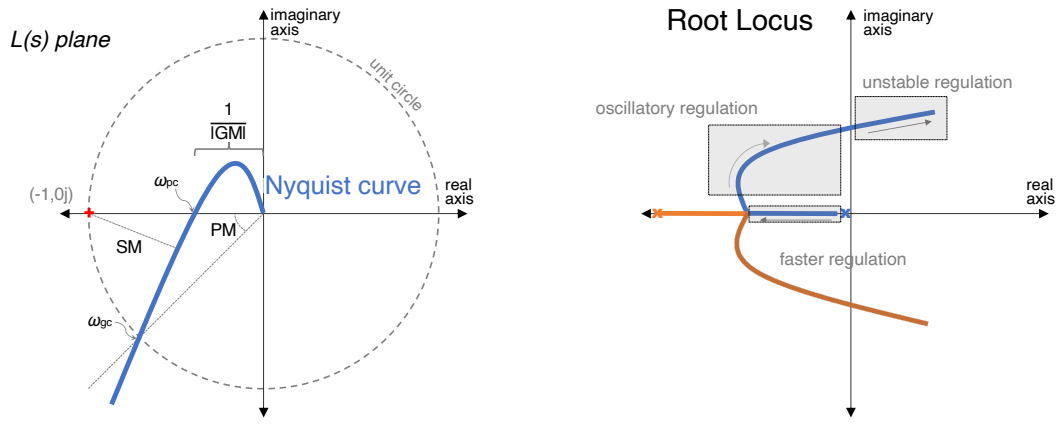
(a) A Nyquist plot showing the stability margins.   (b) Movement of dominant eigenvalues.

Fig. 4.1 Frequency-domain geometric definition of different margins (left) and root-locus of the linearized system showing regions of stable, oscillatory, and unstable regulation.

4.1.2 Convergence rate

This attribute is related to how fast the system reaches its steady state. For linear systems, this is determined by the real part of the right-most eigenvalue. Since the CLSS model is nonlinear, we will use the eigenvalues of the linearized system at equilibrium. These captures the convergence properties of the system trajectories in a neighborhood of the equilibrium. This reads

$$\bar{\lambda} = \mathrm{Re}\left(\min_{i \in n}\{\lambda_i \in \Lambda\}\right) \tag{4.1}$$

where Λ is the set of eigenvalues of the linearized closed loop synaptic scaling model around its fixed point. Figure 4.1b shows how the eigenvalues of the linearization moves as a function of the gain k_G of the global feedback mechanism.

For small gain of the negative feedback the two rightmost eigenvalues of the linearization moves towards each other, as shown by the blue and red branches in Figure 4.1b. From a behavior point of view, this means that the closed loop becomes faster, that is, trajectories are faster to converge to steady state. With a further increase of the gain k_G, the two eigenvalues coalesce and bifurcate becoming complex conjugate. From the behavior point of view, the system trajectories converges to steady state but with small oscillations. The system has reached the limits of performances above which the behavior deteriorates. In fact, a further increase of the feedback gain leads to a loss of stability, when the two eigenvalues cross the imaginary axis. The system becomes unstable.

These feature of the root locus are structural, that is, they can be reproduced for any parameter selection. This shows the limitation of the global feedback mechanisms in improving performance. At technical level, the gain at which the system loses stability, that is, the gain at which the eigenvalues cross the imaginary axis corresponds to the gain at which the Nyquist locus in Figure 4.1a touches the point -1.

4.1.3   Accuracy of scaling and potentiation

Accuracy captures the preservation of relative strength between synapses. This is a fundamental feature for synaptic scaling. To quantify such a feature, we introduce expressions that monitor synapses strengths before and after potentiation and depression. First, prior to LTP/LTD, the steady states of all non-potentiated synapses g_i^{ss} are recorded and averaged as follows:

$$\mu^{ss} = \text{mean}(g_{\text{unpot}}^{ss}).$$

μ^{ss} is the mean active cargo content of all non-potentiated synapses. We normalize all g_i^{ss} by the mean μ^{ss}. We then compute the steady state mean following LTP/LTD: $\hat{\mu}^{ss}$, indicated by ˆ. We compare the quantity g_i^{ss}/μ^{ss} between the pre- and post-LTP states. A synapse that scales perfectly will preserve the relative strength with respect to other (unponetiated) synapses, mathematically this is expressed as:

$$\frac{g_i^{ss}}{\mu^{ss}} = \frac{\hat{g}_i^{ss}}{\hat{\mu}^{ss}} \qquad \text{and} \qquad q_i = \frac{\hat{g}_i^{ss}/\hat{\mu}^{ss}}{g_i^{ss}/\mu^{ss}} - 1 = 0 \tag{4.2}$$

where q_i measures scaling deviation for each individual synapse (Figure 4.2). $q_i < 0$ indicates excess scaling during LTP or incomplete scaling during LTD. While $q_i > 0$ corresponds to incomplete scaling during LTP or excess scaling during LTD. We can use the q_i's to compute
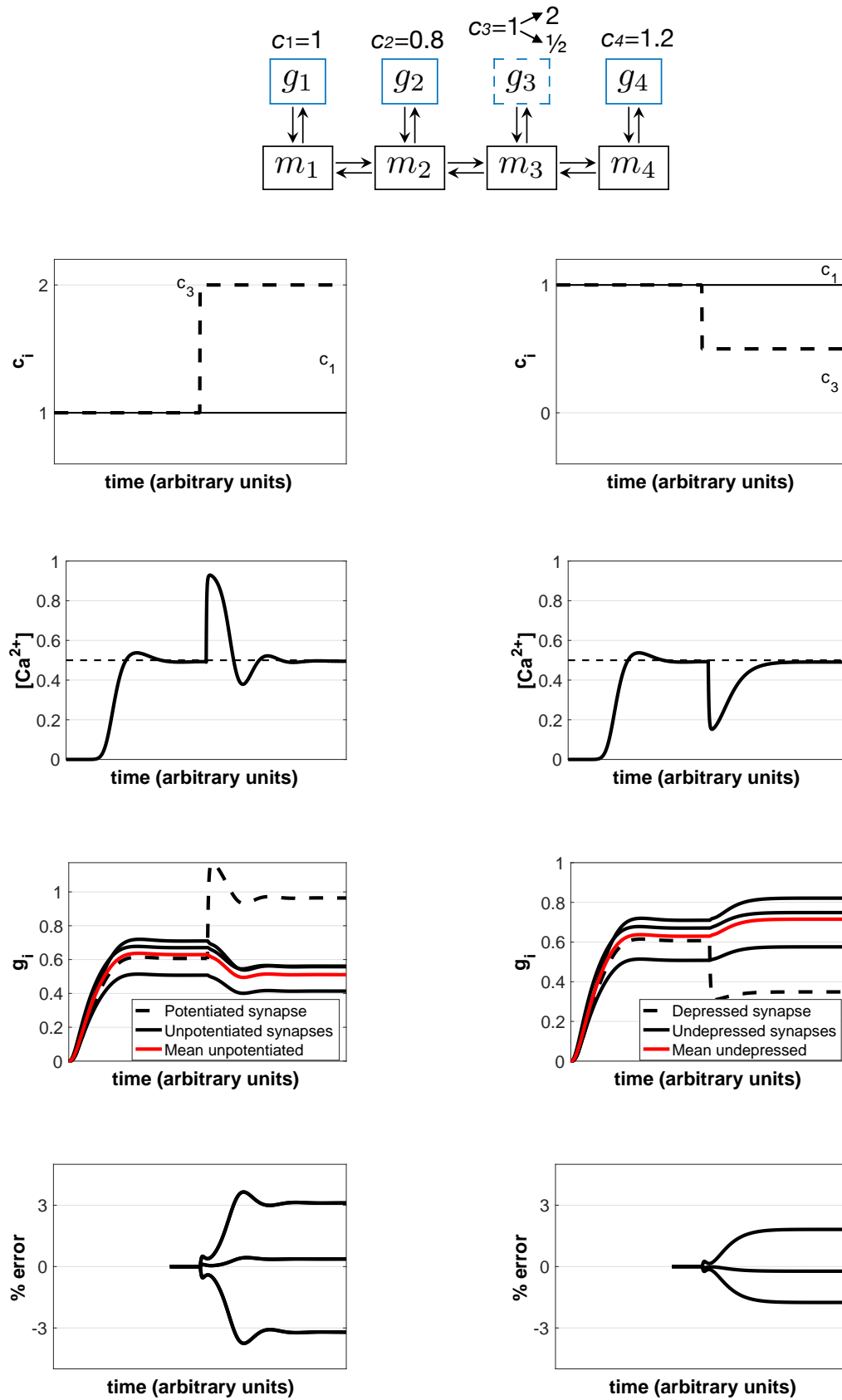
Fig. 4.2 A 4−compartmental neuron model undergoing LTP(left) and LTD(right).

mean absolute percent error Q from perfect scaling:

$$Q = \text{mean}(|q_i|) \times 100\% \tag{4.3}$$

Larger Q indicates a greater deviation from perfect scaling, i.e. more inaccurate synaptic scaling.

4.2 Navigating the tradeoffs

Now we show that improving any of the three performance attributes above results in worsening one or the other two. We do this by varying the following free parameters

- The global controller sensitivity k_G

- The local controller sensitivity k_L

- The detachment/inactivation rate s_{-i}

4.2.1 k_G mediates between robustness and convergence rate

The sensitivity of the global controller k_G to changes in average calcium mediates the system robustness and convergence rate of synaptic scaling. Figure 4.4 (left) shows $[\text{Ca}^{2+}]$ responses for different k_G values. As k_G increases, $[\text{Ca}^{2+}]$ reaches faster its steady state. Above a certain threshold, dampened oscillations appear. These decaying oscillations shows that the feedback mechanism has reached its performance limit. A further increase on k_G leads to oscillations.

k_G can be also correlated to the system stability margin, that is, to its robustness. To quantify robustness, we evaluate feedback regulation in a simplified model—a single compartment with two states m and g for inactive and active cargo, respectively. A third state u represents cargo production. Strength of global control is mediated by gain k_G. This three-dimensional system is described by the following equations:

$$\dot{m} = u - s_1 m(c - g) + s_{-1} g - \omega_m m$$
$$\dot{g} = s_1 m(c - g) - s_{-1} g - \omega_g g.$$
$$\dot{u} = k_G([\text{Ca}^{2+}]_{target} - [\text{Ca}^{2+}]) - \omega_u u$$
$$[\text{Ca}^{2+}] = h(g_{avg}).$$

The connections between the linearized subsystems are summarized in the block diagram in Figure 4.3(right) and briefly described here. The model has a preset $[Ca^{2+}]_{\text{target}}$ that is summed with $[Ca^{2+}]$ to produce an error signal, e_G. The block G_u outputs cargo production u, block G_m transports cargo throughout the dendrites, and block G_g activates cargo by insertion into dendritic spines. Active cargo g then feeds back to modify $[Ca^{2+}]$.

As mentioned before, the Nyquist criterion predicts the stability of the closed loop system from studying the open loop system. Using the linearization of the three dimensional system above, this means that we can study the product $L = \partial h G_g G_m G_u$ to predict the behavior in closed loop. In particular, the stability margin measures the distance from instability. Increasing the gain k_G reduces this distance, as shown in Figure 4.4(right). This illustrates the role of the gain k_G in modulating between convergence rate and robustness.

Why does the stability margin, i.e. the distance from instability, provide a good measure of robustness? The idea is that the eigenvalues of the closed loop system are given by the root of the polynomial

$$1 + L$$

and these roots will have negative real part only if the Nyquist locus of L passes to the left of the point -1. Instability occurs when the Nyquist locus of L passes through the point -1. When this happens, we have

$$1 + L(j\omega) = 0$$

which means that $j\omega$ is a root of the polynomial, that is, an eigenvalue of the closed loop system. As a result, the closed loop system is marginally stable and an infinitesimal perturbation makes the system unstable. The previous analysis imposes the first constraint or tradeoff: *there is a hard limit to how quickly a neuron can produce and transport cargo before it becomes unstable.*

Robustness against static and dynamic uncertainties

Biological organisms and the cells within them are highly complex with significant variabilities. These include the variance in microscopic parameters, genetic mutations, environmental changes, structural/morphological differences, perturbations in neural excitability, etc. Uncertainties are therefore ubiquitous in biological systems. Experimental studies have shown that biological systems show a degree of robustness against a number of uncertainties [92, 53]. Hence, robustness is an intrinsic property of biological systems. For the **CLSS** model, we demonstrate its robustness against perturbations. We show that it tolerates two distinct types of uncertainties or perturbations.
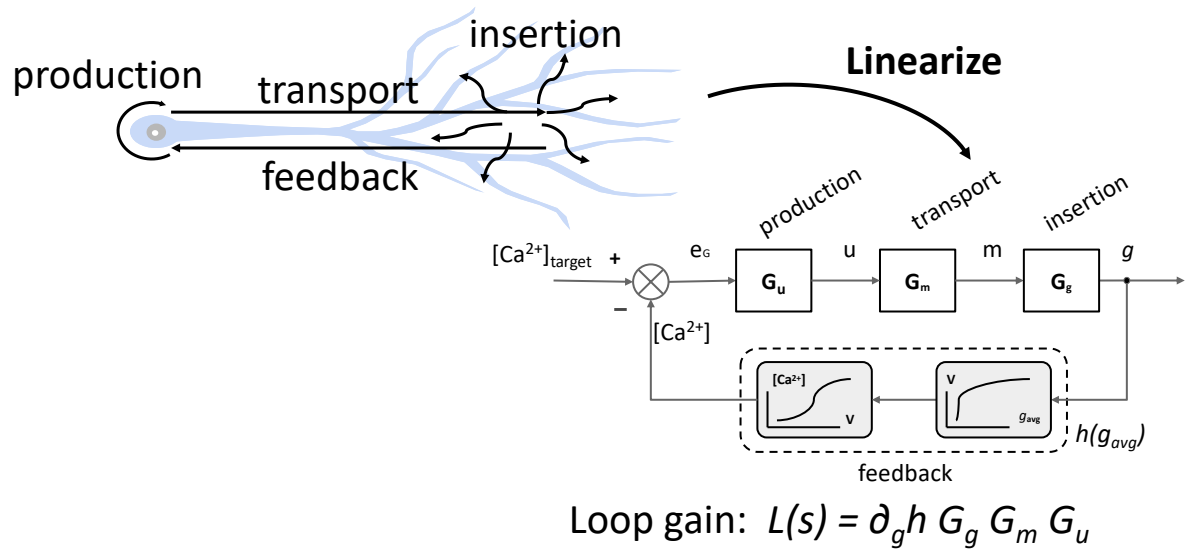
Fig. 4.3 First step is to linearize the constituent dynamics of the **CLSS** model and construct the loop gain $L(s)$.
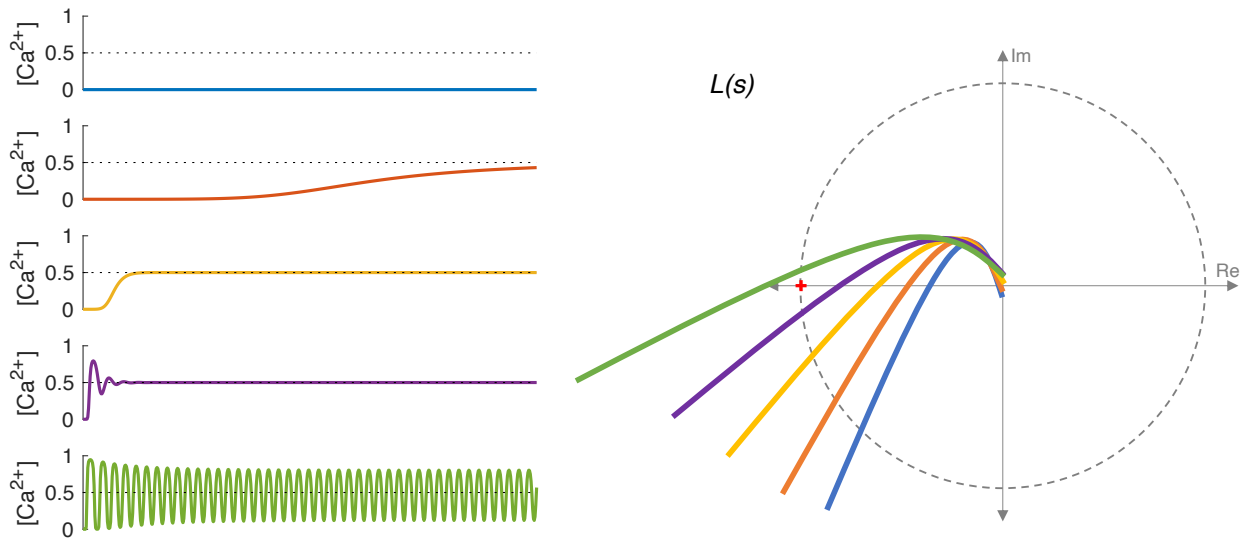

Fig. 4.4 Second step is to plot Nyquist curves and compute the stability margins.

- **Robustness to parametric variations:** the first type of robustness is the robustness to parametric variations—also called static uncertainties. Here, the system achieves homeostasis despite variations in the model parameters. For example, trafficking rates v_f and v_b depend on the number and type of protein motors attached to the cargo, which vary the effective velocity of the motor-cargo complex. Further, a number of experimental studies showed that AMPA receptor degradation ω_m is an activity-dependent process and thus a variable parameter [47][1]. Synaptic potentiation and a synapse's geometrical/structural properties c_i also vary with presynaptic input or LTP/LTD. We show that the system shown in Figure 4.5a is robust for generous parameter ranges by ensuring that the family of transfer functions never encircles the $(-1, j0)$ point. The parameter ranges are Although the steady state varies in each case,

<div align="center">

Table 4.1 Parameter Ranges

parameter	minimum	maximum
$v_f \; [\mu m s^{-1}]$	0.5	2
$v_b \; [\mu m s^{-1}]$	0	1
$\omega_m \; [s^{-1}]$	0.002	0.2
c_i	1	5
$d \; [\mu m s^{-1}]$	0.1	1
n (length) $[\mu m]$	3	15

</div>

the system adapts and homeostasis is achieved. The model can withstand a substantial amount of parameter variation. Low w_m corresponds to the least stable, most fragile system, because degradation acts as leak or dissipation in the system, which prevents accumulation of cargo. Increased dissipation makes the system more robust, allowing for more aggressive synaptic scaling (higher k_G).

- **Robustness to unmodeled dynamics:** a system can also be robust to dynamic uncertainties, which guarantees that the model behavior is preserved against unmodeled dynamics. Unmodeled dynamics are a result of the assumptions made during the model formulation process. To assess this type of uncertainty, we use the system gain, H_∞ norm, and the small gain theorem [41, 170, 11]. We will use the system's robustness to dynamic uncertainties to show that behavior is independent of system dimension. This validates our analysis of toy neuron models as representative of more detailed, higher dimension systems.

---

[1]We expand on this in Chapter 6.

To assess the system's robustness to dynamic uncertainties, we will focus on the transport dynamics that describes AMPAR trafficking. To this end, we construct the mismatch system Δ, which is computed using the difference between a nominal and a detailed (higher dimensional) system. The nominal system Σ_3 is a 3-compartmental system, while Σ_N is a system of of dimension N with $N \in \{3, \ldots, 100\}$. As N increases, Σ_N captures the transport dynamics with high resolution. Then, we define the mismatch system as

$$\Delta := \Sigma_3 - \Sigma_N,$$

where Σ_3 is described by

$$\dot{m}_1 = u - v_f m_1 + v_b m_2$$
$$\dot{m}_2 = v_f m_1 - (v_f + v_b) m_2 + v_b m_3$$
$$\dot{m}_3 = v_f m_2 - v_b m_3$$

and Σ_N is described by

$$\dot{m}_1 = u - \bar{v}_f m_1 + \bar{v}_b m_2$$
$$\dot{m}_i = \bar{v}_f m_{i-1} - (\bar{v}_f + \bar{v}_b) m_i + \bar{v}_b m_{i+1}$$
$$\dot{m}_N = \bar{v}_f m_{N-1} - \bar{v}_b m_N.$$

In the dynamics of Σ_N, $\bar{v}_f$ and $\bar{v}_b$ are the scaled forward and backward trafficking rates, respectively, and their scaling follows the rule introduced in (7.9). Lastly, we compute the H_∞ norm of the system. The H_∞ norm measures the distance between the peak gains of the two systems Σ_3 and Σ_N, which represents the worst case amplification over the range of frequencies. This plot, depicted in Figure 4.5b (discretization), saturates at 1.02, which guarantees unchanged behavior if the 3-dimensional model is replaced with a more detailed, higher dimensional one with up to 100 compartments.

The same principle of robustness to dynamic uncertainties can guarantee that the overall behavior is preserved when the system is interconnected with another system. For example, we can show that the system is robust and maintains the same behavior if the species m is replaced with a more detailed description considering a more detailed synthesis step that involves another species, such as Arc mRNA. In other words, this process demonstrates that lumping parameters does not drastically affect the observed phenomena. This is also applicable in showing system robustness when considering cytoplasmic diffusion, which will be discussed later. We return to this matter at the end of this chapter.
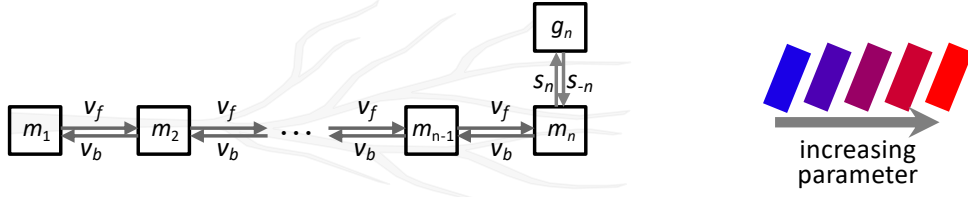
(a) Abstract neuron model (left) and legend (right).
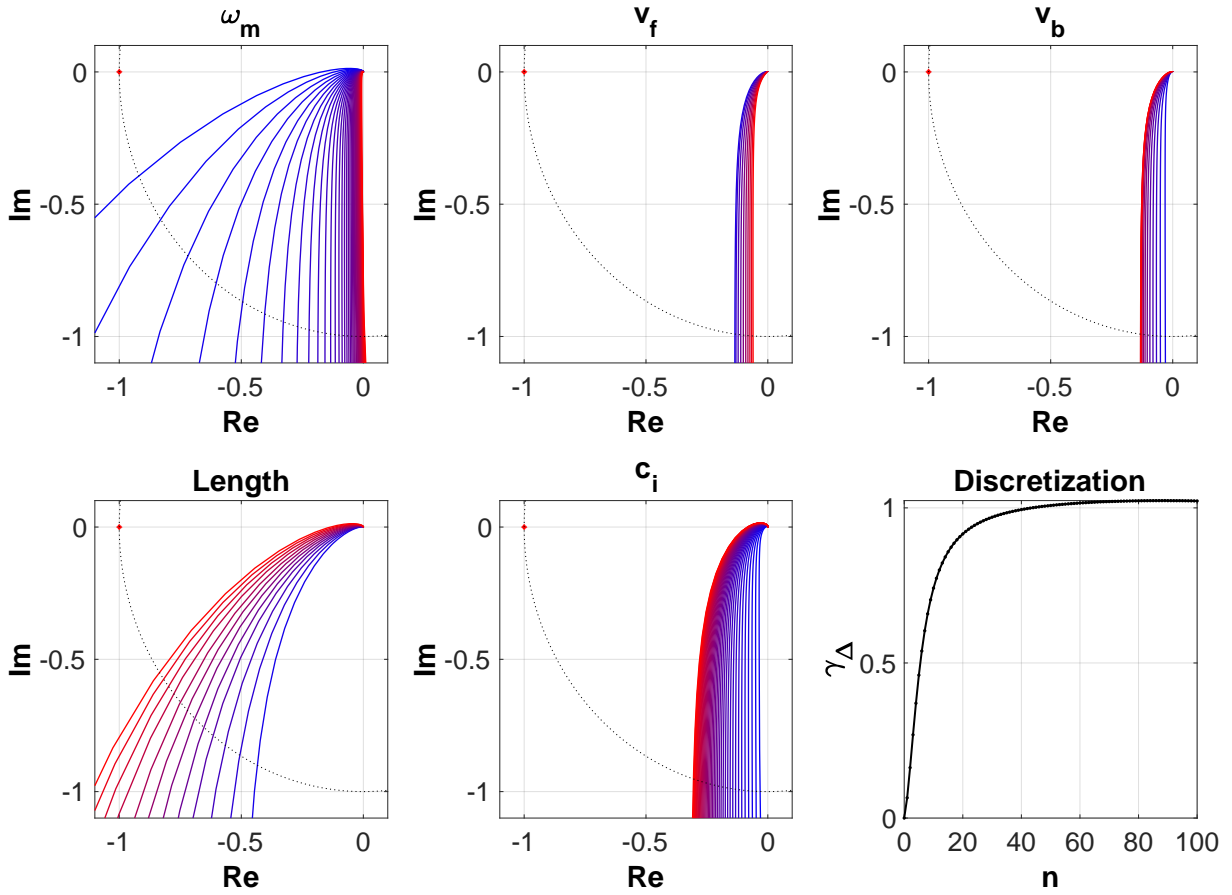
(b) Family of Nyquist plots generated for ranges of parameters values.

Fig. 4.5 Robustness of the **CLSS** model against static and dynamic uncertainties.

4.2.2 s_{-i} **mediates between accuracy of scaling and convergence rate**

We assess how well a neurite can potentiate its synapses at varying locations in the dendritic tree. To this end, we compare potentiated synapses to equivalent unpotentiated compartments on identical branches (Figure 4.6). We potentiate single synaptic compartments with varying

strength and at varying distances from the soma. We calculate accuracy of synaptic potentiation as percentage of full potentiation, which corresponds to how well a synapse meets its demand for increased AMPARs.
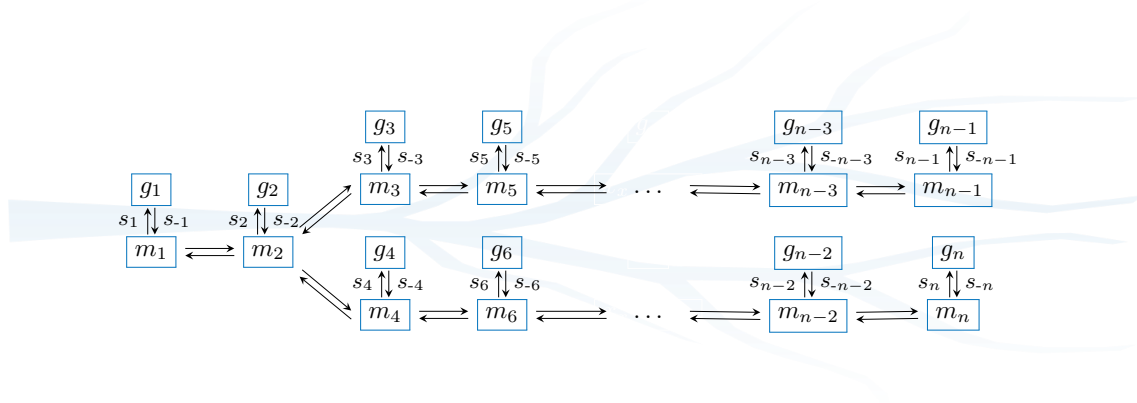
Fig. 4.6 Abstract neuron model with symmetric branches.

In Figure 4.8 we vary the pool size by varying s_{-i}. For a small internal pool (small s_{-i}) a neuron only fulfills half the demand for increased AMPARs in distal synapses. Reserve AMPAR count dwindles with distance from the AMPAR source, and the demand of synaptic potentiation is not achieved. Neurites with increasing internal pool (large s_{-i}) size more readily fulfill demand during LTP, thus improving accuracy of potentiation. This can be shown analytically by studying the transport equation from (3.3) at steady-state. Let $M = \Sigma m_i$ be the pool size, then the first part of equation (3.3) can be rewritten as

$$\dot{M} = u - \Sigma s_i m_i (c_i - g_i) + \Sigma s_{-i} g_i - \omega_m M$$

and the pool size at steady-state M^* from the above expression as

$$M^* = \frac{u + S_- \bar{G}^*}{\omega_m + \Sigma p_i s_i (c_i - g_i^*)}$$

where we used the fact that at steady-state $m_i^* = p_i M$, $p_i < 1$ for all i and $\Sigma p_i = 1$, and substituted $S_- = \Sigma s_{-i}$ and $\bar{G} = \Sigma g_i$. Thus, the above steady-state relation shows that increasing s_{-i} increases the pool size at steady-state, subsequently improving the accuracy of scaling. By increasing s_{-i}, synaptic AMPARs (g_i) are more likely to end in the dendritic pool which means that they will undergoing more transport, thereby increasing their chances in ending in distal sites (since $v_f > v_b$). This mitigates the disadvantages of location-dependent distribution of receptors. The explanation is depicted in Figure 4.7. The simulations in Figure

4.8 shows the steady-state profile of functional AMPARs of the neuron shown in Figure 4.6. Indeed, increasing inactivation rate s_{-i} normalizes the steady-state profile g. Despite the change in the equilibrium as a result of varying s_{-i}, feedback ensures that homeostasis is achieved.
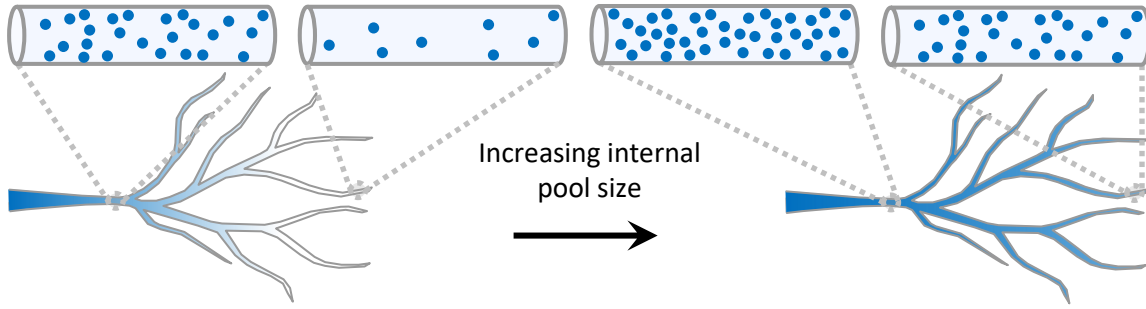
Fig. 4.7 Increasing pool size by increasing s_{-i}.

Nevertheless, there is a penalty of increasing the settling time, as shown in Figure 4.9. Improved scaling comes at the expense of settling time. Although increasing s_{-i} improves the accuracy of scaling, it makes it longer to achieve homeostasis. This can be understood in the same way it improves scaling. Increasing s_{-i} increases the propensity of g_i to end up in the pool. At steady-state,

$$g^* = \frac{m_i s_i c_i}{m_i + s_{-i} + w_i^g}.$$

Hence, synaptic AMPARs reduces with increasing s_{-i}. This, in turn, results in a slower regulation process due to insufficient g_{avg}.

Impact of morphology on accuracy of scaling

Synaptic scaling allows a neuron to maintain the relative strengths of its synapses following potentiation. We next explore how morphology impacts the accuracy of scaling, in addition to varying variation in the internal pool size . During scaling, neurons undergo multiplicative changes in synaptic strength such that the relative strengths of the synapses are preserved. Stable, reliable changes at the molecular and cellular level correspond to stable, reliable memories, which motivates quantifying accuracy of synaptic scaling. Our measure of accuracy of synaptic scaling, introduced earlier, is the mean absolute percent error in scaling ratio (which we term Q) following a scaling event (LTP or LTD).

To further unpack the impact of morphology, we compare Q for varying internal pool sizes and potentiation ratios in distinct neuron morphologies. We examine linear and stellate
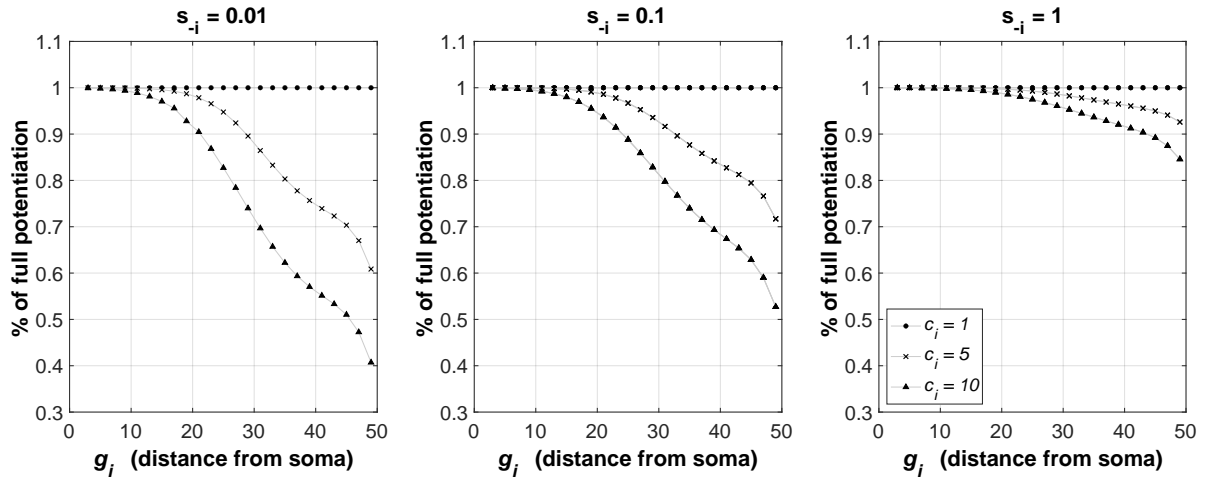
Fig. 4.8 Steady state spatial profile of g_i for different s_{-i} and c_i values.
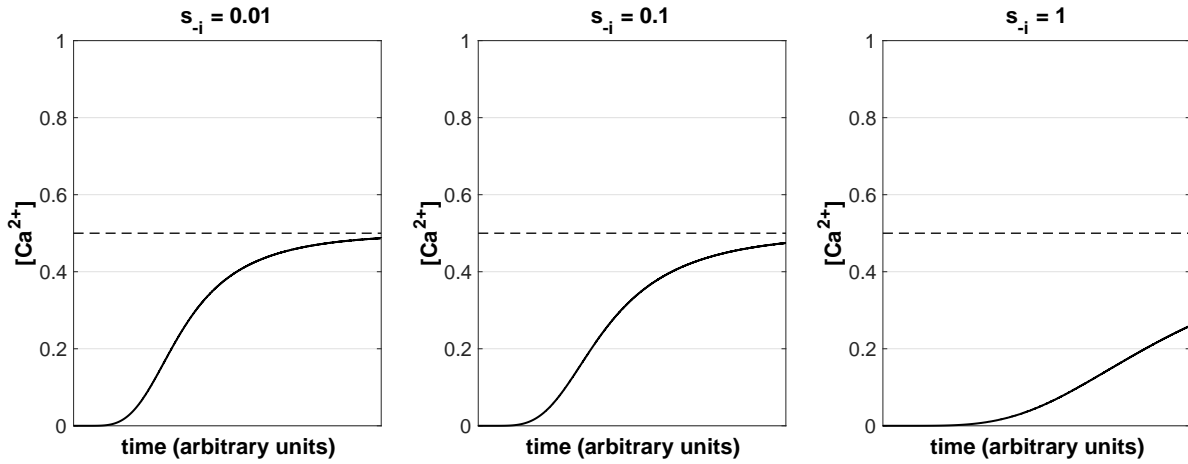
Fig. 4.9 Response of $[\text{Ca}^{2+}]$ for different s_{-i} values. c_i is fixed at 1.

architectures—the extreme cases of structural symmetry, depicted in Figure 4.10. In both, m_1 is the soma and site of AMPAR production and global regulation. Model parameters are scaled such that AMPARs are transported at 1 µm/s and the linear and stellate models are 1000 µm in length and 250 µm in radius, respectively. In the symmetric, stellate model, each compartment has proximate access to the soma with minimal transport of scaling signal and AMPARs. In this geometry, all the synapses have equal and identical access to internal pool of AMPARs. The symmetry of the structure forces a symmetry in the dynamics. This ensures in cases when a subset of synapses are subjected to an LTP/LTD event, then the rest of the synapses in the network are affected equally. In this way relative strengths are preserved, and this constitutes the ideal situation where the effect of transport (and hence morphology) is minimized.

On the other hand, in the asymmetric, linear model, the effect of transport and resultant phase lag increases, particularly for distal compartments. Unlike the symmetric case, each synapse has access to a different internal pool size. Here, the effect of transport is accentuated: closer synapses to the soma have access to larger internal pool. This means that proximal synapses scale better than distal ones as the internal pool size decreases with distance away from the soma. This results in significantly reduced scaling accuracy in asymmetric morphologies (Figure 4.11).
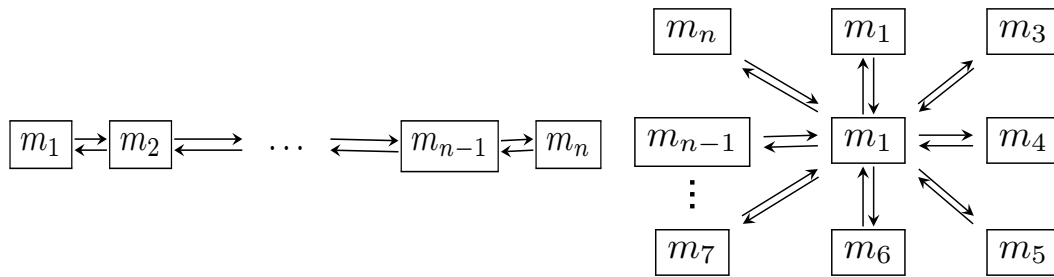
Fig. 4.10 The morphologies, linear morphology (left) and a star one (right), represent the two extreme cases. The line is the asymmetric case, where the star is symmetric one.

The two networks in Figure 4.10 represent two extreme cases where one minimizes and the other maximizse the effect of transport. In both cases, scaling accuracy decreases with increasing potentiation ratios. Higher demand for AMPARs results in scaling error. Scaling accuracy also increases with larger internal pools. Nevertheless, the settling time takes longer as s_{-i} increases, deteriorating the convergence rate. This imposes the second tradeoff: *improving the scaling accuracy comes at the expense of how fast the neuron delivers AMPARs to demand sites*.

4.2.3 k_L mediates between robustness and accuracy of scaling

The sensitivity of the local controller to changes in calcium concentration also alter the behavior. We simulate a $10-$compartmental system that experience potentiation in half of its compartments, depicted in red in Figure 4.12. The simulations are done with a relatively high global regulation sensitivity k_G, apparent by the oscillatory transient response, shown in Figure 4.12a.
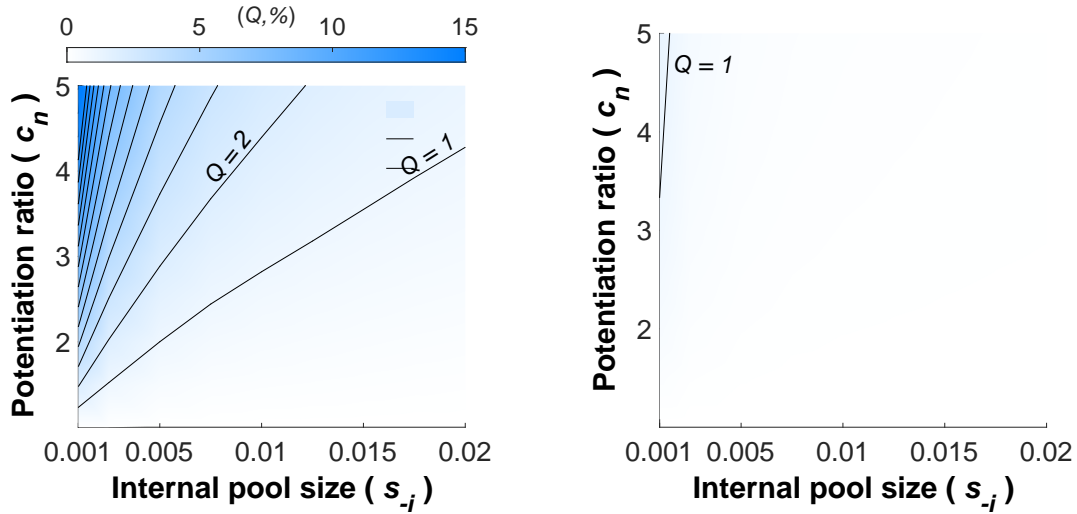
Fig. 4.11 The linear and star morphologies, shown in Figure 4.10 are simulated for varying c_n and s_{-i} while quantifying mean absolute percent error Q. More accurate synaptic scaling is achieved in symmetric morphologies.

The absence of local control results in synaptic scaling with moderate accuracy and oscillations. The red synapses strengthen, as expected during LTP. The unpotentiated, black compartments are scaled down, which is notable because the synaptic capacity of these compartments was not changed. Figure 4.12a validates that synaptic scaling works with global control alone. Note that the relative weights of the synapses are preserved with moderate accuracy. Further, the difference between potentiated (red) and unpotentiated (black) synapses is prominent.

If we introduce local regulation at low gain (Figure 4.12b), the oscillations are improved at the cost of accuracy. The difference between potentiated and unpotentiated synapses begins to diminish. If we increase the local gain (Figure 4.12c), the oscillations are eliminated and the system is fully stable now. However, synaptic scaling is no longer accurate, and red synapses hardly increase compared to the black ones. The degree to which local regulation can improve stability is limited by a reduction in accuracy of synaptic scaling. This suggests the third tradeoff: *the sensitivity of the local regulation mechanism mediates between the robustness of the system and accuracy of synaptic scaling*.

(a) $k_L = 0$.   (b) $k_L = 0.3$.   (c) $k_L = 0.5$.
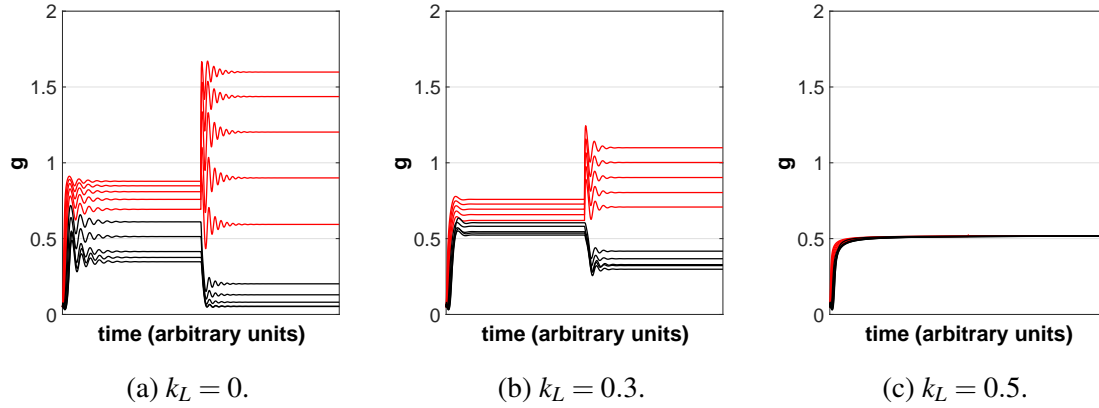
Fig. 4.12 Increasing the sensitivity of the local regulation mechanism improves the robustness of the system at the cost of scaling accuracy.

4.3 Overall performance tradeoffs

We have discussed the tradeoffs involved in balancing the system's robustness, convergence rate, and accuracy of synaptic scaling. We have shown how to quantify these attributes. Using these measures, we provide a summary of these tradeoffs, as shown in Figure 4.13.

We simulate a simplified $4-$compartmental model with distributed LTP, and performed the following

1. The stability margin reflects robustness, the convergence rate reflects the settling time, and the reciprocal of mean absolute percent error (Q^{-1}) reflects accuracy.

2. We sweep through parameter k_G to vary global regulation that modulates the robustness-convergence rate tradeoff. We then sweep through parameter k_L to vary local regulation that modulates the robustness-accuracy tradeoff. Lastly, we sweep through parameter s_{-i} to vary internal pool size that modulates the convergence rate-accuracy tradeoff.

3. The axes for each tradeoff are adjusted to cover the stable regulation region, characterized by real eigenvalues of the first order linearization. Beyond the limits of these axes, the system is unstable and has oscillations.

Each tradeoff is hyperbolic in shape, suggesting a negative correlation. From a system-theoretic perspective this means that no attribute can be improved without worsening at least one of the other attributes. Furthermore, no modification to the system can simultaneously improve all attributes.

4.4   Chapter summary and concluding remarks

This chapter can be summarized in the following key points:

1. The sensitivity of the global regulation k_G mediates between the system robustness and convergence rate.

2. The internal pool size, which is intimately linked to s_i, mediates between the convergence rate and accuracy of scaling.

3. The sensitivity of the local regulation k_L mediates between the accuracy of scaling and system robustness.

4. The **CLSS** model is robust against static and dynamic uncertainties, with maximum fragility arising from variation in the degradation rates.

5. The trafficking of AMPARs significantly constrains the performance of the neuron.

The objective of the closed loop model is the maintenance of average neuronal activity, or homeostasis. This is achieved via the negative feedback regulation of active AMPA receptors, or g_i. The aforementioned description interprets species m and g as pre-protein and protein, which are inactive and active in synapses, respectively. Nevertheless, the model at hand has the capacity to be interpreted as number biological molecules and processes. For example, m and g can model other ionotropic glutamate receptor, such as NMDA receptors.

In general m can be interpreted as ion channel precursor that is only produced in the soma, and transformed into functional ion channels in designated compartments g_i. Channels are synthesized at the cell body then trafficked (chapters $3 - 5$). An alternative interpretation of the model is that m represents mRNA and its transport within the neuron. Then, channels g are synthesized locally. This interpretation is explored and adopted in chapters 6-8. There is mixed biological evidence for whether the trafficked precursor is mRNA or protein. However, this does not affect our model at our chosen level of abstraction.

As mentioned in the introduction, a number of molecules could be involved in the scaling process and there might be other key players, beside AMPARs. Experimental studies have suggested that Arc protein is the global scaling signal dissipated throughout the dendrites in response to changes in neural firing rate [142, 141, 151, 31]. In our modeling we lump the transport of the scaling signal with AMPAR trafficking. Our modeling assumption is reasonable since AMPARs and Arc are trafficked at similar rates [158]. To further evaluate this assumption, we also perform simulations with Arc protein as a separate communication channel to validate that lumping of the scaling signal with AMPAR trafficking produces similar results.
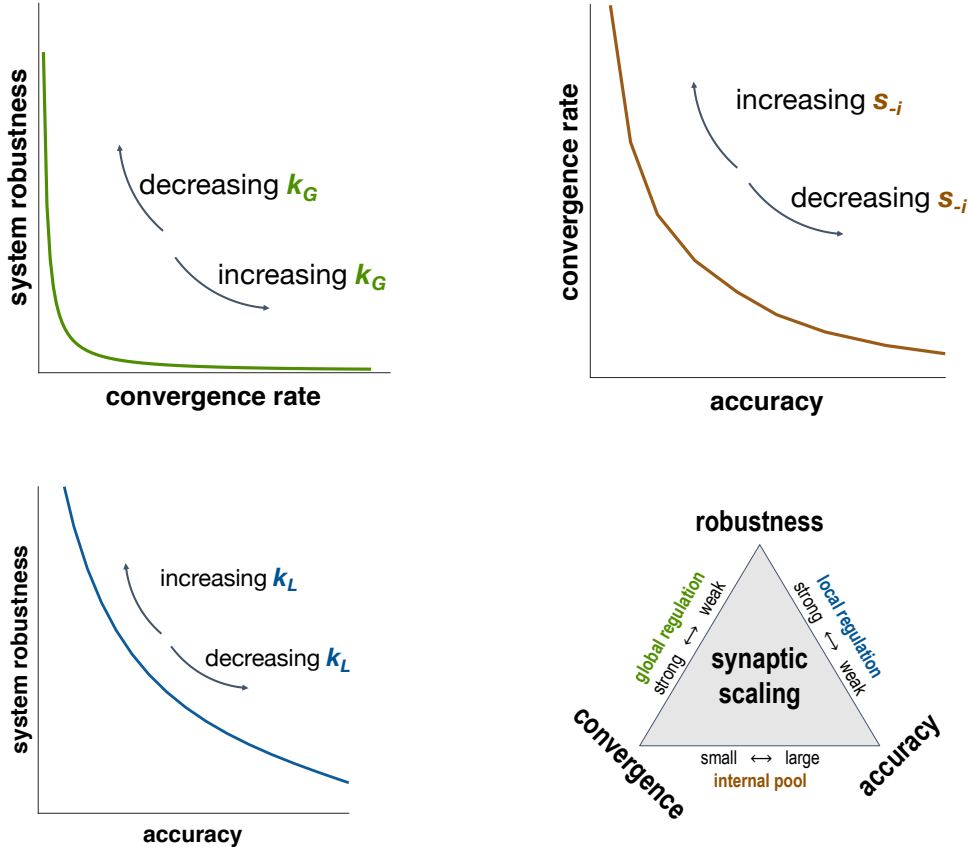
Fig. 4.13 The tradeoffs are summarized in a toy model by rigorously quantifying each attribute: The stability-efficiency tradeoff is mediated by tweaking k_G, the stability-accuracy tradeoff is mediated by tweaking k_L, the efficiency-accuracy tradeoff is mediated by tweaking s_{-i}.

In a variant of the model, we assume that Arc protein is a separate communication channel for global signaling (Figure 4.14). This introduces Arc protein as another species a. In this system, the global controller regulates production of both m and a with some bias $m : a$. This modified system has the following dynamics:

$$
\begin{aligned}
\dot{m}_i &= \delta u + f(m_i) - k_i m_i a_i - \omega_m m_i \\
\dot{a}_i &= (1 - \delta)u + f(a_i) - k_i m_i a_i - \omega_a a_i \\
[\dot{ma}]_i &= k_i m_i a_i - s_i [ma]_i (c_i - g) + s_{-i} g - \omega_{[ma]} [ma]_i \\
\dot{g} &= s_i [ma]_i (c_i - g) - s_{-i} g - \omega_g g.
\end{aligned}
$$
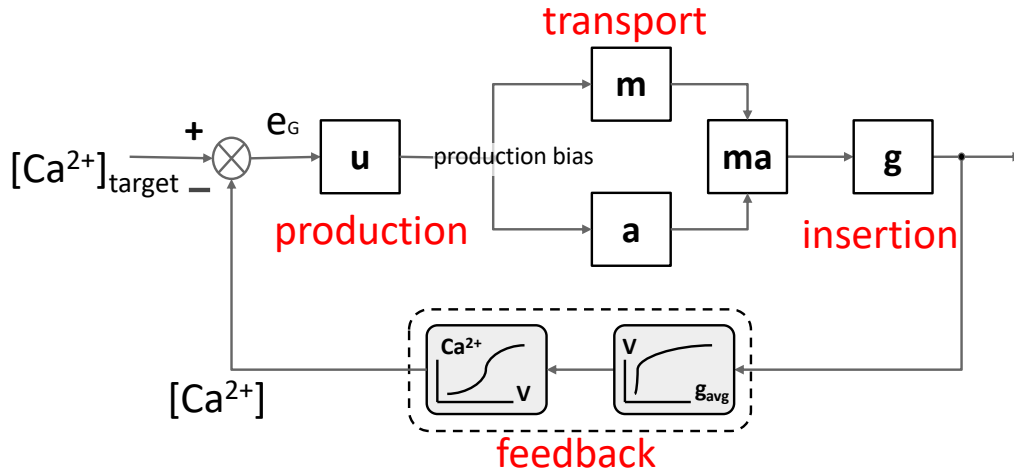
Fig. 4.14 Block diagram of closed loop model with additional species *a* for Arc. The global regulator produces both inactive AMPARs *m* and Arc *a* with some production bias *m* : *a*.

where [*ma*] is a complex containing both *m* and *a*. The remaining model dynamics for this variant are unchanged. The modified block diagram is shown in Figure 4.14. The tradeoffs are preserved, as shown in Figure 4.15. This is reassuring since the **CLSS** model, although fairly simple, can indeed capture the same qualitative characteristics of the same scaling phenomena if modeled with more species and higher level of complexity.
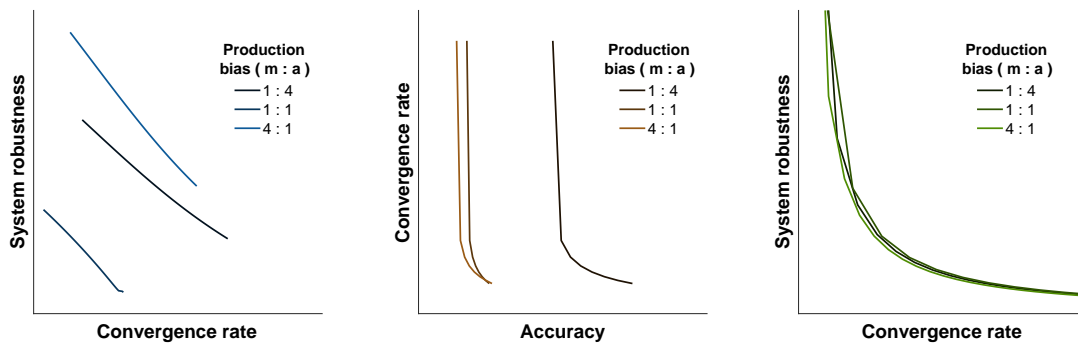
Fig. 4.15 All three tradeoffs are replicated in the Arc system. Production bias is indicated by different lines.

Up to this point, we have studied abstract neuron models with relatively simple topologies. However, neurons distinct themselves from other cells in their highly complex dendritic trees that vary in size and structure. Are the tradeoffs between the three performance attributes preserved in real morphologies with realistic parameters?

Chapter 5

Real dendritic morphology effects on synaptic scaling

"The brain is the last and grandest biological frontier, the most complex thing we have yet discovered in our universe. It contains hundreds of billions of cells interlinked through trillions of connections. The brain boggles the mind."

James D. Watson, *Discovering the Brain, National Academy Press, 1992*

In this chapter we apply the **CLSS** model to dendritic trees of reconstructed neuron morphologies. Using parameter values from experimental studies in the literature, we show that the tradeoffs presented in the previous chapter still apply, and that the performance of synaptic scaling is heavily constrained by morphology.

5.1 Robustness and morphologies

5.1.1 Simplified morphologies through transfer functions

Predicting the behavior of a large dimensional system can be nontrivial and computationally expensive, especially with nonlinearities. Neuronal systems fall under this category, and attempts to build reduced order models of neurons started with Rall's in his equivalent cylinder

a. granule cell   b. Purkinje cell   c. symmetric L3 pyramidal cell

d. Martinotti cell   e. asymmetric L3 pyramidal cell   f. CA1 interneuron

● soma
━ unpotentiated synapse
━ potentiated synapse   ━━ 300 μm
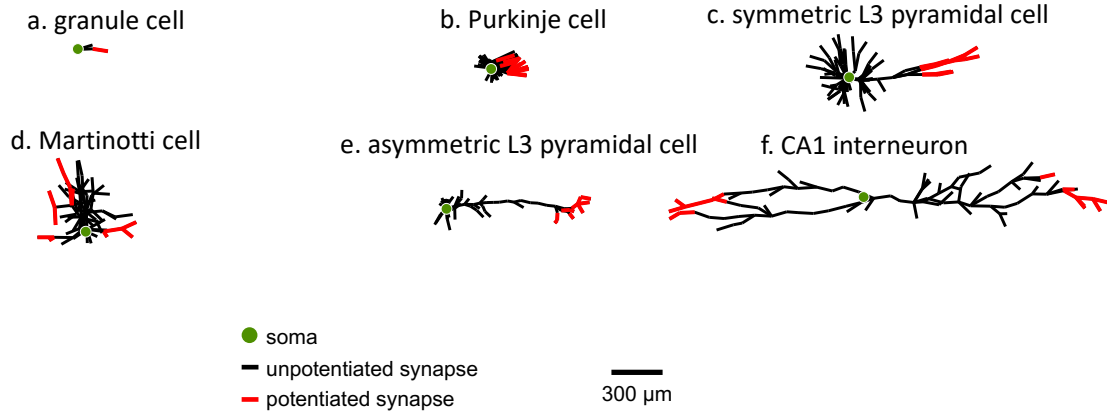
Fig. 5.1 Neuron morphologies considered in this chapter. Green dots correspond to cell body (soma), and red branches correspond to synapses that undergo potentiation. In this chapter, we simulated these morphologies with parameter values in Table 5.1

[126], and other models [98]. These techniques rely on coordinate transformations and on ignoring "disconnected" or "unseen" states (an example of this is the case of Householder transformations [64]).

We take a different approach to address the issue of reduced order models. We start with transfer functions. The use of transfer functions is justified by our interest in the input-output behavior. Specifically, we are interested in how the global and local controllers shape the calcium response to achieve regulation. This implies that, from an input-output perspective, similar morphologies can have different behavior and, conversely, different morphologies can have similar behavior. How can we use transfer functions to cope with morphological complexities?

We start by showing how transfer functions can be used as a *low-cost model for predicting the behavior of the original complex system*. As we have shown before, the return ratio $L(s)$ of the **CLSS** model is a transfer function that correspond to an open loop system. Using the Martinotti cell as a guiding example, we compute its return ratio $L(s)$ and plot a family of Nyquist plots for varying gain k_G, as shown in Figure 5.2a. From this information, how accurate is the prediction if we were to compute the maximum allowable k_G before losing stability? Firstly, we take the furthest and closest curves to -1 (emphasized by blue and red colors), and extract the corresponding k_G values. Next, we use those k_G values to simulate a Martinotti cell. Indeed, the one closest to -1 is nearly unstable (Figure 5.2b), hence agreeing with the prediction we made from the open loop system, which was a transfer function $L(s)$ that corresponded to an SISO system. This is extremely powerful since we avoided

Table 5.1 Model parameters.

	symbol	value	reference
Forward velocity	v_f	$1\ \mu\text{m s}^{-1}$	Ranges in [122, 91, 101]
Backward velocity	v_b	$0.5\ \mu\text{m s}^{-1}$	Ranges in [122, 91, 101]
AMPAR exocytosis	s_i	dynamic	varies with local control
AMPAR endocytosis	s_{-i}	$0.01 - 1\ \text{s}^{-1}$	Lower bound recorded in [77, 78]
Synapse/spine size	c_i	$\{0.5, 1, 2\}$	Ranges recorded in [139]
AMPAR degradation	$\omega_{m,g}$	$4.81 \times 10^{-6}\ \text{s}^{-1}$	[154, 135, 43]
Global set point	$[\text{Ca}^{+2}]_{\text{target}}$	$0.5\ \text{nM}$	Normalized. arbitrary.
Leakage conductance	g_{leak}	$0.5\ \text{pS}$	Arbitrary
Buffering parameters	α, β	1	Chosen to shape sensitivity of $[\text{Ca}^{+2}]$ to V
Equilibrium potential	E_g	$20\ \text{mV}$	Arbitrary
Maximum rate	S_{max}	$10\ \text{s}^{-1}$	Arbitrary
Hill coefficient	h	1	Arbitrary
Dissociation constant	k_A	0.5	Arbitrary
Timescale separation constant	ε	0.1	Has to be $0 < \varepsilon \ll 1$.

simulating the original high-dimensional system, by simply computing the Nyquist curves for multiple k_G values.

This was the case for a Martinotti cell, what about other cell morphologies? Can we extract more information about the real morphology beside predicting how aggressively it can produce AMPARs before losing stability? The answer is yes. To clarify this, we first need to illustrate the effects of morphology on the input-output description. We start by plotting two important quantities. The first one is the *morphological variance* in neurite length, which is computed by measuring the distance from the soma to the dendritic tips (using the TREES toolbox [37])-this represents the *x*-axis. This property captures the symmetry of the morphology. The second property is the *reduction in the number of states*, and it is a ratio that is computed as follows:

$$\text{Percent reduction} = \frac{\text{number of compartments} - \text{number of poles of the transfer function}}{\text{number of compartments}}$$

which will represent the *y*-axis. For a line, the number of compartments is equal to the number of poles. This means that the transfer function of a line embeds in it information about all the compartments. Figure 5.3 shows how this property is correlated to variance which leads to the following observation. From an input-output perspective, feedback for symmetric morphologies causes states to collapse, specifically, identical or sister compartments. The takeaway point is that the degree of symmetry dictates how much *lumping* of identical states takes place in the process of obtaining the transfer function from the real morphology.

(a) Nyquist plots for varying k_G.

(b) $[Ca^{+2}]$ response for two k_G values.
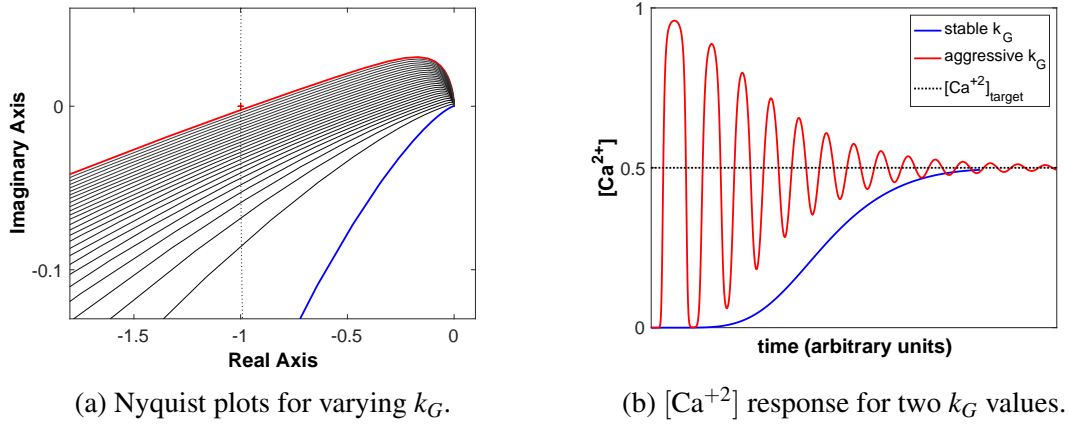
Fig. 5.2 Using transfer functions to predict robustness of Martinotti Cell.
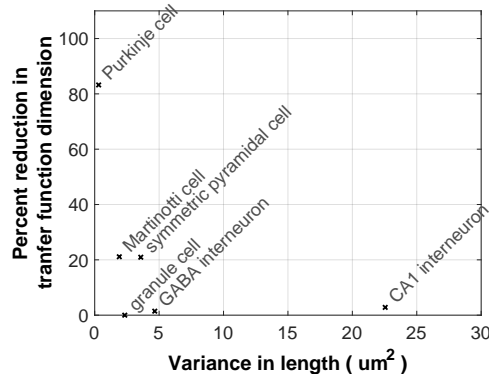
Fig. 5.3 Morphological symmetry, captured by the branches variance, strongly effects the number of poles of the transfer function.

An important characteristic can be extracted from transfer functions, which is based on the fact that they are invariant under coordinate transformations. This means that every morphology can be mapped, via coordinate transformation (for example by Householder transformation [64]), to an equivalent morphology which has the shape of a line. We will call it G_{line}. Equivalent here means that the original morphology and the "equivalent line" will have the same transfer function. Indeed, they are equivalent from a feedback perspective, that is, the closed loop of the original morphology can be replaced by the closed loop of its equivalent line preserving the overall behavior.

To further illustrate this idea. Let's assume that we have a morphology with m compartments and that its transfer function has n poles. Then we can deduce that its equivalent line G_{line} will have n compartments. This provides an indication of the true complexity of a morphology from the perspective of closed loop regulation.

In summary, every morphology is associated with a transfer function and can be mapped to an equivalent line. The features of this equivalent line give us an abstract measure of how hard/simple it is to achieve stability/robustness/accuracy for that specific morphology. In fact, this observation substantiates that the control mechanism reacts to the input-output behavior. As we saw, the behavior of a complex network is not more difficult than a line. In other words, morphologies behave simpler than we think and what dictates the behavior is the parameters of the equivalent line. Those parameters, in turn, reflect the effect of morphology on the regulation problem.
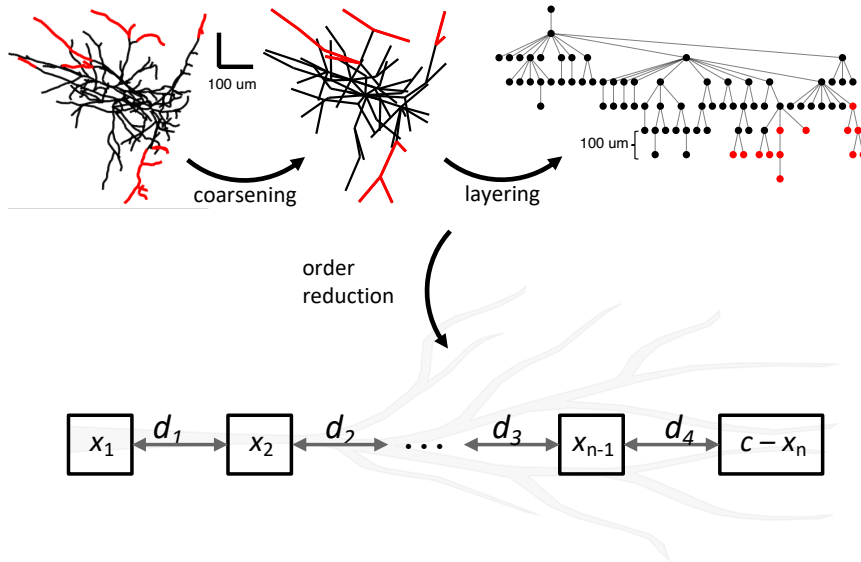
Fig. 5.4 From a real morphology to a reduced-order model.

5.1.2 Input-output description of morphology

Now we take the notion of the equivalent line a step further towards a reduced-order model. If every morphology can be mapped to an equivalent line, it makes sense to search for a simplified/reduced line model that captures, with few compartments, the rough behavior of the system. Unlike equivalent lines, the reduced-order models considered here are equipped with homogeneous parameters. Specifically, we study ball-stick models [5] and how accurate they can capture the behavior of real morphologies.

In the ball-stick model, the complex morphology of the neuron is replaced by a line of compartments with a single synapse placed at the tip, as shown in Figure 5.4(bottom), with

parameters for diffusion d, capacity c, number of compartments n, and degradation ω. Real neuron morphologies vary in size and symmetry, which are expected to impact parameters in their ball-stick representation. For example, a longer neuron like a pyramidal cell would best fit to a longer ball-stick than that of a granule cell.

The fitting to a ball-stick model begins with a raw neuron morphology (Figure 5.4-top). The morphology can be coarsened to some fixed distance (100 µm) between nodes using the TREES toolbox [37], shown in Figure 5.4. The layered depiction clarifies the logical progression of cargo through branches. The coarsened model is simulated, and input u and output g_{avg} are recorded. Ball-stick parameters are estimated using Grey-Box Model Estimation from the MATLAB system Identification Toolbox. Grey-Box Model Estimation uses the structure of the nonlinear ball-stick model with fixed n for fitting to input and output vectors.

System identification is performed to demonstrate that a ball-stick model alone can capture the dynamics of a real neuron morphology. Figure 5.5 shows that the estimated parameters are converging as n increases. Subsequently, the ball-stick fit improves. Furthermore, we perform another set of simulations where we fix the number of compartments at 4, and map the different morphologies to study how much such a low-dimensional reduced-order model can capture the dynamics of morphologies. We found that the $4-$dimensional system gives an accuracy of fitting the input-output behavior between 69-96% for the different morphologies as shown in Table 5.2.

The main conclusions of this section are twofold. Firstly, due to the control mechanism and by virtue of feedback, the input-output behavior of the regulation problem over a morphology is *analogous to that of a line, and what matters is the parameters on that line*. This is remarkable since the reduction of complexity is considerable, both for analysis and computation. Secondly, this means that the observations and the trade-offs discussed in previous chapters will hold for real morphologies. This will be discussed in detail in the next section.

5.2   Neuron size and symmetry impact scaling performance

We have demonstrated how the neuron morphology is fundamentally captured by its transfer function, equivalent line, and its ball-stick representation. Other scaling attributes, efficiency and accuracy, are also affected by neuron morphology. In this section, we continue to examine how real morphology shapes scaling performance, by looking at several dendritic arbors, as shown in Figure 5.1, using parameter values that agree with those experimentally reported in the literature (Table 5.1).
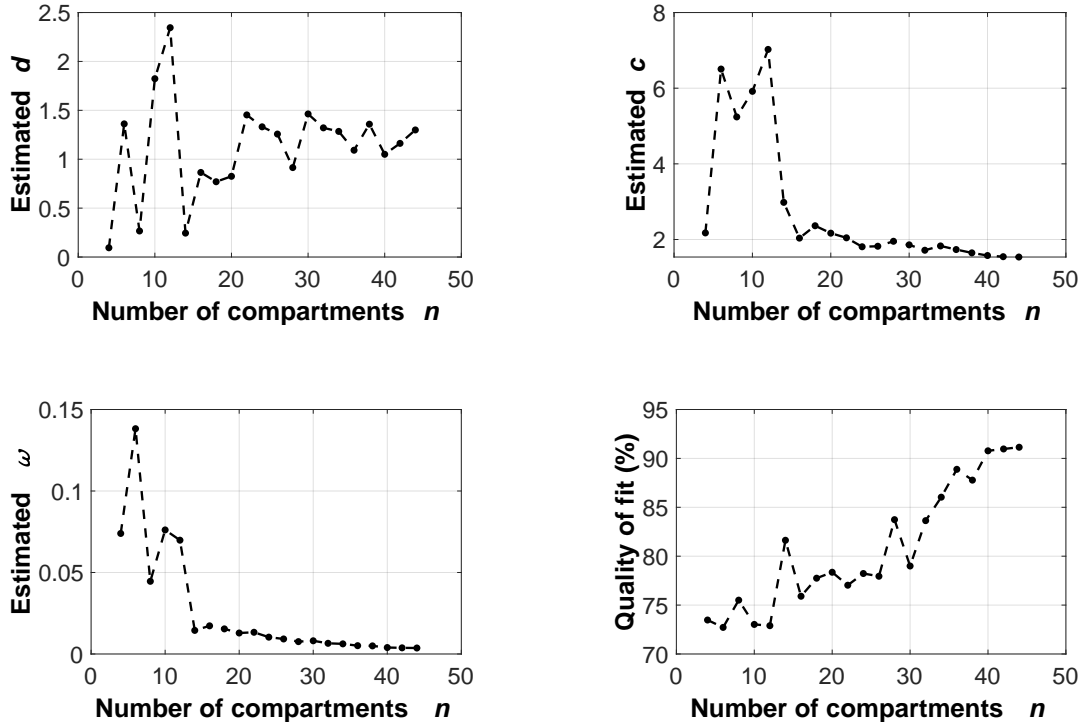
Fig. 5.5 Parameters fitting and quality of fit.

5.2.1   Settling time and scaling accuracy in real morphologies

We first examine scaling performance across the spatial dimension. The progression of AMPARs distribution over time is depicted in Figure 5.6(left). Granule cells have small morphologies and settle within 1 hour (column a). Martinotti and Purkinje cells are larger and fairly symmetric and settle within 5 hours (columns b and d, respectively). The CA1 interneuron and pyramidal cells require up to 15 hours for complete synaptic scaling (columns c, e, and f respectively). Larger cells need more time to get AMPARs to all the compartments, including the distal ones.

The scaling error for individual synaptic compartments (q, see Equation (4.2)) is depicted over each morphology in Figure 5.6(right). Regions of poor accuracy have high AMPAR demand or low cargo supply. This includes regions far from the AMPAR source (soma) and adjacent to potentiated synapses, evident in the pyramidal cells (c and e). High densities of bifurcations also increase scaling error, evident in the CA1 interneuron (f). Bottleneck effects [161] might also play a role in limiting AMPAR supply (e and f).

In Figure 5.7, k_G was tuned such that each morphology has a similar stability margin for a fair comparison of scaling efficiency and accuracy. All morphologies have a stability margin in the range $[0.2791, 0.344]$. Smaller neurons scale synapses with better performance.

Table 5.2 Ball-stick model parameters fits for various neuron morphologies constrained to $n = 4$

	Estimated parameters			Quality of fit
Cell type	**diffusion d**	**capacity c**	**degradation w**	**% fit**
CA1 interneuron	1.072	0.80	0.1062	93
granule cell	0.084	0.93	0.0002	82
L3 pyramidal, asymmetric	2.134	0.99	0.0781	78
L3 pyramidal, symmetric	0.100	1.11	0.0651	87
Martinotti cell	0.040	3.03	0.0593	96
Purkinje cell	0.029	14.52	0.0672	69
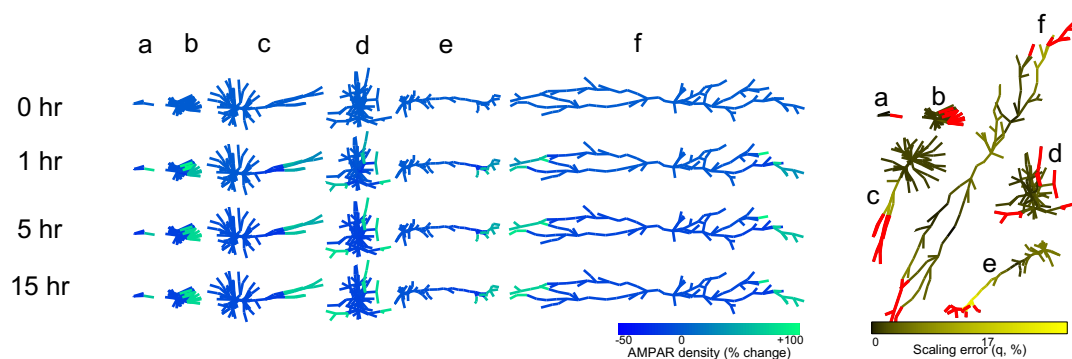
Fig. 5.6 Synaptic scaling settles throughout each morphology at four time points (left) and Scaling error at steady state following LTP reveals increased error in distal compartments (right).

The settling times for all neurons vary significantly, with the granule cell reaching 98 % steady-state in under 5.5 hours, while large neurons like the CA1 interneuron require 141 hours.

The observations in this section agrees with those made with toy neuron models in the previous chapter: less branched and smaller morphologies perform significantly better. This is specifically related to the line vs star study in Figure 4.10. Considering the line and star topologies to be the two extreme cases of symmetry, morphologies lie in between these two cases. However, effective length and the size of the morphology plays an important role. Therefore, beside variance, which reflects the symmetry of the morphology, we study the effects of mean/effective length on the neuron's performance in the next section.
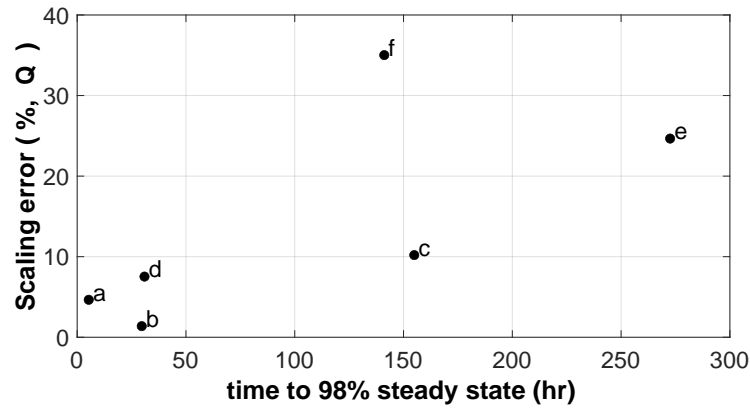
Fig. 5.7 Smaller, more symmetric morphologies have better scaling performance.
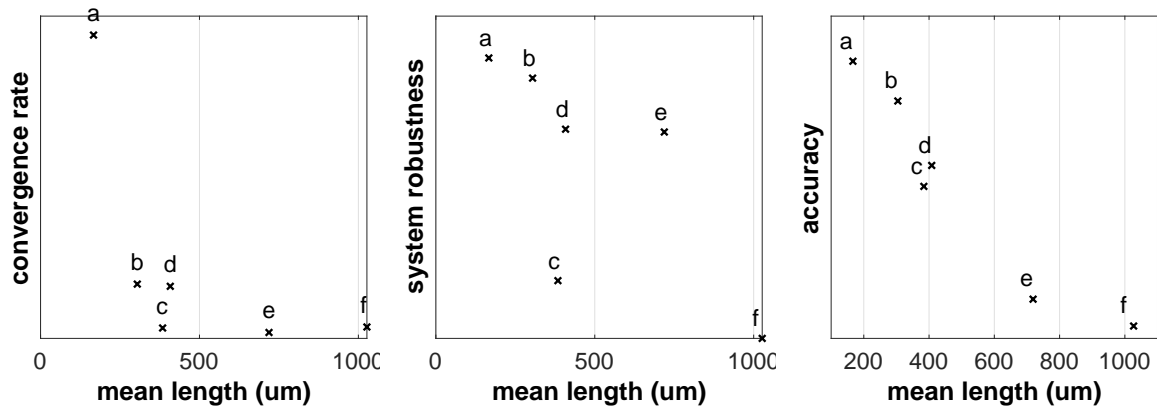
Fig. 5.8 Comparing the scaling performance of the neurons' different morphologies against their mean length.

5.2.2 Morphology effect on the three attributes of performance

Here we consolidate measures of neuron morphology to predict scaling performance. For each morphology, we average all soma-tip path lengths to estimate an effective neural mean length. In Figure 5.8, metrics of scaling performance are plotted against mean length. In general, cells with low mean lengths have improved scaling performance. Neurons with the highest mean length (the CA1 interneuron and asymmetric L3 pyramidal cell) have the slowest convergence rate, accuracy, and robustness. In connection with the toy neuron models, shorter cells are more robust longer ones (Figure 4.5b); this pattern is preserved in real morphologies.

The variance in soma-tip lengths also correlates with scaling attributes, as shown in Figure 5.9. In connection with the toy neuron models, more symmetric cells scale much better than asymmetric ones (Figure 4.11); this pattern is also preserved in real morphologies.
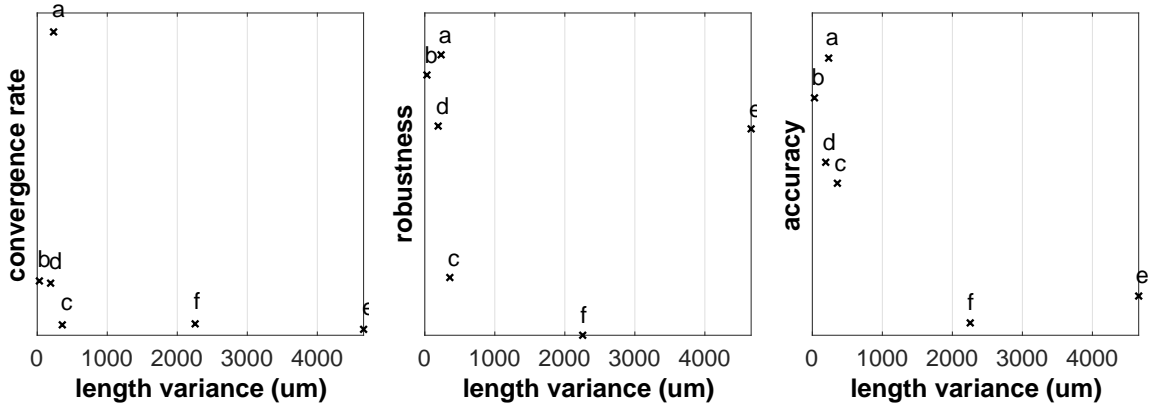
Fig. 5.9 Comparing the scaling performance of the neurons' different morphologies against their variance.

Neurons with large and extended branching patterns are harder to regulate than shorter and less branched ones. The explanation becomes intuitive when we use the ball-stick approximation in place of morphologies. A shorter ball-stick model is always easier to control and regulate, as morphology effects are minimized in this case. These observations lead us to believe that the tradeoffs we obtained using toy neurons models 4.13 are indeed still applicable in real morphologies.

5.2.3 Regeneration of the tradeoffs in a Martinotti cell

We lastly try to regenerate the $2-D$ tradeoffs, presented in Figure 4.13, but now for a real neuron morphology. We perform such simulations for more simple (Martinotti) and complex (pyramidal) neurons in Figure 5.10. We perform the simulations with varying k_G, k_L, and s_{-i}. In all three tradeoffs, the more complex (asymmetric) neuron—the pyramidal cell—has worse scaling performance.

As expected, real morphologies replicate the tradeoffs observed in the previous chapter. Indeed, neurons appear to have optimized their performance with respect to the three attributes. Given the current model, the neuron cannot improve one attribute unless one or the other two are worsen. The only apparent way performance can be improved is if neuron undergo morphological or structural changes. This indeed is a physiologically possible option that we explore in Chapter 8.

5.3 Chapter summary and concluding remarks

This chapter can be summarized in the following key points:
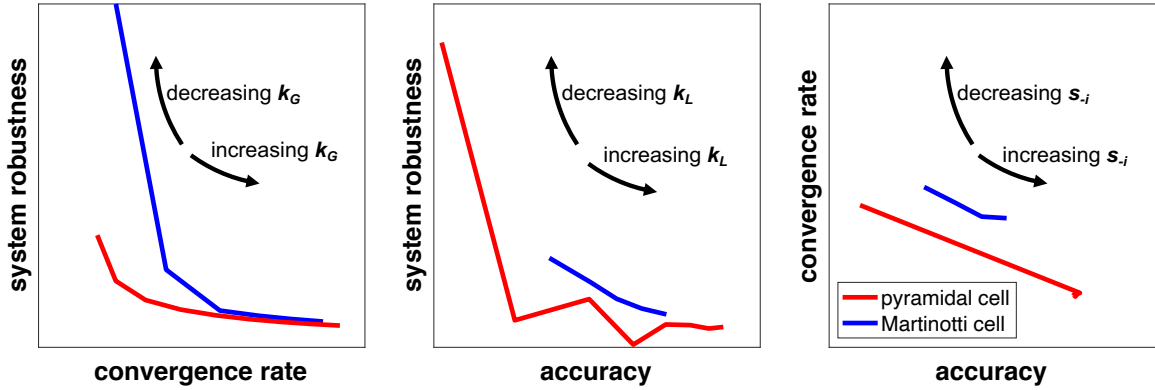
Fig. 5.10 Martinotti and Pyramidal cells navigate the tradeoff between scaling attributes.

1. The performance of the regulation mechanism is determined by the input-output behavior of the dendritic tree. Therefore, the reduction to approximate models where the morphology is reduced to a line, like the simplified ball-stick model, is justifiable.

2. Specific features of the neuron morphology severely limit the performances. For example, length and variance of the morphology enforce hard constraints on the overall performance.

We have shown how different dendritic morphologies perform differently, by showing that synaptic scaling in short and less branching networks is more robust, efficient, and accurate than longer and elaborate ones. These observations were guided by the fact that, to the cell body, the complex dendritic tree is equivalent to a simple line. Therefore, from the next chapter onwards, we consider simple toy neuron models, such as lines and binary trees, at the expense of more complex models. This will allow us to clarify other important properties and tradeoffs at the cost of geometrical details on the morphology. Nonetheless, this sacrifice is of a limited cost, as we have shown in this chapter.

We have established that scaling performance largely depends on neuron morphology. We have also shown that high demand for AMPARs (increasing c_i) results in imperfect synaptic potentiation and scaling. Indeed, experiments and computational studies have demonstrated that synapses compete among themselves for resources [132, 148]. Synaptic competition results from the neuron's homeostatic set point $[\text{Ca}^{+2}]_{\text{target}}$, which sets a constraint on the number of allowable AMPARs $\sum g_i$. $\sum g_i$ remains unchanged despite an increase in c_i during LTP, which results in imperfect scaling. As discussed earlier, this is explained by the fact that proximal synapses scale better, since they have earlier access to a larger pool of AMPARs.

Up to this point, we have only considered transport of m, but not g. An example of g transport is the lateral diffusion of AMPARs, or "cross-talk" between synapses [46].

Incorporating such lateral diffusion changes the g dynamics [1] to

$$\dot{g}_i = s_i m_i (c_i - g_i) - s_{-i} g_i - \omega_i^g g_i + dg_{i-1} - 2dg_i + dg_{i+1}. \tag{5.1}$$

where d is a diffusion coefficient. Lateral diffusion appears to normalize the steady-state distribution of g, and therefore improving accuracy. However, experimental measures of diffusion rates between synapses—and therefore across dendritic spine necks—are significantly lower than active microtubule-based transport rates v_f and v_b [51]. This limits g normalization, which suggests that the impact of lateral diffusion on scaling performance is negligible, hence the tradeoffs are not heavily altered, and hence maintained.

Using transfer functions and Nyquist stability criterion, we analyzed the robustness of the **CLSS** model, as shown in Figure 4.5b. In agreement with Hebbian-form of plasticity, we saw that increasing c_i indeed contributes to the reduction of the system's robustness, and therefore destabilizing it. This is reminisent of persistent LTP that ultimately leads to excitotoxicity. However, if we consider toy neuron models similar to that in Figure 4.10(left), then varying c_i can have a different effect. By different we mean that potentiating a proximal synapse versus a distal one does not exhibit the same influence- in the sense of robustness of the model and its stability margins.

The discrepancy between proximal and distal LTP can be understood in the context of phase lag. LTP of proximal synapses increases cargo demand close to the soma, which is easily achieved with little time delay. LTP in the distal synapses imposes a demand for cargo that is more difficult to globally regulate, given the increased phase lag. LTP in proximal synapses shifts the mean distance of all cargo closer to the soma, which alleviates the destabilizing effect. LTP in the distal synapses shifts the mean distance of all cargo further, which increases phase lag and intensifies the destabilizing effect. This behavior can be clarified using the aforementioned ball-stick model [5]. As mentioned before, the ball-stick model is an abstract approximation of a dendritic tree in which all synapses are lumped into a single compartment at the tip, and the length of the stick reflects the effective length of the dendritic tree. In this setting, distal LTP results in a ball-stick approximation with larger effective length than that of a proximal LTP.

In the following chapters, we take advantage of the results of section 5.1 and focus on simple toy neuron models, mainly models of lines and binary trees. We will study variations of the **CLSS** model to focus on specific aspects of the phenomena of homeostatic regulation of average neuron activity. In the next chapter, for example, we study the effects of activity-dependent degradation.

---

[1]This does not effect the proof of Theorem 3. See proof remarks.

Chapter 6

Synaptic scaling in the presence of activity-dependent degradation: a local-global tale

> *"Think globally, act locally"*

> Unknown

In this chapter we study the effects of activity-dependent regulation on synaptic scaling. Specifically, we analyze the role of activity-dependent degradation ω_m and its effects on performance and stability.

6.1   Introduction and motivation

The **CLSS** model is most sensitive to variations in the degradation rate ω_m, as evident from the robustness study in Figure 4.5b. Intuitively, this is understood since degradation "dissipates" mass from the system and prevents it from accumulating. We made a simplifying assumption by setting degradation to occur at a constant rate. Here, we further explore the implication of activity-dependent degradation on the performance of the neuron and scaling.

Neurotransmitter receptors and ion channels are dispersed throughout the dendrites of postsynaptic neurons. They are transported from the cell body all the way to extremities of the dendritic tree. They are next inserted into synaptic sites according to inputs, activity, and location in the network. An important feature of synaptic plasticity is a persistent and long-term change in the synapse undergoing activity. Such changes necessarily require an activity-dependent protein turnover rate.

Experimental data suggest two broad classes of activity-dependent feedback mechanisms in neurons: global and local feedback. Global feedback regulates the synthesis of material at the cell body, necessarily including all mRNA synthesis. Local feedback regulates the synthesis and delivery of proteins in the vicinity of the site of use, throughout the dendritic tree [55, 60, 56]. The role of both mechanisms in maintaining neuronal function is the subject of intense experimental research and debate, and is believed to vary substantially across biological contexts, including animal species, brain area and neuron type. Nonetheless, these mechanisms serve two broad goals:

  (i) maintaining average electrical activity at an (approximate) set point;

 (ii) supporting heterogeneous distribution of receptors and ion channels across the dendritic tree.

In the previous chapter, specifically in the **CLSS** model, (i) and (ii) were achieved by (3.4) and (3.8), respectively. In Equation (3.4), cargo synthesis rate was set to be dependent on the mismatch between the global set-point and average neuron activity; in this way, cargo synthesis is regulated in order to achieve homeostasis, and global synaptic scaling was the emergent phenomena. Equation (3.8) was a local adaptive activation mechanism that regulated the insertion of active cargo into synaptic sites, with the goal of preventing Hebbian-like instabilities. In this chapter we continue our study of local activity-dependent mechanisms by exploring other biologically relevant processes, focusing on the role of activity-dependent degradation.

6.2   A modified synaptic scaling model

To study activity-dependent degradation, we consider a variant of the **CLSS** model.

A simplified sketch of a neuron is shown in Figure 1. As we did in Chapter 3, we model the neuron as an interconnection of n compartments. The first represents the soma (or cell body), while the remaining compartments refer to sections of the dendritic tree. Using m_i to denote the concentration of material in compartment i, the variation in time of m_i is described by

$$\dot{m}_i = -\left(\omega_i^m + \sum_{i=1,i\neq j}^{n} v_{ij}\right)m_i + \sum_{j=1,j\neq i}^{n} v_{ji}m_j + b_i u$$

where $v_{ij} \geq 0$ is the trafficking rate or speed of material moving from compartment i to compartment j, and $\omega_i^m > 0$ is the degeneration rate of m_i. We assume $v_{ij} = 0$ if and only if
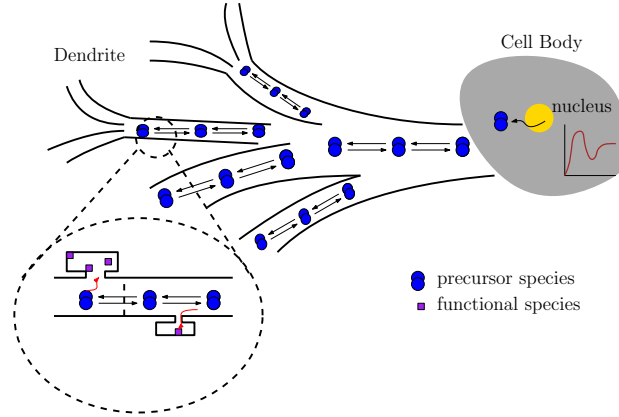
Fig. 6.1 Schematic of a neuron showing its structure and sites where processes of interest occur, from the cell body to the extremities of the dendritic tree.

i is not connected to j. The input u represents m_i synthesis or production. We assume that material production occurs primarily in the cell body, where the required machinery exists, including nucleic acids and ribosomes. Overall, the dynamics is represented by

$$\dot{m} = (L - \Omega_m)m + Bu \tag{6.1}$$

where $m \in \mathbb{R}^n$, $L \in \mathbb{R}^{n \times n}$, and $\Omega_m = \text{diag}\{\omega_i^m\}$. The off-diagonal elements of L satisfy $l_{ij} = v_{ji}$. The diagonal elements of L satisfy $l_{ii} = -\sum_{j=1, j \neq i} v_{ij}$.

(6.1) is a drift-diffusion system modeling active intracellular transport, performed by motor proteins [161, 5]. To allow the material to reach every point in the dendrite, we assume that there is alway a path from the first compartment to any other compartment. We also assume bidirectionality, that is, if if $l_{ij} \neq 0$ then $l_{ji} \neq 0$.

Similar to the **CLSS** model in Chapters 3-5, species g is a functional cargo that modulates the electrical activity of the neuron. In other words, m is produced in the soma, while a reaction occurs $m_i \rightarrow g_i$ in synaptic sites. This reaction takes place according to the rule $\dot{g}_i = s_i m_i - \omega_i^g g_i$ where s_i is the transformation factor from m_i to g_i and ω_i^g is the degradation rate of g_i. In matrix form,

$$\dot{g} = Sm - \Omega_g g \tag{6.2}$$

where $g \in \mathbb{R}^n$, $S = \text{diag}\{s_i\}$, $\Omega_g = \text{diag}\{\omega_i^g\}$, and $S, \Omega_g \in \mathbb{R}^{n \times n}$. In the **CLSS** model in Chapters 3-5 m and g were AMPARs and the only difference was their location in the dendritic network; m_i was an inactive dendritic cargo, while g_i was an active synaptic cargo. Furthermore, the reaction (6.2) was bidirectional/reversible ($s_{-i} \neq 0$). In this chapter, however, the interpretation of species m and g is slightly different, and more general in

certain aspects. Firstly, *m* here is interpreted as precursor species and *g* is a functional species that is obtained after *m* undergoes a number of reactions. An example of this situation is when equation (6.2) models translation or protein synthesis. In this situation, *m* is a mRNA-type cargo, where *g* is the protein or ion channel needed to modulate neurons activity. Therefore, we replace the activation and inactivation rates from the previous chapters with a transformation factor s_i.

The first-order dynamics (6.2) implies that the reaction $m_i \rightarrow g_i$ is not happening instantaneously, but rather takes time. Furthermore, from equation (6.1), the new synaptic molecule is not inserted back to the dendritic arbor, and hence is not transported. This biological setting is maintained in the following chapters. Moreover, equation (6.2) adds a theoretical simplification to the model, since the dynamical activation rate $s_i(t)(c_i - g_i)$ was replaced with z constant rate s_i. As we laid out in the introduction of this chapter, the local control will be implemented in the degradation process, in a fashion that will be revealed shortly. As a result, we will model LTP events differently; instead of instantaneously changing the capacity/number of slots c_i, we will do this through assigning local set-points to compartments.
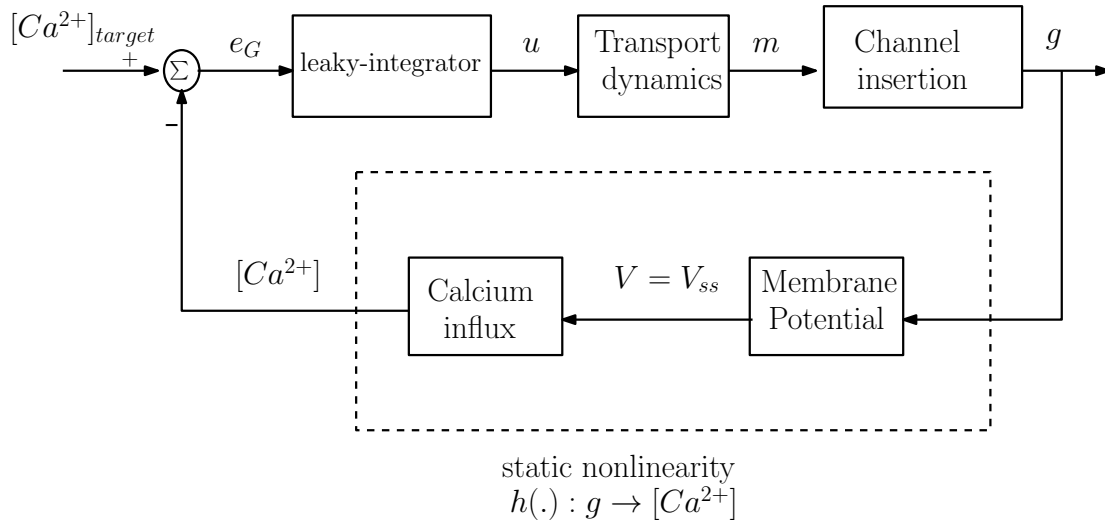
Fig. 6.2 Block diagram of the closed loop system (6.1)-(6.7).

The processes that describe the generation of the feedback signal from functional cargo *g*, i.e. $h(.) : g \rightarrow [Ca^{2+}]$, to the homeostatic cargo synthesis *u* is unchanged from the previous

chapters. Nonetheless, we state the system of equations for readability.

$$\text{Readout map:} \quad g_{avg} = \frac{\mathbf{1}^T g}{n} = \frac{\Sigma g_i}{n} \tag{6.3}$$

$$\text{Membrane potential:} \quad V := V_{ss} = \frac{g_{avg}E_g + g_{leak}E_{leak}}{g_{leak} + g_{avg}}. \tag{6.4}$$

$$\text{Calcium signal:} \quad [\text{Ca}^{2+}] = \frac{\alpha}{1 + \exp(-V/\beta)} \tag{6.5}$$

$$\text{Error:} \quad e_G = [\text{Ca}^{2+}]_{\text{target}} - [\text{Ca}^{2+}] \tag{6.6}$$

$$\text{Global controller:} \quad \dot{u} = k_G e_G - \omega_u u \tag{6.7}$$

Equations (6.3)-(6.7) matched equations (3.4)-(3.6) in the **CLSS** model. In Figure 6.2, we show the block diagram describing the interconnection between the different dynamics and relations. Theorem 4 below is similar to Theorem 3 after implementing the modifications we presented above. These modifications include replacing the adaptive activation and inactivation terms with a single transformation factor, and implementing the local irreversible reaction that transform trafficked m_i into functional cargo g_i.

Theorem 4 *Under Assumption 1, for any selection of system parameters, there exists a feedback gain $\bar{k}_G > 0$ such that the equilibrium of the closed loop model* (6.1)-(6.7) *is globally exponentially stable for any $0 < k_G \leq \bar{k}_G$.*

6.3   Limitation of the homeostatic controller

In agreement with the **CLSS** model in the previous chapters, the closed loop system (6.1)-(6.7) achieves stable regulation. The modified closed loop system exhibits the same tradeoff between convergence rate and robustness; this is illustrated via simulations, based on topology and parameters in Figure 6.3. For increasing values of k_G, the simulations in Figure 6.4 reveal that the system is well-behaved and achieves regulation for small values of k_G. Convergence improves for larger values of the feedback gain. Eventually, however, high values of feedback gain lead to instability (oscillations).

This fundamental limitation can be explained in a similar way to the previous chapters. It follows from the particular form of the Nyquist diagram of the linearized system, which shows a Nyquist locus similar to the one in Figure 4.1a. As a result, the gain margin of the system is finite, that is, above a certain gain the system becomes unstable. The relationship between increasing k_G and the emergence of oscillations is attributed to the interconnection nature of the dynamics (6.1)-(6.7), as portrayed in Figure 6.2. The return ratio of the block

$v_{ij} = 1\ \mu m s^{-1}$ if $i < j$	$v_{ij} = 0.5\ \mu m s^{-1}$ if $i > j$	$\omega_i^m = \omega_i^g = 0.1\ s^{-1}$	$g_{leak} = 0.25\ \mu S$
$E_{leak} = -50\ mV$	$E_g = 20\ mV$	$\alpha = 1$	$[Ca^{2+}]_{\text{target}} = 0.5\ \mu M$
$\beta = 1$	$\omega_u = 0.0001\ s^{-1}$	$k_G = \text{varies}$	$s_i = 1\ s^{-1}$
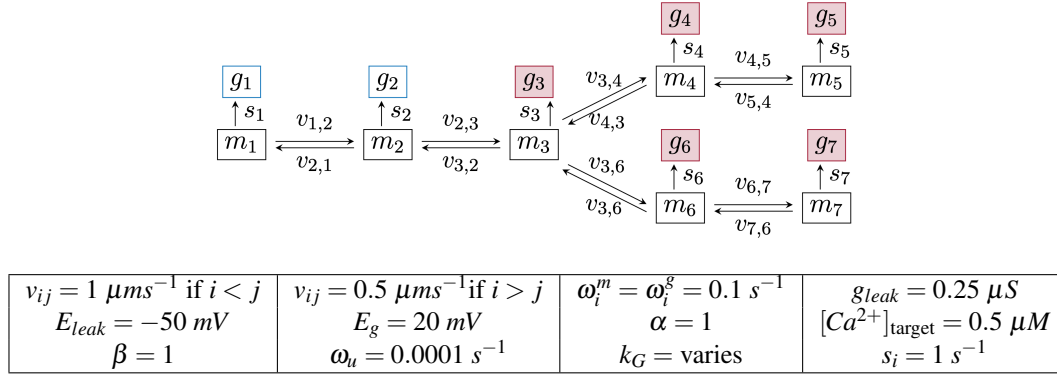
Fig. 6.3 Neuron topology and parameters.

(a) $k_G = 0.003$ (b) $k_G = 0.03$ (c) $k_G = 0.3$

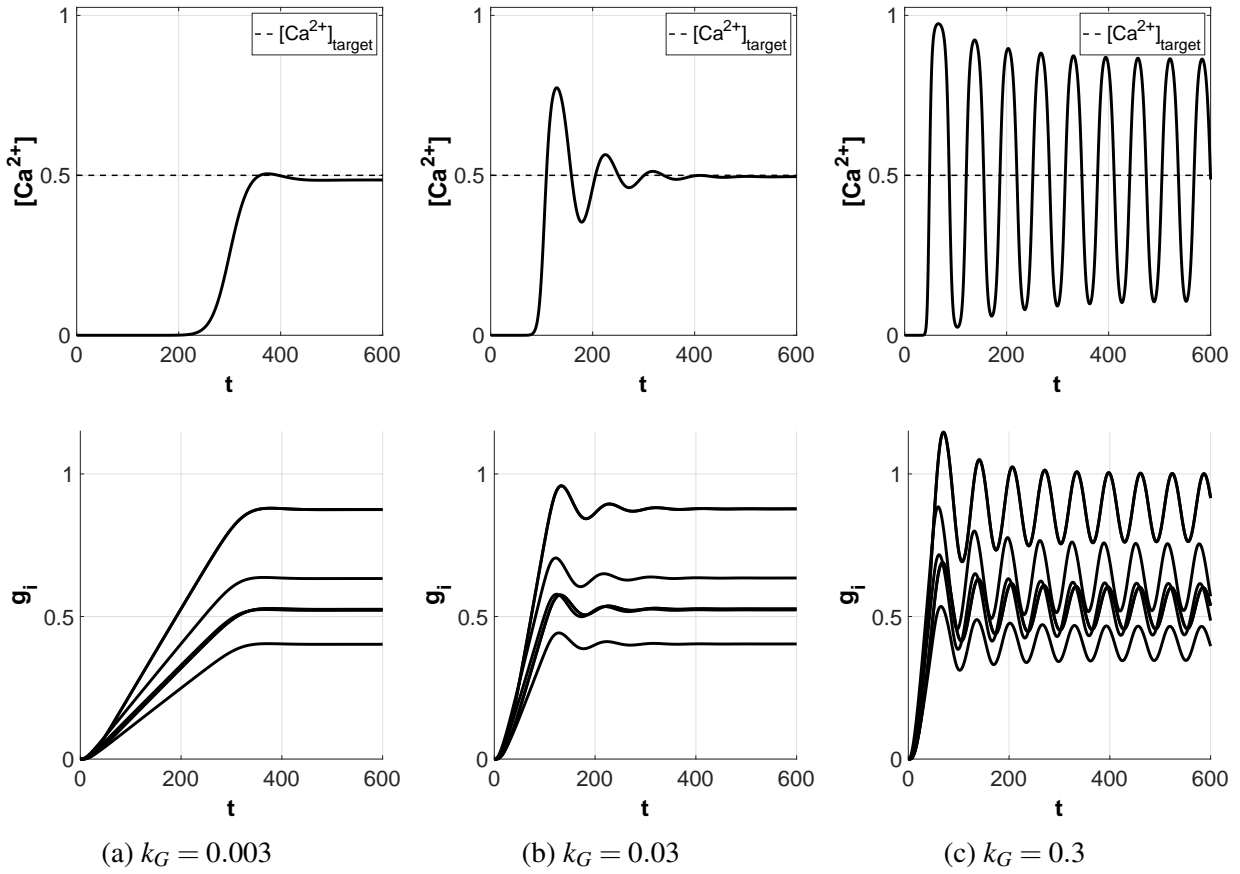Fig. 6.4 Response of closed loop system (6.1)-(6.7) applied to the neuron in Figure 6.3. Increasing feedback gain k_G destabilizes the system. Top panel shows $[Ca^{2+}]$ response, and bottom panel shows g_i response.

diagram has at least a relative degree 3, which has finite gain and phase margins. Increasing k_G gradually decreases those stability margins until the closed loop system is fully unstable.

It is important to emphasize that the relative degree of return ratio is also related to the structure of the readout (6.3) map. The average represents the best case scenario from a performance perspective. Alternatively if the functional cargo g_i were scattered throughout the network in a nonuniform manner (for example, if we set the reaction $m_i \rightarrow g_i$ to occur only in even compartments), then the resulting return ratio would have relative degree > 3, and hence higher sensitivity to variations in k_G.

The global controller guarantees stable average electrical activity of the neuron and scaling is still a prominent feature of the model. In the following section we seek a local control mechanism that achieves two objectives. Firstly, the local control mechanism should improve the tradeoff between convergence rate and robustness, which is mediated by k_G. Secondly, it should shape the overall distribution of ion channels g_i in the dendritic tree. The first goal was alluded to in the robustness study in Section 4.2.1, as illustrated in Figure 4.5b. The second goal is similar to local action in (3.8). The second objective, therefore, serves the neuron's need to support changes to the distribution of receptors and ion channels that are imposed by other processes, while gradually normalizing activity to a target level [36, 151].

6.4   Distributed adaptation

Taking inspiration from [55, 60, 56], we propose a distributed adaptation mechanism to enable fine tuning of ion-channel concentrations, based on adaptation of the degradation rates ω_i^m in feedback from the local concentrations g_i. The adaptation penalizes the mismatch from a desired target while maintaining (physiological) positive degradation rates. The mechanism is defined by the following basic model

$$
\begin{aligned}
i \in \mathbb{I}: \quad & \varepsilon \dot{\omega}_i^m = -\gamma_L \omega_i^m + k_L(g_i - \bar{g}_i) + \phi_{\ell b}(\omega_i, \bar{\phi}) \\
i \notin \mathbb{I}: \quad & \omega_i^m = \omega_i^m(0)
\end{aligned}
\tag{6.8}
$$

where $\mathbb{I}$ is an index set identifying the compartments with active adaptation, $\gamma_L > 0$, $k_L > 0$, and $\varepsilon > 0$ are generic filtering parameters; $\bar{g}_i$ is the desired ion-concentration set point, and $\phi_{\ell b}(\cdot, \bar{\phi})$ is a decreasing barrier function, with domain $(\bar{\phi}, \infty)$, $\bar{\phi} > 0$, whose role is to guarantee that the adaptation of ω_i never goes below the boundary $\bar{\phi}$. $\phi_{\ell b}(\omega_i, \bar{\phi})$ should not affect the dynamics away from the boundary $\bar{\phi}$, as clarified by the next assumption.

Standing Assumption. For any given $0 < \varepsilon_{\bar{\phi}} \ll 1$, we assume that the barrier function $\phi_{\ell b}(\cdot, \bar{\phi})$ satisfies $\phi_{\ell b}(\omega_i, \bar{\phi}) \simeq 0$ and $\frac{d}{d\omega_i}\phi_{\ell b}(\omega_i, \bar{\phi}) \simeq 0$ for all $\omega_i \geq \bar{\phi} + \varepsilon_{\bar{\phi}}$.

The time constant ε is typically small, to reflect the fact that the adaptation of ω_i^m occurs at a faster timescale than (6.1)-(6.7). Standard singular perturbation methods, and specifically Theorem 2, lead to the following result.

Theorem 5 *Under Assumption 1, for any given selection of system parameters, suppose that there exist intervals $0 < k_G \leq \bar{k}_G$ and $0 < \varepsilon \leq \bar{\varepsilon}$ for which the equilibrium $(m^*, g^*, u^*, \omega^*)$ of the closed loop system (6.1)-(6.8) satisfy $\omega_i^* \geq \bar{\phi} + \varepsilon_{\bar{\phi}}$. Then, for k_G and ε sufficiently small, the closed loop equilibrium is exponentially stable.*

Theorem 5 makes clear that the combination of global controller and distributed adaptation guarantees stability of the equilibrium of the system, which depends on the local concentrations targets, $\bar{g}_i$, and on the calcium target, $[\text{Ca}^{2+}]_{\text{target}}$.

Remark 1 *Degradation is hypothesized to be an activity-dependent phenomena [47], and Equation (6.8) is one way to capture the dependence of precursor cargo degradation on local active cargo concentration. Ideally, a reaction of this kind involves multiple processes and signaling pathways, such as phosphorylation/dephosphorylation events; however, for simplicity, we assume that degradation is directly proportional to active cargo concentration. Alternatively, the dependence on g_i can be replaced by a monotone relation that depends on g_i, like $[Ca^{2+}]_i = f(g_i)$. Doing so would not alter the conclusions of this chapter. Hence, we adapt formulation (6.8) for simplicity.*

Protein turnover depends on the balance between protein synthesis and degradation. In the previous chapters, we investigated the effects of activity-dependent insertion/transformation in equation (3.8). Conversely, in this chapter we explore the other possibility which is to model degradation as an activity-dependent process. The ubiquitin proteasome system (UPS) is a known degradation machinery in proteins [62], and in neurons. Moreover, it is influenced by neuronal activity [48] (and references in [7]). For example, a disruption in the ubiquitin-ligase enzymes (E3), a class of UPS pathways, mediated the concentrations of *Arc* and AMPARs in synapses [69]. Furthermore, postsynaptic glutamate receptors can be ubiquitinated as a way to decrease their concentration in the synapse [26]. In fact, regulated protein degradation in neurons has been identified as a way to modulate synaptic growth, development, transmission, and plasticity [75, 85, 42, 164, 111].

As a matter of illustration, we revisit the simulations in Figure 6.4, to show the effectiveness of the adaptation mechanisms at fine tuning the distribution of ion-channels. Adaptation is applied to compartments $3-7$, with local set points $\bar{g}_i = 0.5$. The response of these compartments is shown by the red traces. Figure 6.5 shows how local set points are recovered

for increasing values of the local gain k_L. Moreover, the local adaptation has a stabilizing effect on the closed loop dynamics, substantially reducing system oscillations for $k_G = 0.03$.

(a) $k_G = 0.03$, $k_L = 1$, $\gamma_L = 1$.

(b) $k_G = 0.03$, $k_L = 20$, $\gamma_L = 1$.
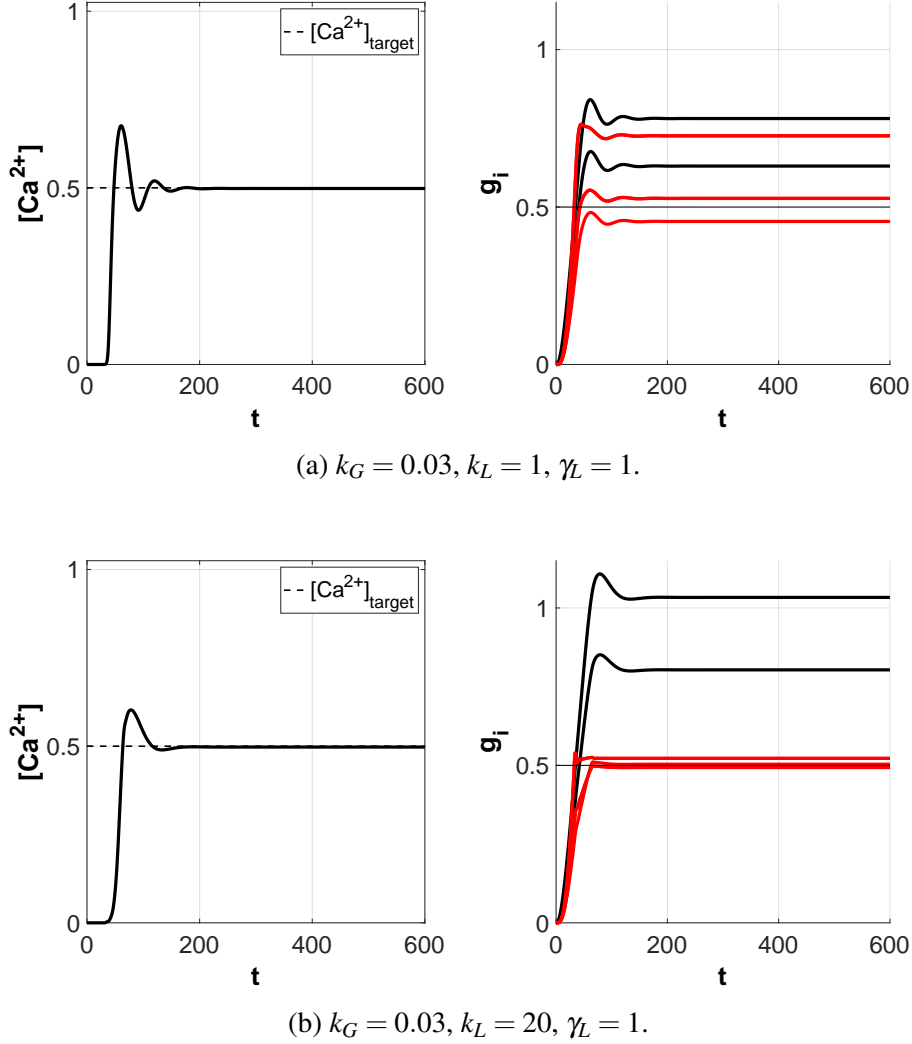
Fig. 6.5 Response of the closed loop model (6.1)-(6.8) for $\bar{g}_i = 0.5$ and $\varepsilon = 0.1$.

The simulations in Figure 6.5 suggest that the two objectives are achieved, namely improving the tradeoff between convergence rate and robustness, and supporting heterogeneous concentration profiles of g. In this way, rapid changes in the efficacy of synapses that are involved in potentiation can occur, while the overall average activity is maintained over longer timescales.

The simulations in Figure 6.6 further illustrate the effectiveness of the local action to cope with a perturbation on the rates s_4 and s_5 occurring at $t = 300$. After a brief transient, the desired set-point is restored.
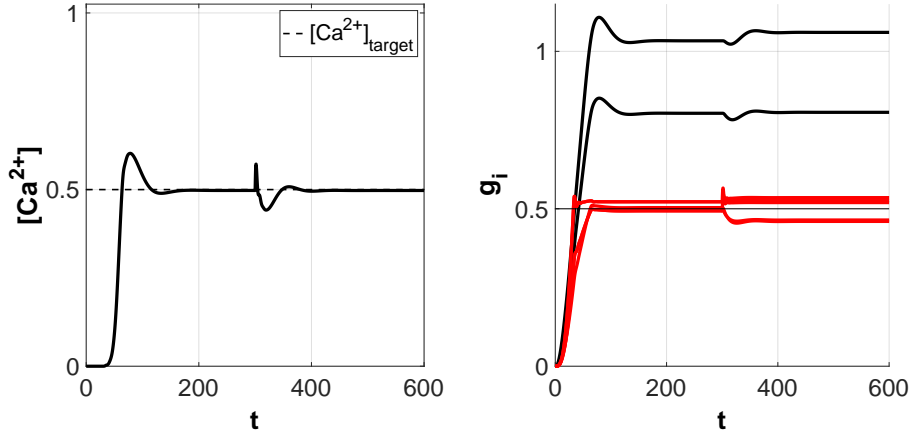
Fig. 6.6 Perturbed response of the closed loop model (6.1)-(6.8) for $k_G = 0.03$, $k_L = 20$, and $\gamma_L = 1$. At $t = 300$, s_4 and s_5 switch from 1 to 2. The system recovers.

6.5   Synaptic plasticity and competition

In Chapters 3-5, we modeled LTP/LTD events by modifying capacities c_i. Here, we will model such events by modifying the local set point $\bar{g}_i$. In both situations, these changes are being introduced exogenously, resulting in a local increase or decrease in the concentration of receptors at the membrane, where communication with other cells can occur.

   In this setting, the global controller (6.7) is still responsible for synaptic scaling, which sets the average number of receptors in the system. On the other hand, the local action sets the local set-point in response to changes like LTP/LTD or Hebbian-like events. In what follows, we show that there might be cases where a competition arises between the global and local objectives.

   Figures 6.7a-6.7b show the system response as $[\text{Ca}^{+2}]_{\text{target}}$ is gradually decreased. Decreasing $[\text{Ca}^{+2}]_{\text{target}}$ corresponds to decreasing the total amount of receptors in the system, hence making it difficult for the local action to succeed in achieving $\bar{g}_i$. When the local action fails to achieve the local set-point, it achieves the closest possible steady state given the limited total mass in the system. The tug-of-war between the global controller and local action can ultimately lead to instability. This is illustrated by gradually increasing the local set point while maintaining a fixed Calcium target, as shown in Figures 6.8a-6.8b.

   The previous simulations imply the extent of the success of the local action in complementing the global controller. Meeting the prescribed objectives depends on three important factors: synapse location with respect to the soma, global set-point, and local set-point. Enough receptors must be present in the neuron (k_G large enough) for the local action to be

(a) $[Ca^{+2}]_{target} = 0.3$

(b) $[Ca^{+2}]_{target} = 0.1$
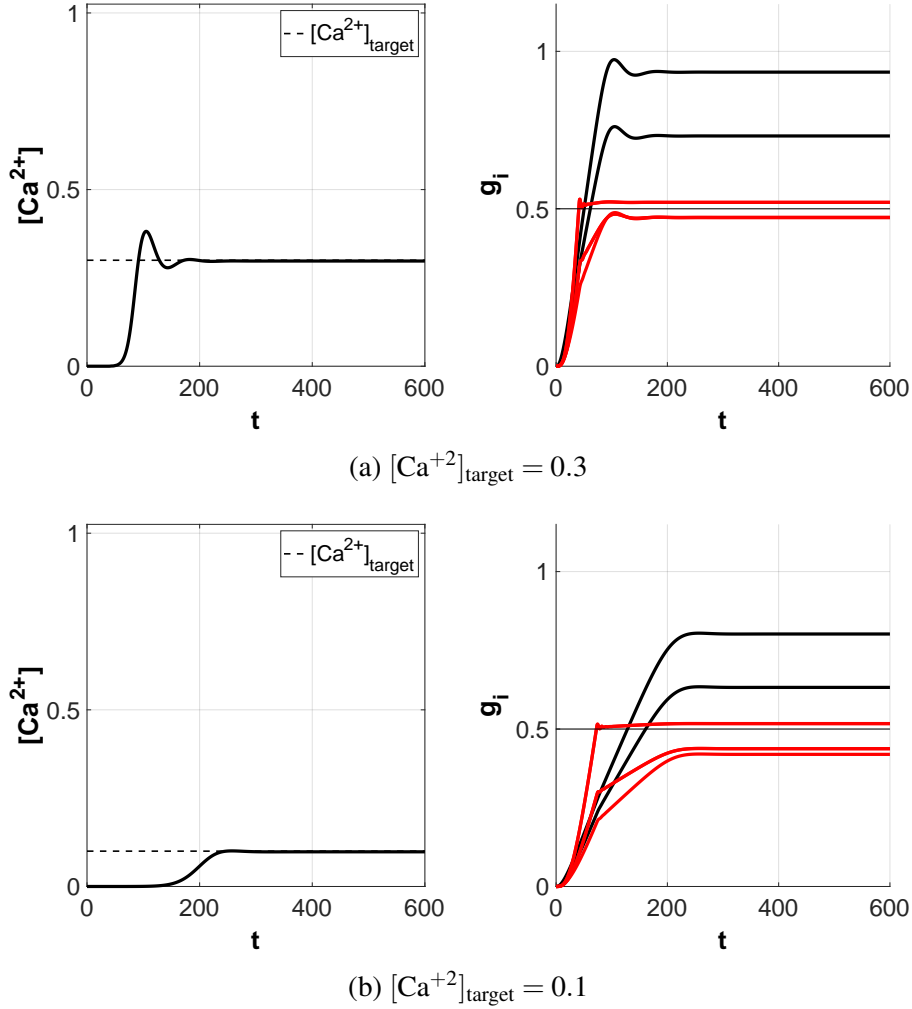
Fig. 6.7 Decreasing the global set point for $k_G = 0.03$, $k_L = 20$, $\gamma_L = 1$.

effective. This is illustrated in Figure 6.5. Indeed, low levels of receptors may force the local action to further deteriorate the neuron's performance, as illustrated in Figure 6.8.

6.6 Chapter summary and concluding remarks

The chapter can be summarized in the following key points:

1. The constraint on the feedback gain $k_G < \bar{k}_G$ follows from the the composition and interconnection of subdynamics of the closed loop system (6.1)-(6.7). The return ratio of the feedback loop $L(s)$ always has a relative degree ≥ 3. This also explains why k_G modulates the tradeoff between convergence rate and robustness.

(a) $\bar{g}_i = 0.8$

(b) $\bar{g}_i = 1.1$
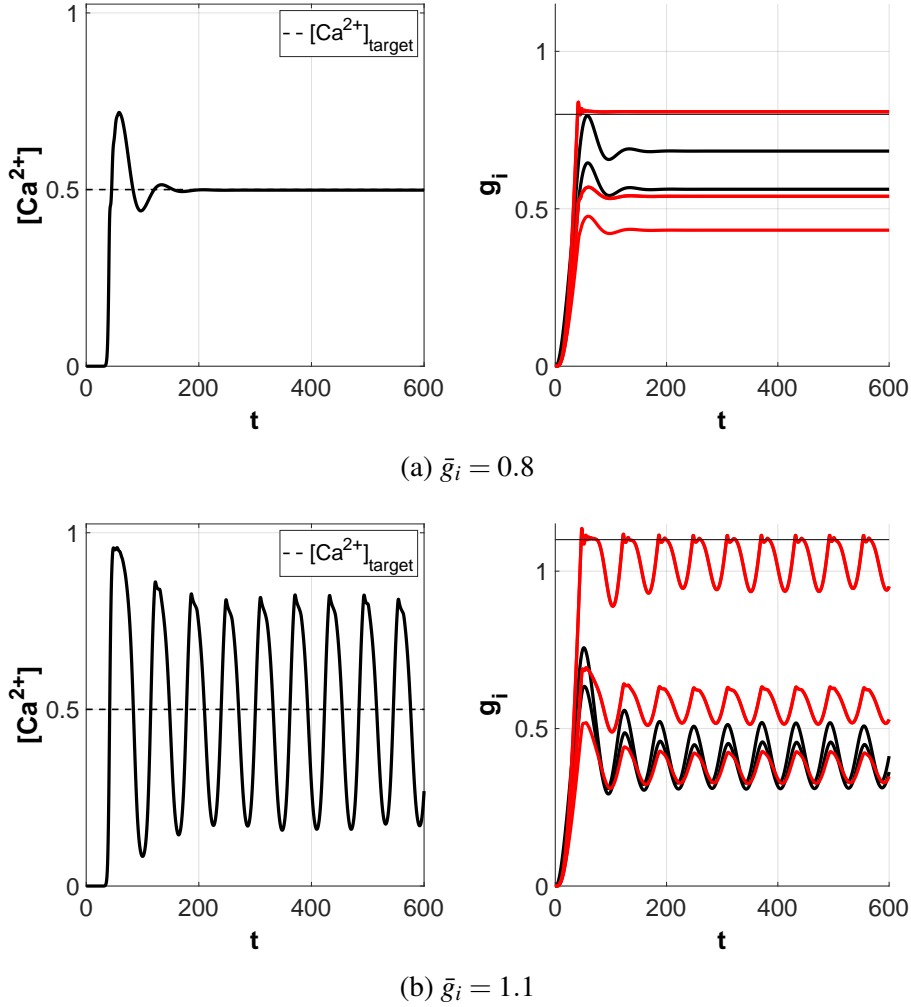
Fig. 6.8 Increasing the local set point for $k_G = 0.03$, $k_L = 20$, $\gamma_L = 1$.

2. Activity-dependent degradation has a bidirectional effect on regulation, depending on synaptic location, the local set-point, and global set-point.

Both local actions in (3.8), and in (6.8) correspond to rapid changes in synaptic efficacies, by setting $\varepsilon \ll 1$. Increasing the local sensitivity k_L in both mechanisms amplifies the effect of the local action, thereby improving the response to local activity in individual synapses. Conversely, in situations of very high local feedback sensitivity k_L, the scheme in (6.8) had a destabilizing effect (Figure 6.8). This was not the case in the **CLSS** model.

In the next chapter, we analyze the effects of another biological limitation, which is the finite capacities of dendritic compartments. Up to this point, we assumed that receptor transport occur linearly and that trafficking rates v_f and v_b are fixed. We will study the effects

of relaxing this assumption on the regulation of average neuronal activity. Moreover, we also investigate the effects of varying the timescale of cargo synthesis.

6.7 Proofs

We start with the proof of Theorem 5. The proof of Theorem 4 is similar, and can be derived from the proof of Theorem 5.

6.7.1 Proof of Theorem 5

Part 1 and Part 2 below satisfy the conditions of Theorem 2 which allows to conclude the exponential stability of the equilibrium of the closed loop system from the analysis of two reduced subsystems, namely the boundary-layer system and the reduced system, both specified below.

Part 1: exponential stability of the boundary-layer system

Define the function $\phi(g_i, \omega_i) = k_L(g_i - \bar{g}_i) + \phi_{\ell b}(\omega_i, \bar{\phi})$. The boundary layer system is obtained by finding the (parameter dependent) equilibrium $\bar{\omega}_i^m(g_i)$ of (6.8), which corresponds to the solution to the equation $\omega_i^m = \frac{\phi(g_i, \omega_i^m)}{\gamma_L}$ and belongs to the domain $\bar{\omega}_i^m(g_i) \geq \bar{\phi} + \varepsilon_{\bar{\phi}}$

Consider the new coordinate $z_i = \omega_i^m - \frac{\phi(g_i, \omega_i)}{\gamma_L}$ for all $i \in \mathbb{I}$. Then,

$$
\begin{aligned}
\dot{z}_i &= \dot{\omega}_i^m - \frac{d}{dt} \frac{\phi(g_i, \omega_i)}{\gamma_L} \\
&= -\frac{\gamma_L}{\varepsilon} z_i - \frac{1}{\gamma_L} \left(\frac{\partial \phi(g_i, \omega_i)}{\partial \omega_i} \dot{\omega}_i + \frac{\partial \phi(g_i, \omega_i)}{\partial g_i} \dot{g}_i \right) \\
&= -\frac{1}{\varepsilon} \left(\gamma_L - \frac{\partial \phi(g_i, \omega_i)}{\partial \omega_i} \right) z_i - \frac{1}{\gamma_L} \frac{\partial \phi(g_i, \omega_i)}{\partial g_i} \dot{g}_i.
\end{aligned}
$$

(6.9)

By introducing $\tau = \frac{t}{\varepsilon}$, in the limit of $\varepsilon = 0$, we obtain the boundary layer system

$$
\frac{dz_i}{d\tau} = - \left(\gamma_L - \frac{\partial \phi(g_i, \omega_i)}{\partial \omega_i} \right) z_i, \quad \text{for} \quad i \in \mathbb{I}.
$$

which is an exponentially stable system in the neighborhood of the equilibrium $\bar{\omega}_i^m(g_i) \geq \bar{\phi} + \varepsilon_{\bar{\phi}}$ for $\gamma_L > \frac{\partial \phi(g_i, \omega_i)}{\partial \omega_i} \simeq 0$.

Part 2: exponential stability of the reduced-order system

The reduced order system is obtained from (6.1)-(6.7) by replacing the diagonal matrix Ω_m with the diagonal matrix $\bar{\Omega}_m(g)$ whose elements on the diagonal are given by $\bar{\omega}_i^m(g_i) \geq \bar{\phi}$,

whenever $i \in \mathbb{I}$, and by $\omega_i^m(0)$, otherwise. We use a contraction argument to prove exponential stability of the reduced system equilibrium.

Part 2.a: widened reduced system and linearization. As a first step, consider the "widened" reduced order system obtained by replacing $\bar{\Omega}_m(g)$ with $\bar{\Omega}_m(q)$ where $q(\cdot) : \mathbb{R} \to \mathbb{R}^n$ is any differentiable signal. The set of trajectories of the widened reduced system contains the original reduced system trajectories, corresponding to additional constrain $q = g$. As second step, consider the linearized dynamics of the widened reduced order system

$$\delta\dot{m} = (L - \bar{\Omega}_m(q(t)))\delta m + B\delta u$$
$$\delta\dot{g} = S\delta m - \Omega_g \delta g$$
$$\delta\dot{u} = -k_G \frac{\partial h}{\partial g}\left(\frac{\mathbf{1}^T g}{n}\right)\frac{\mathbf{1}^T}{n}\delta g - \omega_u \delta u$$

where h corresponds to the function arising from the composition of (6.3)-(6.5). In what follows we construct a differential Lyapunov function to show exponential contraction of the system [57], which implies exponential stability.

Part 2.b: diagonal Lyapunov matrix P for the transport sub-dynamics. Consider the system $\dot{\eta} = (L - \rho I)\eta$ where $\rho > 0$ is a generic real constant. Following Chapter 4 in [52], this system is positive (off-diagonal elements are all non-negative) and irreducible (by the connectedness assumption on the neuron topology and the fact that $l_{ij} \neq 0$ iff $l_{ji} \neq 0$, for all $i \neq j$). Furthermore, each column of L sums to zero therefore each column of $L - \rho I$ sums to $-\rho$. As a consequence, the system has a dominant eigenvalue in $-\rho$. All other eigenvalues have smaller negative real part. Thus, by Theorem 15 in [52], for any $\rho > 0$ there exists a positive definite and diagonal matrix P such that $(L - \rho I)^T P + P(L - \rho I) < 0$. Take P to be any positive diagonal solution to this inequality for $\rho = \frac{1}{2}\min_{i \notin \mathbb{I}}\{\bar{\phi}, \omega_i(0)\}$, which ensures $\rho \leq \frac{1}{2}\lambda_{\min}(\bar{\Omega}_m(q(t)))$, for all t.

Part 2.c: Lyapunov argument. Consider now the differential Lyapunov function

$$V = \frac{\rho_m}{2}\delta m^T P \delta m + \frac{\rho_g}{2}\delta g^T \delta g + \frac{1}{2}\delta u^T \delta u.$$

We have

$$\dot{V} = 1/2\rho_m \delta m^T (L^T P + PL)\delta m - \rho_m \delta m^T P \bar{\Omega}_m(q(t))\delta m$$
$$+ \rho_m \delta m^T P \delta u + \rho_g \delta m^T S \delta g - \rho_g \delta g^T \Omega_g \delta g$$
$$- k_G \frac{\partial h}{\partial g}\left(\frac{\mathbf{1}^T g}{n}\right)\frac{\mathbf{1}^T}{n}\delta g \delta u - \omega_u \delta u^T \delta u$$
$$= 1/2\rho_m \delta m^T ((L - \rho I)^T P + P(L - \rho I))\delta m$$
$$- \rho_m \delta m^T P(\bar{\Omega}_m(q(t)) - \rho I)\delta m$$
$$+ \rho_m \delta m^T P \delta u + \rho_g \delta m^T S \delta g - \rho_g \delta g^T \Omega_g \delta g$$
$$- k_G \frac{\partial h}{\partial g}\left(\frac{\mathbf{1}^T g}{n}\right)\frac{\mathbf{1}^T}{n}\delta g \delta u - \omega_u \delta u^T \delta u \ .$$

Then, using $(L - \rho I)^T P + P(L - \rho I) < 0$, can be bounded by the following inequality

$$\dot{V} \leq \begin{bmatrix}|\delta m|\\|\delta g|\\|\delta u|\end{bmatrix}^T \underbrace{\begin{bmatrix}-\lambda_1 & 0 & \lambda_6\\ \lambda_2 & -\lambda_3 & 0\\ 0 & \lambda_4 & -\lambda_5\end{bmatrix}}_{-Q}\begin{bmatrix}|\delta m|\\|\delta g|\\|\delta u|\end{bmatrix}$$

where

$$\lambda_1 = \frac{\rho_m}{2}\min_{i\notin\mathbb{I}}\{\bar{\phi}, \omega_i(0)\} \leq \frac{\rho_m}{2}\lambda_{\min}(\bar{\Omega}_m(q(t))) \quad \forall t$$
$$\lambda_2 = \rho_g|S|$$
$$\lambda_3 = \rho_g\lambda_{\min}(\Omega_g)$$
$$\lambda_4 = k_G|\frac{\partial h}{\partial g}\left(\frac{\mathbf{1}^T g}{n}\right)\frac{\mathbf{1}^T}{n}|$$
$$\lambda_5 = \omega_u$$
$$\lambda_6 = \rho_m|P|.$$

The problem now reduces to proving that $Q > 0$. Firstly, we write the equivalent symmetric problem $\frac{Q + Q^T}{2} > 0$, that is,

$$\begin{bmatrix} \frac{\rho_m}{2}\min_{i\notin\mathbb{I}}\{\bar{\phi},\omega_i(0)\} & -\frac{\rho_g}{2}|S| & -\frac{\rho_m}{2}|P| \\ -\frac{\rho_g}{2}|S| & \rho_g\lambda_{\min}(\Omega_g) & -\frac{k_G}{2}|\frac{\partial h}{\partial g}\left(\frac{\mathbf{1}^T g}{n}\right)\frac{\mathbf{1}^T}{n}| \\ -\frac{\rho_m}{2}|P| & -\frac{k_G}{2}\left|\frac{\partial h}{\partial g}\left(\frac{\mathbf{1}^T g}{n}\right)\frac{\mathbf{1}^T}{n}\right| & \omega_u \end{bmatrix} > 0$$

Next, by Sylvester's criterion, the above matrix is positive-definite provided that its leading principal minors are positive. For the first minor is

$$\frac{\rho_m}{2}\min_{i\notin\mathbb{I}}\{\bar{\phi},\omega_i(0)\} > 0 \iff \rho_m > 0 \tag{6.10}$$

For the second minor we get

$$\frac{1}{2}\rho_m\rho_g\lambda_{\min}(\Omega_g)\min_{i\notin\mathbb{I}}\{\bar{\phi},\omega_i(0)\} - \frac{\rho_g^2|S|^2}{4} > 0$$

$$\iff \boxed{\rho_m > \frac{|S|^2}{2\lambda_{\min}(\Omega_g)\min_{i\notin\mathbb{I}}\{\bar{\phi},\omega_i(0)\}}\rho_g} \tag{6.11}$$

For the third minor we get

$$\frac{\rho_m}{2}\min_{i\notin\mathbb{I}}\{\bar{\phi},\omega_i(0)\}\left(\omega_u\lambda_{\min}(\Omega_g)\rho_g - \frac{k_G^2}{4}\left|\frac{\partial h}{\partial g}\left(\frac{\mathbf{1}^T g}{n}\right)\frac{\mathbf{1}^T}{n}\right|^2\right) +$$

$$+\frac{\rho_g}{2}|S|\left(-\frac{\omega_u}{2}|S|\rho_g - \frac{1}{4}k_G\left|\frac{\partial h}{\partial g}\left(\frac{\mathbf{1}^T g}{n}\right)\frac{\mathbf{1}^T}{n}\right|\rho_m|P|\right) +$$

$$-\frac{\rho_m}{2}|P|\left(\frac{1}{4}k_G\left|\frac{\partial h}{\partial g}\left(\frac{\mathbf{1}^T g}{n}\right)\frac{\mathbf{1}^T}{n}\right||S|\rho_g + \frac{1}{2}\lambda_{\min}(\Omega_g)|P|\rho_g\rho_m\right) > 0.$$

Rearranging

$$\lambda_{\min}(\Omega_g)\left(\frac{\omega_u}{2}\min_{i\notin\mathbb{I}}\{\bar{\phi},\omega_i(0)\}\rho_m\rho_g - \frac{1}{4}\left[|P|^2\rho_g\rho_m^2 + \omega_u|S|^2\rho_g^2\right]\right)$$

$$> \frac{1}{4}\left(k_G|\frac{\partial h}{\partial g}\left(\frac{\mathbf{1}^T g}{n}\right)\frac{\mathbf{1}^T}{n}||S||P|\rho_g\rho_m + \frac{k_G^2}{2}\left|\frac{\partial h}{\partial g}\left(\frac{\mathbf{1}^T g}{n}\right)\frac{\mathbf{1}^T}{n}\right|^2\lambda_{\min}(\bar{\Omega}_m)\rho_m\right)$$

which can written as

$$\lambda_{\min}(\Omega_g)\left(\frac{\omega_u}{4}\min_{i\notin\mathbb{I}}\{\bar{\phi},\omega_i(0)\}\rho_m\rho_g - \frac{1}{4}|P|^2\rho_g\rho_m^2\right) \tag{6.12}$$

$$+\left(\frac{\omega_u}{4}\min_{i\notin\mathbb{I}}\{\bar{\phi},\omega_i(0)\}\lambda_{\min}(\Omega_g)\rho_m\rho_g - \frac{1}{4}\omega_u|S|^2\rho_g^2\right) \tag{6.13}$$

$$>\frac{1}{4}\left(k_G\left|\frac{\partial h}{\partial g}\left(\frac{\mathbf{1}^T g}{n}\right)\frac{\mathbf{1}^T}{n}\right||S||P|\rho_g\rho_m\right) \tag{6.14}$$

$$+\frac{1}{4}\left(\frac{k_G^2}{2}\left|\frac{\partial h}{\partial g}\left(\frac{\mathbf{1}^T g}{n}\right)\frac{\mathbf{1}^T}{n}\right|^2\rho_m\min_{i\notin\mathbb{I}}\{\bar{\phi},\omega_i(0)\}\right) \tag{6.15}$$

In order for the above inequality to hold, we need sum of the terms (6.12) and (6.13) to dominate that of (6.14) and (6.15) . As a first step, we observe that (6.14) and (6.15) can be made arbitrarily small by setting $0 < k_G \ll 1$. Thus, what remains to show is that the terms of (6.12) and (6.13) are positive; this can be guaranteed by satisfying the following relations:

$$\text{from (6.12) :} \quad \boxed{\rho_m < \frac{\omega_u \min\limits_{i \notin \mathbb{I}}\{\bar{\phi}, \omega_i(0)\}}{|P|^2}} \tag{6.16}$$

$$\text{from (6.13):} \quad \boxed{\rho_m > \frac{|S|^2}{\min\limits_{i \notin \mathbb{I}}\{\bar{\phi}, \omega_i(0)\}\lambda_{\min}(\Omega_g)}\rho_g} . \tag{6.17}$$

Therefore, combining (6.10), (6.11), (6.16), and (6.17), we conclude that the widened reduced systems satisies $\dot{V} \leq -\bar{\lambda}V$ for some $\bar{\lambda} > 0$, whenever $\rho_m, \rho_g, k_G > 0$ satisfy

1. $\dfrac{\omega_u \min\limits_{i \notin \mathbb{I}}\{\bar{\phi}, \omega_i(0)\}}{|P|^2} > \rho_m > \dfrac{|S|^2}{\min\limits_{i \notin \mathbb{I}}\{\bar{\phi}, \omega_i(0)\}\lambda_{\min}(\Omega_g)}\rho_g.$

2. k_G is sufficiently small.

Part 2.d: exponential stability of the reduced system. The exponential decay of the differential Lyapunov function guarantees incremental exponential stability of the widened reduced system, [57, Theorem 1]. This implies exponential stability of the equilibrium of the reduced system.

6.7.2 Proof of Theorem 4

The proof of the theorem corresponds to the argument in Part 2 in the proof of Theorem 5. There is just a minor difference in the use of the matrix Ω_m, which contains fixed elements ω_i^m. In other words, the proof steps are identical except that *part 2.a* is no longer needed, since the dependence on g is no longer present. Then, a differential Lyapunov function is proposed, along with contraction argument, to prove exponential stability the equilibrium.

Chapter 7

From linear to nonlinear transport: stable and pathological scaling

> *"The problem with linear theory is that it is not nonlinear."*
>
> ———————————————————
>
> John A. Adam, *Mathematics in Nature*

In order to capture the effects of finite capacity of dendritic arbor and microtubules, we model the active transport of inactive cargo *m* as a nonlinear phenomenon. We also explore the biological ramifications of varying the timescale of somatic cargo production. Using dominance theory presented in Section 2.3, we analyze the behavior of the model qualitatively, and asses how robust the system is to static and dynamics uncertainties.

7.1   Introduction and motivation

In the previous chapters we studied various aspects of synaptic scaling. In Chapters 3-5 we focused on the convergence rate, robustness, and accuracy of scaling. In Chapter 6 we paid special attention to the role of activity-dependent degradation on its effects on performance. The goal was to explore further how global-local regulation mechanisms shape the neuron's overall behavior. Here, we take a deeper look at the trafficking phenomena, by replacing it with a more detailed transport system. Moreover, we explore the implication of varying the timescale of cargo production on performance, and how it cooperates with the new trafficking model.

We consider two modifications to the model presented in Chapter 6. The first modification is related to the cargo transport mechanism, i.e. the *m* dynamics. In the previous chapters

we modeled cargo transport as a linear phenomenon, that is, the forward and backward trafficking rates were fixed. Here we relax this assumption by replacing the *m* dynamics with a nonlinear active transport model. The second modification is related to the cargo production dynamics. This is done to explore fast production regimes, needed to compensate for delays that can arise from a nonlinear trafficking system.

7.2 Modifications to the closed loop model

7.2.1 Nonlinear compartmental model for dendritic trafficking

For expository purposes we refer to the abstract neuron shown in Figure 7.1, characterized by a simple line of compartments. We model mRNA trafficking by revisiting how microscopic active transport along microtubules affects concentration m_i in each compartment. Inspired by [127], we derived a mean-field approximation of the random process governed by a *Simple Exclusion Principle* [140] taking into account crowding effects of cargo particles. This results in the following nonlinear $(n+1)-$compartmental model, with finite capacity compartments, describing dendritic trafficking
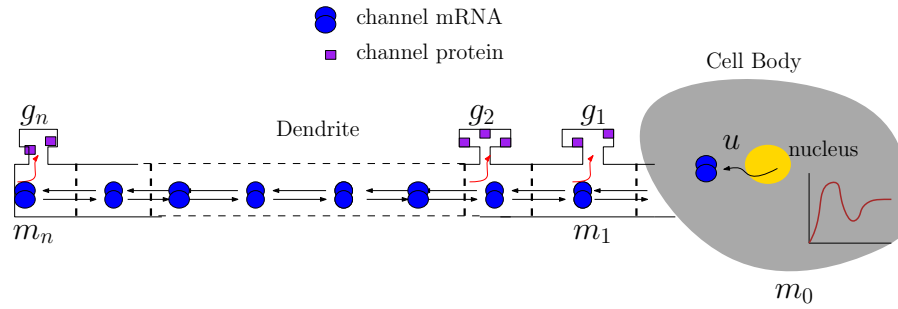
Fig. 7.1 An abstract visualization of neuron showing where different physiological processes take place.

$$\dot{m}_0 = u - m_0(c - m_1) - \omega_m m_1 \tag{7.1}$$
$$\dot{m}_1 = m_0(c - m_1) - v_f m_1(c - m_2) + v_b m_2(c - m_1) - \omega_m m_1$$
$$\dot{m}_i = v_f m_{i-1}(c - m_i) - v_b m_i(c - m_{i-1}) + v_b m_{i+1}(c - m_i)$$
$$\qquad - v_f m_i(c - m_{i+1}) - \omega_m m_i$$
$$\dot{m}_n = v_f m_{n-1}(c - m_n) - v_b m_n(c - m_{n-1}) - \omega_m m_n.$$

In (7.1), m_0 is the mRNA concentration in the soma and $m_i \in [0, c]$ for $i \in 1, 2, \dots n$ is mRNA concentration in the ith compartment, bounded above by a capacity, c; v_f, v_b, w are forward velocity, backward velocity, and mRNA degradation, respectively; u is a homeostatic cargo synthesis rate, which will be formulated later. In comparison to the **CLSS** model, c in (7.1) is a capacity parameter and resembles the c_i's in (3.2). However, in (7.1) those spatial parameters are uniform. In both settings, the effect of finite space is captured in the same way; in the **CLSS** model, the level of occupancy in synaptic sites is given by $(c_i - g_i)$, while the level of occupancy in dendritic compartments is given by $(c - m_i)$.

7.2.2   Cargo production dynamics with varying timescale

Here we consider a modified global controller that takes the error signal $e_G = [\text{Ca}^{2+}]_{\text{target}} - [\text{Ca}^{2+}]$ in the following fashion:

$$\tau_u \dot{u} = k_G e_G - \omega_u u - \vartheta(u) \tag{7.2}$$

where $\omega_u > 0$ sets the degradation rate of u and $\vartheta(u)$ enforces positivity and boundedness of u. A typical $\vartheta(u)$ is plotted in Figure 7.2. Here, for simplicity, we take $\vartheta(u) = a \tan\left(\frac{\pi}{c_u}\left(u - \frac{c_u}{2}\right)\right)$, for $0 < a \ll 1$.
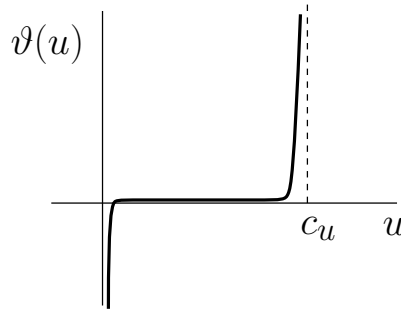
Fig. 7.2 A typical function $\vartheta(u)$.

The remaining parts of the models are not changed from the previous chapter. For readability, we list them below.

$$\text{Protein dynamics:} \quad \tau_g \dot{g}_i = s_i m_i - \omega_g g_i \tag{7.3}$$

$$\text{Calcium signal:} \quad [\text{Ca}^{2+}] = \frac{\alpha}{1 + \exp V / \beta} \tag{7.4}$$

$$\text{Membrane potential:} \quad V = \frac{g_{avg} E_g + g_{leak} E_{leak}}{g_{leak} + g_{avg}}, \quad g_{avg} = \frac{\Sigma g_i}{n}. \tag{7.5}$$

In (7.1), we ignored finite space effects in m_0. This is done for mathematical convenience reasons to prove the stability of the closed loop system. Nevertheless, adopting a finite capacity soma c_0 does not alter the conclusions and behavior. In other words, if the cargo synthesis rate is replaced with the following term

$$u(c_0 - m_0)$$

in (7.1) it does not drastically change the behavior. This was shown in [5]. Similarly, the assumption is unchanged in the next chapter. The stability result below is a restatement of Theorem 4 with nonlinear transport, and with varying global controller timescale.

Theorem 6 *Under Assumption 1, there exists a minimal time constant $\bar{\tau}_u > 0$ such that, for every $\tau_u > \bar{\tau}_u$, and $[Ca^{2+}]_{target}$ the closed loop system comprised of (7.1)-(7.5) has a globally exponentially stable equilibrium.*

The above theorem guarantees that the overall behavior is similar to the one of the models discussed in previous chapters, in spite of the finite capacity of the dendritic compartments. In other words, the nonlinearity in the form of saturation in the modified trafficking system does not fundamentally changes the property of the system. The system's input-output characteristics remain qualitatively similar. We further elaborate this through parametric analysis in the following sections.

7.3   Model behavior and nominal parameters

Table 7.1 Nominal Parameter Values

$v_f = 1\ \mu m s^{-1}$	$v_b = 0.5\ \mu m s^{-1}$	$\omega_m = 0.1\ s^{-1}$	$g_{leak} = 0.25\ \mu S$
$E_{leak} = -50\ mV$	$E_g = 20\ mV$	$\alpha = 1$	$a = 0.0001$
$\beta = 1$	$\tau_g = 1$	$\omega_g = 0.1\ s^{-1}$	$\tau_u =$ varies
$[Ca^{2+}]_{target} = 0.5\ \mu M$	$c = 1$	$\omega_u = 1 \times 10^{-5}\ s^{-1}$	$n = 3$

Using the nominal parameter values in Table 7.1, Figure 7.3a-7.3c summarize the behavior of the model for different values of the integration constant $\tau_u \in \{1000, 100, 10\}$. Stable regulation is achieved for large integrator time constant τ_u (slow feedback). Performance improves for smaller time constants (fast feedback). However, performance rapidly degrades with the occurrence of pathological oscillations when the integral feedback becomes too aggressive ($\tau_u = 10$). A nonzero ω_u will lead to imperfect tracking. The analysis in Section

7.4 shows that these simulations capture the generic robust behavior of the closed loop system.

(a) $\tau_u = 1000$ (b) $\tau_u = 100$ (c) $\tau_u = 10$

(d) $\tau_u = 1000$ (e) $\tau_u = 100$ (f) $\tau_u = 10$
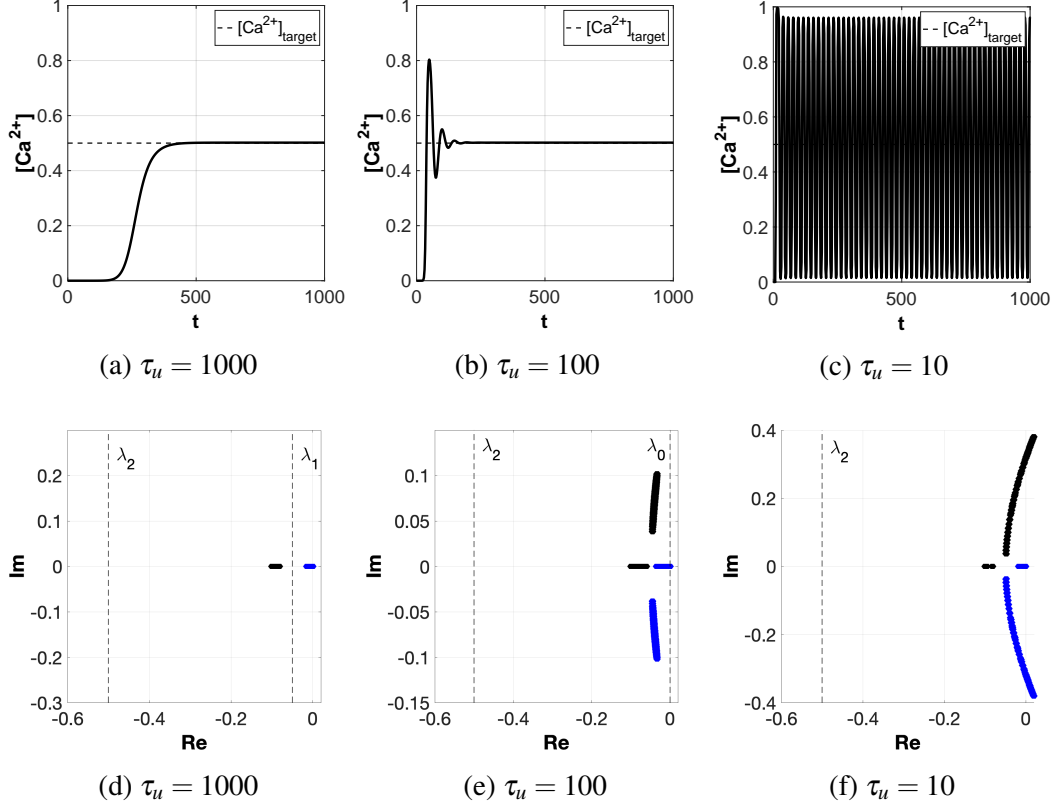
Fig. 7.3 a-c Response of $[Ca^{2+}]$ for different values of τ_u where the dendritic trafficking model was simulated with the nominal parameter values in Table 7.1 and Initial condition $x_0 = [0.05; 0.05; 0.05; 0.05; 0.05]^T$.d-f two right-most eigenvalues of the Jacobian of the closed loop system. For Figure e the right-most eigenvalue does not cross the imaginary axis. Spectra were obtained by sampling $0.05 \le x_i \le 0.95$, where the black and blue dots depict the movement of the two right-most eigenvalues.

7.4   Nominal behavior and differential analysis

Denoting by $\dot{x} = f(x)$ the closed loop dynamics, Figure 7.3d-7.3f show the position of the eigenvalues of the Jacobian $\partial f(x)$ for different levels of control aggressiveness, through the selection of values $\tau_u \in \{1000, 100, 10\}$ and x, for nominal parameter values in Table 7.1. For readability, we show only the two right-most eigenvalues of the Jacobian. The others are always to the left of -0.5. Figure 7.3d-7.3f can be roughly separated in two groups: *stable linearization - $\partial f(x)$* has stable eigenvalues; *Hopf-bifurcation - $\partial f(x)$* has unstable complex eigenvalues. These two groups explain the difference between stable regulation at steady

state and the appearance of oscillations for small τ_u. For instance, for large $\tau_u = 1000$ (slow feedback) there are two real, stable eigenvalues, as shown in Figure 7.3d. This is compatible with the behavior in Figure 7.3a. As the integrator dynamics becomes faster, $\tau_u = 100$, the two right most eigenvalues coalesce and bifurcate, Figure 7.3e. Convergence becomes faster, as shown in Figure 7.3b but damped oscillations may appear. Finally, for aggressive feedback, $\tau_u = 10$, the complex unstable eigenvalues in Figure 7.3f justify the occurrence of sustained oscillations in Figure 7.3c.

The connection between Jacobian eigenvalues and closed loop behavior can be made rigorous through dominance analysis, by solving the linear matrix inequality (2.7) for $\{m_i, g\} \in [0.05c, 0.95c]$, and using rates $\lambda_0, \lambda_1, \lambda_2$ in Figure 7.3d-7.3f; CVX [66] was used to numerically solve (2.7) for each case of τ_u. The first observation is that the system is always $2-$dominant with rate $\lambda_2 = 0.5$. A common solution P can be found for $\tau_u \in [3, 3000]$. This has a striking conclusion: the steady state of the closed loop system is compatible with planar dynamics, captured by a simple attractor. This means that for $\tau_u \in [3, 3000]$ the closed loop system *either converges to a fixed point or enters into sustained oscillations*. This conclusion can be refined:

- ($\tau_u = 1000$) For slow feedback, $\lambda_1 = 0.05$ separates the two real eigenvalues into two subgroups as shown in Figure 7.3d. Feasibility of (2.7) shows that the system is 1-dominant with rate $\lambda_1 = 0.05$, which guarantees *convergence to a fixed point*.

- ($\tau_u = 100$) As the integrator dynamics become faster the two right most eigenvalues bifurcate and $1-$dominance is lost (Figure 7.3e). However, the system is still $0-$dominant locally with rate $\lambda_0 = 0$. This guarantees *local convergence to the fixed point*.

- ($\tau_u = 10$) For aggressive integrator dynamics the system is $2-$dominant with rate $\lambda_2 = 0.5$. It cannot be 1-dominant (complex right-most eigenvalues) and it cannot be 0-dominant (unstable eigenvalues). 2-dominance combined with the instability of the fixed point guarantees that *sustained oscillations are the only possible steady state behavior*.

Figure 7.3 demonstrates the convergence rate and robustness tradeoff from the previous chapters. Previously, this tradeoff was mediated by the feedback gain k_G. Here, the same tradeoff is replicated but for variation in the feedback time constant τ_u. Combining Figure 7.3 to the observations from previous chapters, both the gain and the time constant of feedback improve the settling time at the cost of emergence of oscillations. Both parameters have the same effect on the performance of synaptic scaling.

Using dominance theory, we are able to further extend the convergence rate and robustness tradeoff. It actually reveals a regime where the settling time can improve with minimal or no emergence of oscillations. This is represented by the $1-$dominance region. Beyond this region, decaying oscillations arise and become pronounced; this is the $0-$dominance region. The two combined regions are related to the convergence rate and robustness tradeoff, shown in Figure 4.15. The plot can be decomposed into two parts. In the first, the regulation is nominal with no emergence of oscillation ($1-$dominance). In the second part, regulation is aggressive with damped oscillations ($0-$dominance). Beyond these two regimes, regulation is no longer maintained and the behavior is pathological ($2-$dominance). In the following section, we derive parameter ranges for each region.

7.5 Robustness to static and dynamic uncertainties

7.5.1 Parametric uncertainties

The analysis above shows how the feedback time constant τ_u affects regulation. We now study robustness to other physiologically relevant parameters (such as velocities and length) using dominance theory, looking at the three regimes $\tau_u \in \{1000, 100, 10\}$. For $\tau_u = 1000$ a stable closed loop behavior is preserved for any uncertainty in Table 7.2 (left column). For $\tau_u = 10$, the robustness of the oscillatory regime is guaranteed for parameter ranges specified in Table 7.2 (right column). A local robust analysis is also developed for $\tau_u = 100$. This is a fragile case for dominance analysis, which we address numerically by looking at specific local regions.

Table 7.2 Parameter ranges for $\{1,2\}$-dominance

	$1-$dom: $\tau_u = 2000$, $\lambda = 0.05$	$2-$dom: $\tau_u = 20$, $\lambda = 0.5$
v_f $[\mu m s^1]$	$[0.2, 1.5]$	$[0.5, 1.5]$
v_b $[\mu m s^1]$	$[0.3, 1.2]$	$[0.4, 1.5]$
τ_g	$[0.1, 1.5]$	$[0.5, 1.5]$

For $\tau_u = 1000$, the controller guarantees robust 1-dominance with rate $\lambda = 0.05$ to uncertainties in Table 7.2 (left column). Indeed, the matrix P_1 in Table 7.3 is a solution to (2.7) for all parametric uncertainties in Table 7.2 (left column). Robust stable regulation is thus guaranteed for these uncertainties. Stable regulation is also preserved when the velocity constants are replaced by nonlinear functions $v_f(m_{i-1}, m_i, m_{i+1})$ and $v_b(m_{i-1}, m_i, m_{i+1})$ whose slopes v'_f and v'_b belong to the intervals defined in Table 7.2.

Table 7.3 Solutions to (2.7) for uncertainties in Table 7.2.

1−dominance	2−dominance

$$P_1 = \begin{bmatrix} 53.7188 & 45.0058 & 47.1634 & 0.4707 & -476.4789 \\ 45.0058 & 58.9272 & 50.1640 & -2.1185 & -499.3479 \\ 47.1634 & 50.1640 & 59.7843 & -5.7063 & -495.9245 \\ 0.4707 & -2.1185 & -5.7063 & 7.2869 & -1.5904 \\ -476.4789 & -499.3479 & -495.9245 & -1.5904 & 33.7697 \end{bmatrix} \quad P_2 = \begin{bmatrix} 7.4607 & -29.7730 & -59.3040 & -1.5610 & -22.0651 \\ -29.7730 & 2.2651 & -22.8007 & -8.4190 & 7.8215 \\ -59.3040 & -22.8007 & 33.1752 & -12.6506 & 50.0661 \\ -1.5610 & -8.4190 & -12.6506 & 11.9041 & 25.8331 \\ -22.0651 & 7.8215 & 50.0661 & 25.8331 & -52.7973 \end{bmatrix}$$

For $\tau_u = 10$, the closed loop system is robustly 2-dominant with rate $\lambda = 0.5$ to uncertainties in Table 7.2 (right column). This is certified by the matrix P_2 in Table 7.3 which is a solution to (2.7) for all parametric uncertainties in Table 7.2 (right column). As discussed in other sections, 2−dominance is not sufficient to claim robust oscillations. However, the unique equilibrium of the system is always unstable for parameters in Table 7.2 (right column) which, combined with 2-dominance, guarantees robust oscillations.

For $\tau_u = 100$, the closed loop is moving from a stable to an oscillatory regime (complex stable poles in the Jacobian). High sensitivity to parameter variations is thus expected. Table 7.4 shows the trade-off between parameter ranges and size of the region of 0−dominance.

Table 7.4 0−dominance: $\tau_u = 200$, $\lambda = 0$.

	25% around x^*	20% around x^*	15% around x^*
$v_f\ [\mu m s^1]$	$[0.7, 1.5]$	$[0.6, 1.7]$	$[0.5, 1.8]$
$v_b\ [\mu m s^1]$	$[0.4, 1.3]$	$[0.3, 1.4]$	$[0.2, 1.5]$
τ_g	$[0.5, 1.2]$	$[0.3, 1.5]$	$[0.15, 1.65]$

The robustness analysis done in Chapter 4 differs from the one presented here. In Figure 4.5b, the Nyquist criterion provided a graphical tool to study parametric variations, where we varied one parameter at a time. Furthermore, let p be a parameter in our model, and let's assume that we are considering parameter range $[p_{min}, p_{max}]$. It is not possible to conclude that the closed loop system will be stable for the parameter range by only testing the Nyquist plot corresponding to the minimum and maximum parameter value, namely p_{min} and p_{max}. This is due to the rational representation of transfer functions. Using dominance theory, however, we saw how we were able to derive robustness results for multiple parameter ranges at a time, by computing a single matrix P. This was done for 0−, 1−, and 2-dominance.

7.5.2   A special case of robustness: growth

How does a neuron tune its transcription rate in the presence of growth? A bigger neuron requires more biomolecules to be synthesized and their traveling distance is longer. With

these variations, can a neuron withstand and maintain a stable nominal behavior? Growth can be modeled in two ways: by increasing the number of compartments or by adapting capacity and velocity parameters. We adopt the latter for simplicity.

We consider 1-dimensional growth, where L represents the neuron's total length. The identity $c = L/n$ relates length L to compartment's capacity c and to compartments number n. Growth corresponds to larger L thus larger capacities. Forward and backward speeds are also updated accordingly. Starting from the microscopic picture, suppose that each compartment can fit c number of molecules as shown in Figure 7.4. The figure shows a large compartment z_j of capacitance c and its constituent unit compartments x_i's, each of capacity 1. Both representations are of the same trafficking system, but with different discretizations. In fact, both x and z capture m concentrations, but with different capacities. The rate of change of molecules in compartment z_j is given by

$$\dot{z}_j = vx_{i-1}(1 - x_i) - vx_{i+c-1}(1 - x_{i+c}) \tag{7.6}$$

where the internal exchange of molecules sum to zero. We focus on particles that enter and leave z_j, assuming that particles are homogeneously distributed and spatially indistinguishable (well-mixed) in each compartment z_j, that is,

$$x_i = x_{i+1}\cdots = x_{i+c-1} = \frac{z_j}{c}. \tag{7.7}$$

Substituting (7.7) into (7.6), we get

$$\begin{aligned}
\dot{z}_j &= v\frac{z_{j-1}}{c}\left(1 - \frac{z_j}{c}\right) - v\frac{z_j}{c}\left(1 - \frac{z_{j+1}}{c}\right) \\
&= \frac{v}{c^2}z_{j-1}\left(c - z_j\right) - \frac{v}{c^2}z_j\left(c - z_{j+1}\right).
\end{aligned} \tag{7.8}$$

Equation (7.8) shows that, by increasing L, the compartment size increases linearly and the velocities scale with $1/c^2$ or equivalently $1/L^2$. In summary, growth is modeled by the following parameter scaling in (7.1):

$$v_f \to \frac{v_f}{c^2}, \ v_b \to \frac{v_b}{c^2}, \ c = \frac{L}{n}. \tag{7.9}$$

Within this modeling framework, the question of growth reduces to a question of robustness to parameter variations. The first question is: given an integrator time constant τ_T, how much can the neuron grow before loosing stability? We answer through $1-$dominance, by deriving intervals of length L that guarantee 1-dominance for a fixed time constant τ_u, as shown in Figure 7.5a. As expected, stable regulation for longer neurons requires less aggressive
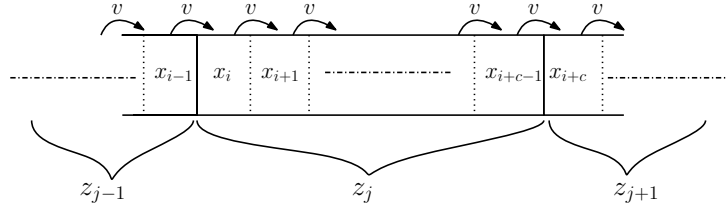
Fig. 7.4 A schematic representation of equations (7.6)-(7.7).

feedback (larger τ_u). For any time constant τ_u, there is a threshold length after which 1-dominance is lost. This regime is characterized by the emergence of damped oscillations, which eventually degrade into sustained oscillations for longer lengths. In fact, Figure 7.5b shows that 2-dominance of the closed loop is preserved for large variations (both on L or τ_u) with limit cycles appearing when the time constant is sufficiently small or the length is sufficiently large, that is, when the equilibrium of the system loses stability.

Figure 7.5a agrees with the conclusion we made by employing the **CLSS** model: it is harder to regulate larger cells and networks. Since we showed that real morphologies can be mapped into simple lines, shorter cells can tolerate more aggressive cargo synthesis, and not suffer from the emergence of oscillations.

(a) $1-$dominance with $\lambda_1 = 0.047$ (b) $2-$dominance with $\lambda_2 = 0.4$
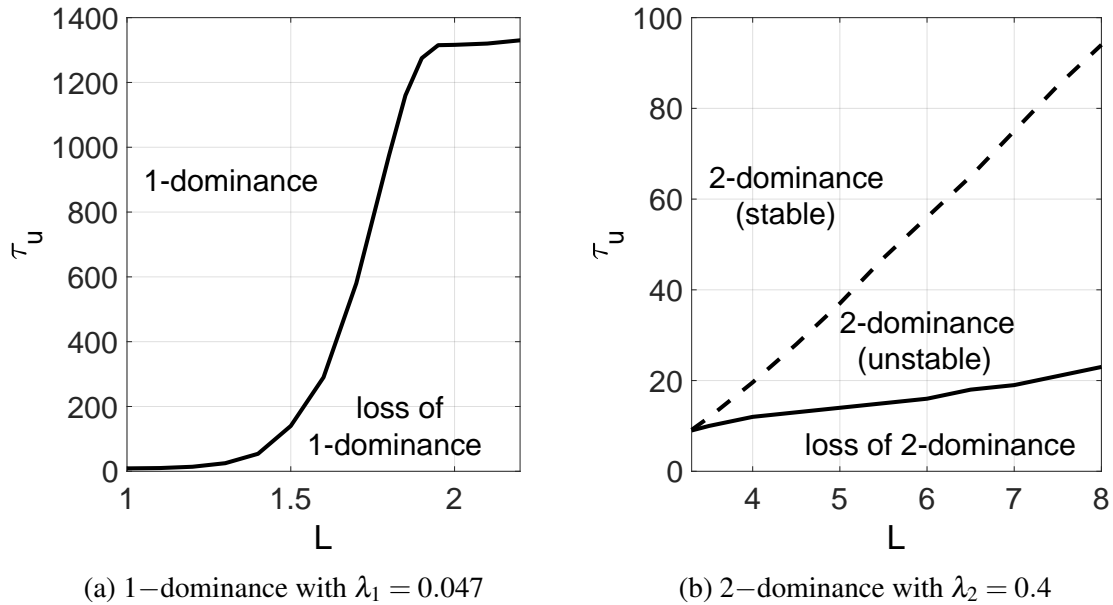
Fig. 7.5 Trade-off between τ_u and L for $1-$ and $2-$dominance.

7.5.3 Unmodeled dynamics

Both growth and parametric variations have been modeled in previous sections as *static* uncertainties. We now consider *dynamic* uncertainties typically arising from unmodeled dynamics and modelling simplifications.We will model these uncertainties as (possibly nonlinear) 0-dominant dynamic perturbations, Δ_m, acting on the nominal closed loop as shown in Figure 7.6. Δ_m corresponds to additive perturbations, such as neglected transport phenomena. uncertainties such as neglected fast dynamics in protein synthesis.

We assess the robustness of the closed loop using the notion of p-gain in Section 2.3 and the small gain interconnection in Proposition 2, which guarantees that perturbations do not affect the the dominance of the closed loop if the product of the nominal gain and of the perturbation gain is less than one. Indeed, for the nominal parameters in Table 7.1, solving (2.8), the nominal closed loop in Figure 7.6 has 1-gain $\gamma_{cl_1} = 0.4549$ from u_1 to y_1 with rate $\lambda_1 = 0.05$. 1-dominance of the closed loop, i.e. steady regulation, is thus preserved for any perturbation Δ_m whose 0-gain γ_m satisfies $\gamma_m < 1/\gamma_{cl_1}$ with rate λ_1.
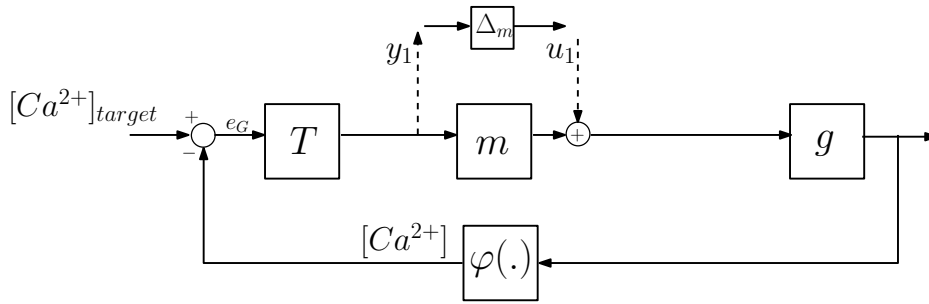
Fig. 7.6 A schematic showing how the unmodeled dynamics affect the nominal closed loop as dynamic perturbations.

As an example we study closed loop regulation when the 3-compartmental model of transport Σ_3 is replaced by a more detailed N-compartmental model Σ_N, $N > 3$. For this case Δ_m represents the mismatch dynamics $\Sigma_N - \Sigma_3$. For simplicity we restrict our analysis to linear transport models, that is, we take Σ_3 as in (7.1) but ignore compartment saturation. Σ_N is also a linear compartmental system. Figure 7.7 shows how the 0-gain γ_m (rate 0.05) of Δ_m changes with the number of compartments. For the nominal parameters in Table 7.1, γ_m peaks at 2.1575, which guarantees that the closed loop behavior remains unchanged if we replace our 3-compartmental transport model with a more detailed transport model based on $3 \leq N \leq 100$ compartments.

A similar analysis can be developed to account for unmodeled protein dynamics to show that sufficiently fast reactions can be safely neglected. These examples show the
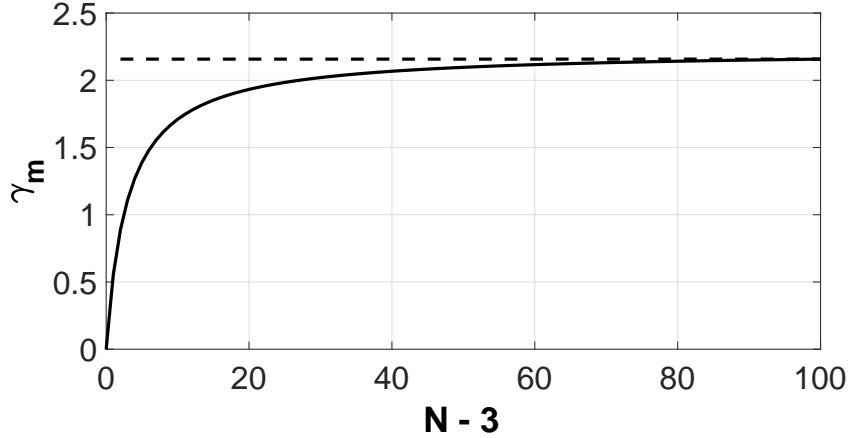
Fig. 7.7 0-gain γ_m of $\Delta_m = \Sigma_N - \Sigma_3$ for $0 \leq N - 3 \leq 100$ and rate 0.05.

flexibility of the framework in systems biology for capturing heterogeneous families of perturbations, mimicking classical robust control. We note that the approach is not limited to linear perturbations and can be extended beyond fixed point analysis to study robust oscillations via 2-dominance.

7.6   Chapter summary and concluding remarks

This chapter can be summarized in the following key points:

1. The modified closed loop system, with a nonlinear trafficking model, is robust. More-over, the features and qualitative behavior of the **CLSS** remain preserved. The non-linear saturations that capture finite compartment capacity do not drastically alter the behavior.

2. Varying the timescale of the global controller τ_u has the same effect on performance as varying k_G in the **CLSS** model. In other words, τ_u modulates between the convergence rate and robustness of the model.

3. Dominance theory allowed us to further examine the convergence rate and robustness tradeoff, which was introduced in Chapter 4 using the **CLSS** model. The tradeoff can be decomposed into two regimes. The first one, corresponding to $1-$dominance, nominal regulation with minimal or no oscillations. The second, corresponding to $0-$dominance, is a more aggressive regulation regime and is substantially more energy-intensive.

From a system-theoretic perspective, adding a timescale τ_u to the global controller (7.2) gave it a low-pass filtering characteristic. Decreasing τ_u gradually made this feature fade away, as we showed in Figure 7.3a-7.3c. This means that there is a limit on how rapid cargo production can be before losing stability.

A nonlinear trafficking system causes more delay to take place, due to the saturated trafficking rates $v_f(c - m_i)$. In the **CLSS** model, trafficking rates were constant, and hence, always faster than their nonlinear counterpart ($v_f \geq v_f(c - m_i)$). We assumed that the neuron is capable of varying the rate at which it produces cargo, to explore a potential physiological mechanism to deal with severe delays and long distances. The study reveals that, indeed, a neuron can withstand a substantial variation in the production of cargo.

By varying the time constant of the production dynamics, we modulate the timescale at which synaptic scaling occurs. This was motivated by the fact that, in experiments, synaptic scaling was recorded to take place over timescales of hours to days [61, 87, 97, 152, 68, 9, 81]. Such variations can be attributed to the experiment, or it can be due to the area or neuron type [168]. For instance, plastic changes in cortical cells were observed to happen over days [128, 129], unlike those in the hippocampus that change much more rapidly [112, 95]. Here, we showed that the toy neuron model shown in Figure 7.1 is generously robust to variations in τ_u. From a computational perspective, the huge recorded variation in the scaling timescale is reasonable considering the variation in neuron morphology and size.

In the next chapter, we explore the effect of adopting another layer of regulation. This layer is structural, and involves geometrical activity-dependent changes in the neuron.

7.7   Proof of Theorem 6

We prove the stability of the closed loop system (7.1)-(7.5) by singular perturbation arguments, specifically invoking Theorem 2. To use this theorem, we prove the exponential stability of the equilibrium of the so-called boundary layer, or fast system. This is constructed from (7.1),(7.3). Furthermore we prove the exponential stability of the equilibrium of the so-called reduced system, constructed from (7.2)-(7.5), by relaxing the fast system at steady state. Part 1 and Part 2 below show that the fast system and the reduced system are both exponentially contractive systems, which entail exponential stability of their respective equilibria. In particular, the fast system is contractive for any time constant $\tau_u > 0$, provided that τ_u is sufficiently large. Thus, stability of the closed loop follows from Theorem 2, under the assumption of sufficient time-scale separation $\tau_u \gg 1$.

Part 1: contraction / stability of the fast system

First we multiply equations (7.1)-(7.3) by $\varepsilon = \frac{1}{\tau_u}$. We start by proving the stability of the fast system (7.1),(7.3). The time derivative in the equations below refers to the scaled time $\tilde{t} = \frac{t}{\tau_u}$. In the fast timescale, the slow variable u is considered as constant. The linearized dynamics of the time-scaled fast system (7.1),(7.3) reads

$$\varepsilon \delta \dot{m} = \frac{\partial f}{\partial m} \delta m \tag{7.10}$$

$$\varepsilon \delta \dot{g} = \frac{1}{\tau_g} S \delta m - \frac{1}{\tau_g} \Omega_g \delta g$$

where $f(m,u)$ is the right-hand side of (7.1), $S = \mathrm{diag}\{s_i\}$, $\Omega_g = \mathrm{diag}\{\omega_g\}$, $m = [m_0, \ldots, m_n]^T$, $g = [g_1, \ldots, g_n]^T$ and $g_{avg} = \frac{1}{n} \sum_i^n g_i = \frac{\mathbf{1}^T g}{n}$, where $\mathbf{1}$ is a vector of ones.

We need to show that (7.10) is a contracting system, which implies the existence of a globally exponentially stable equilibrium when the contracting distance is a norm. We first note that $\frac{\partial f}{\partial m}^T + \frac{\partial f}{\partial m} \leq -2\omega_m I < 0$. Take the differential Lyapunov function $V = \frac{\rho_m}{2} \delta m^T \delta m + \frac{1}{2} \delta g^T \delta g$, where the coefficient $\rho_m > 0$ will be defined later. Its time derivative reads

$$\dot{V} = \dot{V}_m + \dot{V}_g \tag{7.11}$$

where

$$\dot{V}_m = \frac{\rho_m}{2} \left(\left[\frac{\partial f}{\partial m} \delta m \right]^T \delta m + \delta m^T \left[\frac{\partial f}{\partial m} \delta m \right] \right)$$
$$< -\rho_m \omega_m \delta m^T \delta m \delta m \,,$$

and

$$\dot{V}_g = \frac{1}{\tau_g} S \delta m^T \delta g - \frac{1}{\tau_g} \Omega_g \delta g^T \delta g.$$

Therefore, (7.11) satisfies

$$\dot{V} < -\rho_m \omega_m \delta m^T \delta m + S \delta m^T \delta g - \Omega_g \delta g^T \delta g \tag{7.12}$$
$$< -\rho_m |\omega_m| |\delta m|^2 + \frac{1}{\tau_g} |S| |\delta m| |\delta g| - \frac{1}{\tau_g} \lambda_{min}(\Omega_g) |\delta g|^2$$

The right-hand side of (7.12) is bounded by

$$\begin{bmatrix} |\delta m| \\ |\delta g| \end{bmatrix}^T \underbrace{\begin{bmatrix} -\rho_m|\omega_m| & \frac{1}{2\tau_g}|S| \\ \frac{1}{2\tau_g}|S| & -\frac{1}{\tau_g}\rho_g\lambda_{min}(\Omega_g) \end{bmatrix}}_{-Q} \begin{bmatrix} |\delta m| \\ |\delta g| \end{bmatrix}.$$

Next we show that $Q > 0$, using the Sylvester criterion. This guarantees contraction, therefore global exponential stability of the fast system equilibrium. We start by finding conditions under which the leading principal minors of

$$\begin{bmatrix} \rho_m|\omega_m| & -\frac{1}{2\tau_g}|S| \\ -\frac{1}{2\tau_g}|S| & \frac{1}{\tau_g}\lambda_{min}(\Omega_g) \end{bmatrix} \tag{7.13}$$

are positive. We will use the following facts: $|\omega_m| = \omega_m$, $|S| = s$, $\lambda_{min}(\Omega_g) = \omega_g$.

The first principal minor must satisfy $\rho_m\omega_m > 0$, which is true. The second principal minor must satisfy

$$\frac{1}{\tau_g}\rho_m\omega_m\omega_g - \frac{1}{4\tau_g^2}s^2 > 0. \tag{7.14}$$

In order for the above inequality to hold, we need the left-hand side to be positive and larger than the right hand side. So, (7.14) holds if we select

1. $\rho_m > \frac{s^2}{4\omega_m\omega_g\tau_g^2}$.

2. $\tau_u > 0$ is sufficiently large.

Under these conditions, $\dot{V} \leq -\bar{\lambda}V$ for some $\bar{\lambda} > 0$.

The exponential decay of the differential Lyapunov function guarantees global incremental exponential stability of the fast system [57, Theorem 1]. This implies global exponential stability of the equilibrium of the fast system.

Part 2: contraction / stability of the reduced system

We study the stability of the reduced system given by (7.2) for e computed from the fast system at steady state. Thus, as a first step, we study the monotonicity properties of the static relationship between e and u, denoted by $e = r(u)$.

Define $M := \sum\limits_{i=1}^{n} m_i$ and $G := \sum\limits_{i=1}^{n} g_i$. At steady state, $\dot{m}_0 = 0$, $\dot{M} = 0$, $\dot{G} = 0$, we have

$$
\begin{cases}
0 = u - m_0 \left(\dfrac{L}{n} - pM \right) - \omega_m m_0 \\[2ex]
0 = m_0 \left(\dfrac{L}{n} - pM \right) - \omega_m M \\[2ex]
0 = sM - \omega_g G
\end{cases}
\tag{7.15}
$$

where we have written m_1 at steady state as $m_1 = pM$ with $0 < p < 1$. For simplicity, we use x to denote the vector $x = [m_0; M; G]^T$, and $R(x, u)$ to denote the right-hand side of (7.15).

The monotonicity of the static relationship $e = r(u)$ can be determined from the equation $R(x, u) = 0$. For instance, $\frac{\partial R}{\partial x} \delta x + \frac{\partial R}{\partial u} \delta u = 0$, which gives

$$
\delta x = - \left[\frac{\partial R}{\partial x} \right]^{-1} \frac{\partial R}{\partial u} \delta u .
\tag{7.16}
$$

We observe that the inverse $\left[\frac{\partial R}{\partial x} \right]^{-1}$ must exists since the fast system is contractive. Furthermore, the error $e_G = [Ca^{+2}]_{target} - h(G/n) =: E(x)$. Thus, we get

$$
\delta e_G = \frac{\partial E}{\partial x} \delta x = \underbrace{- \frac{\partial E}{\partial x} \left[\frac{\partial R}{\partial x} \right]^{-1} \frac{\partial R}{\partial u}}_{\partial r / \partial u} \delta u .
\tag{7.17}
$$

We observe that $\frac{\partial E}{\partial x} = [0 \, 0 \, \frac{\partial E}{\partial x_3}]$ and that $\frac{\partial E}{\partial x_3} < 0$. Computing explicitly (7.17) we get

$$
\frac{\partial r}{\partial u} = \frac{\frac{\partial E}{\partial x_3} s(L - npM)}{\omega_m \omega_g (L - npM + n\omega_m + npm_0)} < 0,
\tag{7.18}
$$

where the inequality follows from

$$
npM = \frac{L}{c} \times \frac{m_1}{M} \times M = \frac{m_1}{c} L < L .
$$

Thus, from (7.18) , we get $\frac{\partial r}{\partial u} < 0$ for any $u > 0$.

From the argument above we conclude that $e_G = r(u)$ is strictly decreasing. This feature can be used to show contraction of the reduced system. The reduced system and its

linearization read

$$\dot{u} = k_G r(u) - \omega_u u + \phi_{\ell b}(u, \bar{\phi})$$

$$\delta \dot{u} = k_G \underbrace{\frac{\partial r}{\partial u}}_{<0} \delta u - \omega_u \delta u + \underbrace{\frac{\partial}{\partial u} \phi_{\ell b}(u, \bar{\phi})}_{\simeq 0, \text{by assumption}} \delta u \ . \tag{7.19}$$

(7.19) is a contractive dynamics, thus the equilibrium of the reduced system is globally exponentially stable.

Chapter 8

Synaptic scaling in adaptive morphologies: an intrinsic robustness

> *"Where attention goes, neural firing flows, and neural connection grows."*
>
> Daniel J. Siegel, *Aware: The Science and Practice of Presence*

In this chapter we consider another layer of regulation, in addition to synaptic scaling. Here, we study activity-dependent growth, which is also of a homeostatic nature. We explore the implications on performance when two homeostatic mechanisms coexist.

8.1   Introduction and motivation

In Section 7.5.2 we studied growth as a special case of robustness against static uncertainties. The case study ignored the fact that growth in neurons is an activity-dependent physiological process. Neurons undergo a number of structural changes, including growth, that occur in response to various inputs and with the goal of maintaining activity around a set-point. Structural plasticity encompasses morphological changes, such as outgrowth/shrinking of dendrites or axons, dendritic branching, and formations/elimination of synapses [27]. Such changes in the neuron's structural properties happen in response to variations in the electrical activity [107], similar to synaptic scaling. These changes are particularly prevalent during development as neurites grow and as connections first form. Thus, alterations to this process can profoundly and permanently affect the function of a mature network [59, 153].

To understand the role of activity-dependent growth, we modify the model of Chapter 7, namely Equations (7.1)-(7.5). We then take advantage of the "static" growth study (7.9) and implement in the new model to capture dynamic changes that will occur to the compartments, mimicking growth.
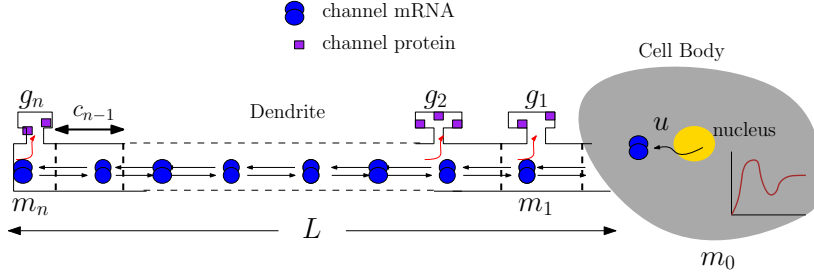
Fig. 8.1 Recalling the abstract neuron model from Chapter 7, and emphasizing the neuron length L and compartment size c_i.

8.2   Modifications to the closed loop model

8.2.1   A scaled nonlinear compartmental model for dendritic trafficking

We revisit the neuron model presented in the previous chapter, and emphasize the new dynamical parameters: L and c_i, shown in Figure 8.1. The first modification to the model is applied to the trafficking system (7.1). The goal of this modification is to exclude growth process effects on the trafficking rates. The model reads

$$\dot{m}_0 = u - m_0(c - m_1) - \omega_m m_0$$
$$\dot{m}_1 = m_0(c - m_1) + \frac{v_b}{c^2}(c - m_1)m_2 - \frac{v_f}{c^2}(c - m_2)m_1$$
$$\quad - \omega_m m_1$$
$$\dot{m}_i = -\frac{v_f}{c^2}(c - m_{i+1})m_i + \frac{v_b}{c^2}(c - m_i)m_{i+1}$$
$$\quad + \frac{v_f}{c^2}(c - m_i)m_{i-1} - \frac{v_b}{c^2}(c - m_{i-1})m_i - \omega_m m_i$$
$$\dot{m}_n = \frac{v_f}{c^2}(c - m_n)m_{n-1} - \frac{v_b}{c^2}(c - m_{n-1})m_n - \omega_m m_n. \tag{8.1}$$

As before, m_0 represents the mRNA concentration in the soma, $m_i \in [0, c]$ represents mRNA concentration in dendritic compartment $i \geq 1$, v_f and v_b are the forward and backward trans-

port rates, respectively, ω_m is the mRNA degradation rate, u represents mRNA production, and c represents the finite capacity of a single compartment, to model crowding.

8.2.2 Structural plasticity as growth dynamics

Structural plasticity involves multiple morphological changes that happen in response to perturbations in electrphysiological activity [27]. Morphological changes include dendritic/axonal length variations (during development), synapse formation and elimination (dendritic spines and axonal boutons), and branching. In our model, such variations are captured by a single length parameter L, describing the average length of a dendritic arbor.
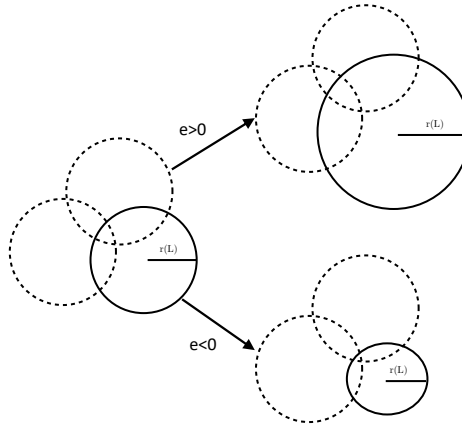
Fig. 8.2 Guided by the mismatch e, as L increases (decreases), the neuron's probability to form new connections increases (decreases), which is done by spatially expanding (shrinking). $r(L)$ denotes the radius of connectivity, which is a function of L.

We model structural plasticity as a growth process that is directly coupled to the neurons's average activity, captured by calcium concentration $[Ca^{+2}]$. The basic idea is that short dendrites have fewer connections, thus a reduced electrical activity. Likewise, long dendrites potentially make more connections, thus enjoying a stronger electrical activity. In this sense, L can also be considered as an abstract indicator of the connectivity of the neuron. Then, a feedback mechanism adjusts L to achieve homeostasis in a way that is not at all dissimilar from synaptic scaling [157, 89, 145]: above set-point ($e < 0$), L must shrink to reduce the number of synapses (pruning) / weakening existing connections, thus reducing the overall electrical activity; conversely, below set point ($e > 0$), L must increase for the neuron to reach out to other neurons / strengthening existing connections, ultimately increasing the

level of electrical activity. This is schematically captured in Figure 8.2. Each neuron in the network is represented by circular neuritic field [157], where the radius is changing in an activity-dependent manner (in this case the radius r is a function of L). A connection and its strength is reflected by the size of the overlapping area. In this way, the more connections the cell receives, the stronger the average electrical activity will be, and vice versa.

We remark that our assumption about the relationship between the neuronal activity and L is not about the intrinsic membrane properties but rather about the neuron connectivity. The total excitatory input is assumed to scale with the size of the dendritic arbour. This is a reasonable and standard assumption [157]. One might argue that inhibitory connections develop in similar proportion, canceling out the increase in excitatory connectivity. In a mature network this may be the case, however during development, as networks are growing, excitatory connections form initially and inhibitory neurotransmitters undergo a late developmental switch [15] from being initially excitatory to inhibitory after many of the connections have formed.

Based on these physiological observations, we model the growth dynamics using the nonlinear first order process

$$\tau \dot{L} = \phi(e_G) - \omega_L L, \qquad c = \frac{L}{n} \qquad\qquad (8.2)$$

where $\tau \gg 0$ is a slow time constant reflecting the slow dynamics of growth[1], and ω_L is the degradation or disassembly rate of the molecules that are responsible for synthesis of the new dendritic components, such as tubulin. The function ϕ, $\phi(0) = 0$, is a monotonically increasing function in the error e_G (see Figure 8.3).

If we interpret L as a connectivity indicator, the slope ϕ' captures the density of the surrounding neurons or richness of the network; a steeper ϕ means there are more potential connections to be made or removed, for the same amount of growth. We emphasize that growth in (8.2) eventually corresponds to a simple variation of capacity, which also affects the forward and backward transport rates in (8.1).

The rest of model is identical to that of Chapter 7. For readability, we list the remaining model components.

---

[1] In biological neurons, growth rates are on the order of days or weeks [156, 133], while active motor-assisted transport is of the order of hours [161]. For example, in *C. elegans*, it was found that they grow at an average rate of $0.001 \mu m/s$, while active transport rates are $\mathcal{O}(1 \mu m/s)$ [24, 143].
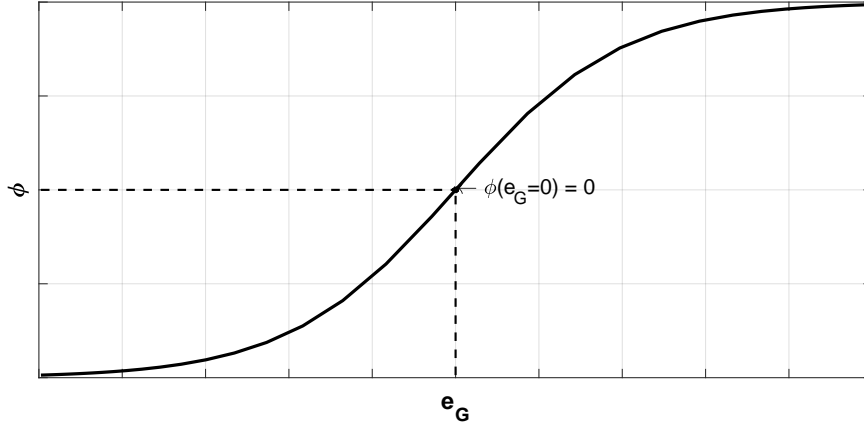
Fig. 8.3 An example of the monotone increasing function ϕ. The graph corresponds to (8.8).

$$\text{Protein dynamics:} \quad \dot{g}_i = sm_i - \omega_g g_i \qquad (8.3)$$

$$\text{Readout map:} \quad g_{avg} = \frac{1}{n} \sum_{i=1}^{n} g_i \qquad (8.4)$$

$$\text{Membrane potential:} \quad V = \frac{g_{avg} E_g + g_{leak} E_{leak}}{g_{leak} + g_{avg}} \qquad (8.5)$$

$$\text{Calcium signal:} \quad [Ca^{+2}] = \frac{\alpha}{1 + \exp(-V/\beta)} \qquad (8.6)$$

$$\text{Cargo production:} \quad \dot{u} = k_G e_G - \omega_u u \qquad (8.7)$$

$$\text{Error:} \quad e_G = [Ca^{+2}]_{target} - [Ca^{+2}].$$

Both the modified synaptic scaling system (8.1),(8.3)-(8.7) and growth dynamics (8.2) aim to achieve the same objective: regulating the neuron's average activity around an (approximate) set-point. The difference is that synaptic scaling occur at a fast timescale and it works by modulating (globally) the number of ion channels g_i in the system. In contrast, growth occurs at a slow timescale and it changes compartments' capacities to modulate the maximum allowable g_i in each synapse. Figure 8.4 provides an illustration of the complete closed loop comprising the two processes.

Fig. 8.4 A block diagram showing the complete closed loop of both synaptic scaling and activity-dependent growth.

8.3   Homeostasis by fast synaptic scaling and slow growth adaptation

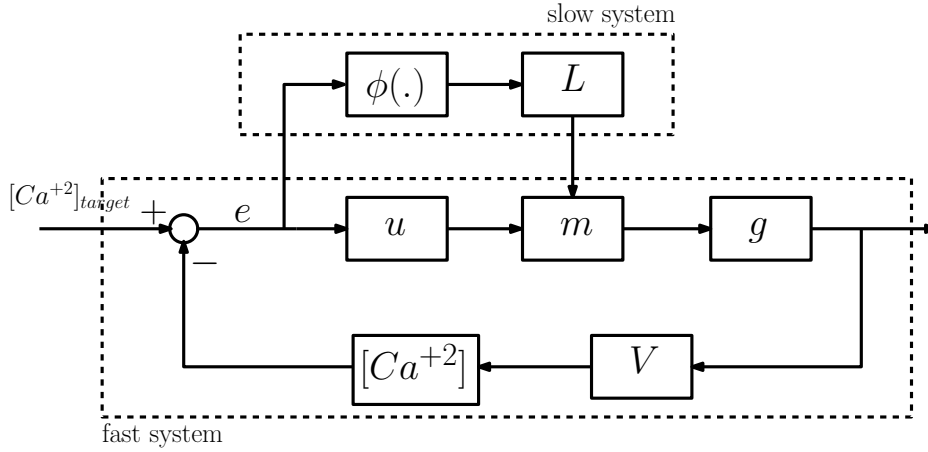For any fixed dendritic length L, synaptic scaling (8.1),(8.3)-(8.7) is a stable process if the feedback gain k_G is sufficiently small. In fact, as we have seen in previous chapters, the aggressiveness of the control action is fundamentally limited by the presence of transport. Growth adaptation is also a stable process, naturally occurring at a slower timescale than synaptic scaling. Thus, by time-scale separation, the combination of synaptic scaling and growth adaptation leads to a stable closed loop system (8.1)-(8.7), for a sufficiently slow growth time constant τ.

Theorem 7 *Under Assumption 1, there exists a maximal feedback gain $\bar{k}_G > 0$ and a minimal time constant $\bar{\tau} > 0$ such that, for every $0 \le k_G < \bar{k}_G$, $\tau > \bar{\tau}$, and $[Ca^{2+}]_{target}$ the closed loop (8.1)-(8.2) has a globally exponentially stable equilibrium.*

Taking advantage of the theoretical result in Theorem 7, we study the system's response under different biologically relevant situations, to better understand the interplay between synaptic scaling and growth dynamics. With this aim, we set $\phi(e)$ in (8.2) as in [157]

$$\phi(e_G) = 1 - \frac{2}{1 + \exp(e_G/\eta)}, \tag{8.8}$$

and we simulate the system for the parameters in Table 8.1.

The first observation is that *growth adaptation guarantees homeostasis even if synaptic scaling is insufficient*. First of all, note that the averaged sum of ion-channel proteins is

Table 8.1 Nominal Parameter Values

$v_f = 1\ \mu m s^{-1}$	$v_b = 0.5\ \mu m s^{-1}$	$\omega_m = 0.1\ s^{-1}$	$n = 2$
$E_{leak} = -50\ mV$	$E_g = 20\ mV$	$\omega_L = 0.1\ s^{-1}$	$\eta = 0.1$
$\beta = 1$	$\alpha = 1$	$\omega_g = 0.1\ s^{-1}$	$\tau = 10^5$
$[Ca^{2+}]_{target} = 0.5\ \mu M$	$g_{leak} = 0.25\ \mu S$	$\omega_u = 10^{-5}\ s^{-1}$	

limited by

$$g_{avg} = \frac{1}{n} \sum_{i=1}^{n} g_i = \frac{s}{n\omega_g} \sum_{i=1}^{n} m_i \leq \frac{s}{n\omega_g} nc = \frac{s}{\omega_g} c \ .$$

Thus, regulation is feasible

$$0 \simeq e_G = [\text{Ca}^{+2}]_{\text{target}} - [\text{Ca}^{+2}] = [\text{Ca}^{+2}]_{\text{target}} - h(g_{avg}) \ ,$$

only if the desired steady state satisfies

$$[\text{Ca}^{+2}]_{\text{target}} \leq h\left(\frac{s}{\omega_g} c\right) \ . \tag{8.9}$$

Inequality (8.9) fundamentally relates the calcium target / the desired level neural activity to the morphological parameter $c = L/n$. It shows that, without growth adaptation, high levels of neural activity ($[\text{Ca}^{+2}]_{\text{target}}$ large) cannot be attained in closed loop because of the finite capacity of cargo transport. However, taking advantage of growth adaptation, the neuron can develop its morphology to reach the desired calcium target.

These two cases are illustrated through simulation, within a comparison between synaptic scaling without growth adaptation (8.1),(8.3)-(8.7), and synaptic scaling with growth adaptation (8.1)-(8.7). We recall that the stability of synaptic scaling without growth adaptation (8.1)-(8.7) is guaranteed by Theorem 6. Results are summarized in Figure 8.5. Left and right graphs shows the calcium $[\text{Ca}^{+2}]$ trajectory and the length L trajectory, respectively. Dashed lines correspond to synaptic scaling without adaptation, while continuous lines correspond to the growth adaptation case. Figure 8.5 shows the case in which $[\text{Ca}^{+2}]_{\text{target}} = 0.5$ is not compatible with the the initial capacity $c = L/n = 0.1/n$ in the sense of (8.9). The dashed line shows that synaptic scaling without growth adaptation is stable but far from target. This is not the case of synaptic scaling with growth adaptation, whose calcium trajectory asymptotically converges to $[\text{Ca}^{+2}]_{\text{target}}$, taking advantage of the increased average length L, thus of larger capacity c.

Considering L as a connectivity parameter, the biological interpretation is that the neuron is below its target activity level and therefore attempts to increase its activity by forming new

synapses to form new connections, or increasing spines' sizes to amplify synaptic strength of existing connections. Likewise, considering L as a morphological parameter, the neuron increases the size of its spines to allow more ion channels to flow to the synapse, which also increases the electrical activity.
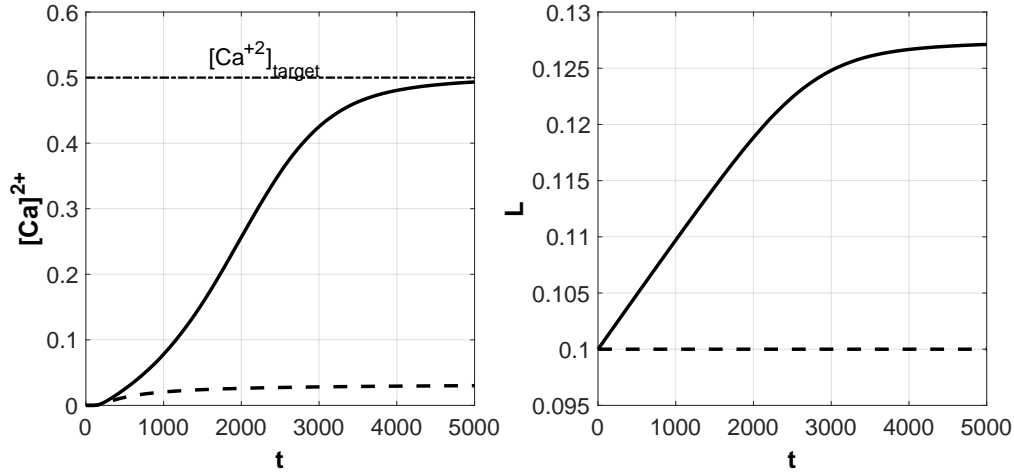

Fig. 8.5 Average activity and length for the synaptic scaling model (8.1),(8.3)-(8.7) (dashed) and synaptic scaling model with growth dynamics (8.1)-(8.7) (solid). $k_G = 0.001$ and $L_0 = 0.1$.

The second observation, derived from simulations, is that *growth adaptation may compensate for pathological oscillations, enabling more aggressive synaptic scaling*. Aggressive feedback gains k_G may lead to pathological oscillations in synaptic scaling [5], as shown in Figure 8.6a. However, these oscillations are dampened through growth adaptation, as shown in Figure 8.6b, reaching the desired set-point. The intuition is that (8.2) is essentially a low pass filter therefore it filters calcium oscillations, extracting the oscillations bias. The overall growth adaptation is thus driven by this bias. When the bias is above the desired calcium target, as in Figure 8.6, the average length will reduce, stabilizing the oscillations. The biological interpretation is that synapses reduces their size, by reducing spine's size or reducing the number of slots on its membrane, when their average electrical activity is irregular (oscillatory).

The above observations, along with the growth process (8.2), establish how structural plasticity regulates neuron activity. Synaptic scaling, as seen in the previous chapters, directly alters the concentration of functional cargo in synapses, hence effecting their densities. On the other hand, structural plasticity, such as (8.2), influences the synapses' properties, like their

spine sizes, which then effect the concentration of functional cargo in synapses. Therefore, structural plasticity mechanisms indirectly affect synaptic densities.
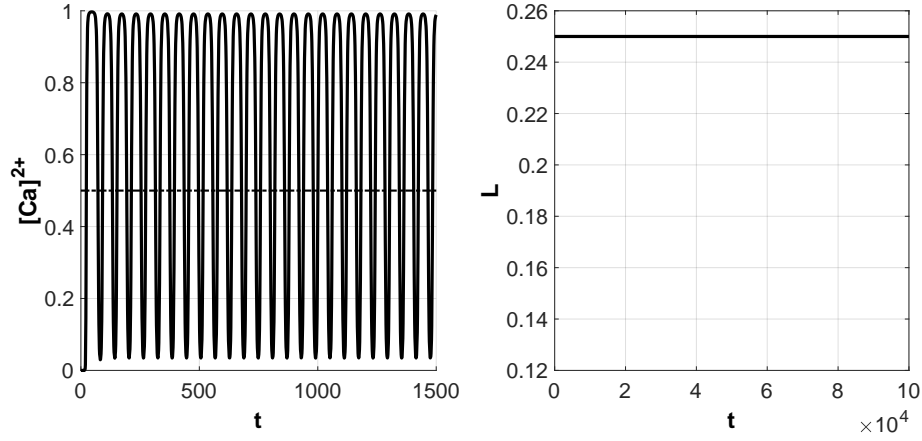
(a) Synaptic scaling model (8.1)-(8.7)
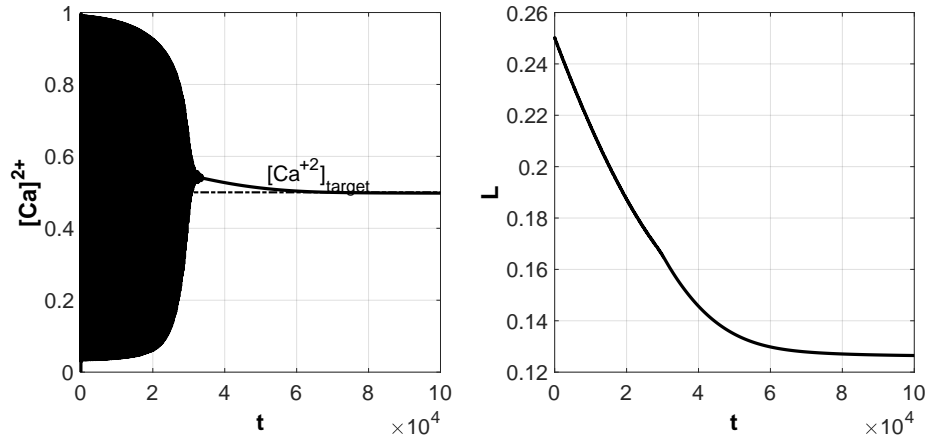
(b) Synaptic scaling model with growth dynamics (8.1)-(8.2)

Fig. 8.6 grow adaptation (8.2) increases the maximum allowable $\bar{k}_u$. Simulations were done with $k_G = 0.01$ and $L_0 = 0.25$. For readability, the calcium trajectory in the left graph of Figure 8.6a is represented on the reduced domain $0 \leq t \leq 1500$.

The last observation is that *inadequate timescale separation leads to fragility*. Theorem 7 guarantees closed loop stability under the strong hypothesis of time scale separation between synaptic scaling and growth adaptation. The simulations in Figure 8.7 shows that time scale separation is actually needed for stability. As τ decreases the system stability becomes more fragile. Reducing τ produces damped oscillations and a further reduction eventually leads to sustained oscillations, for smaller values of τ.
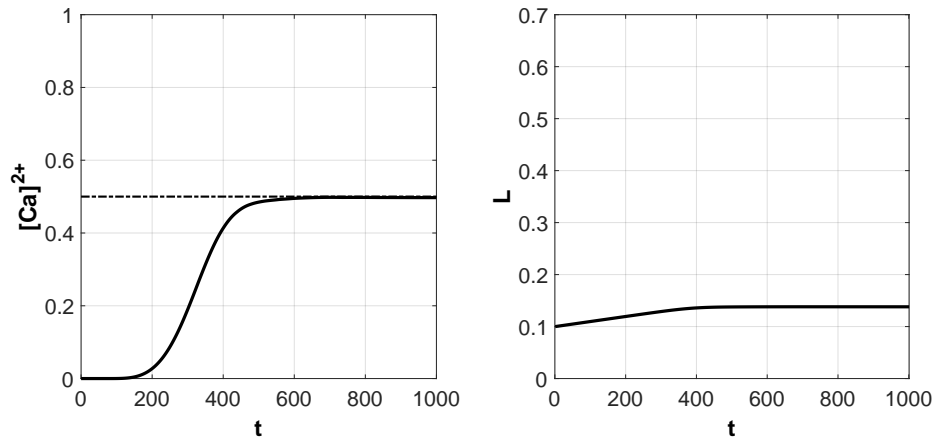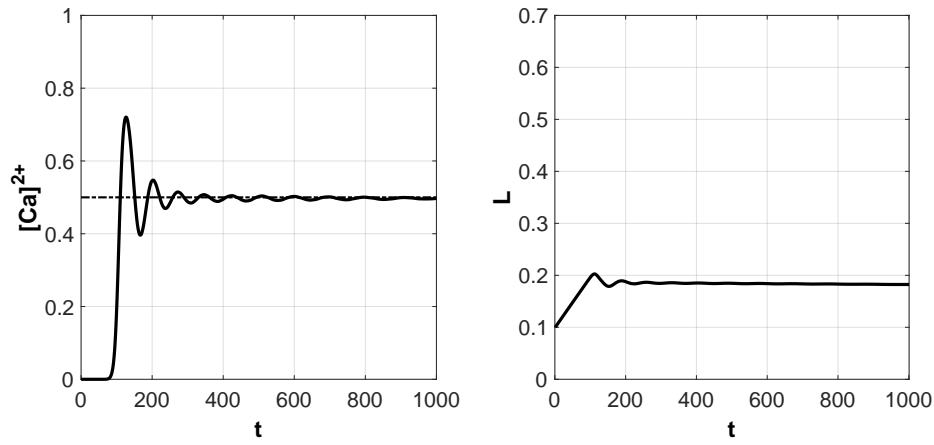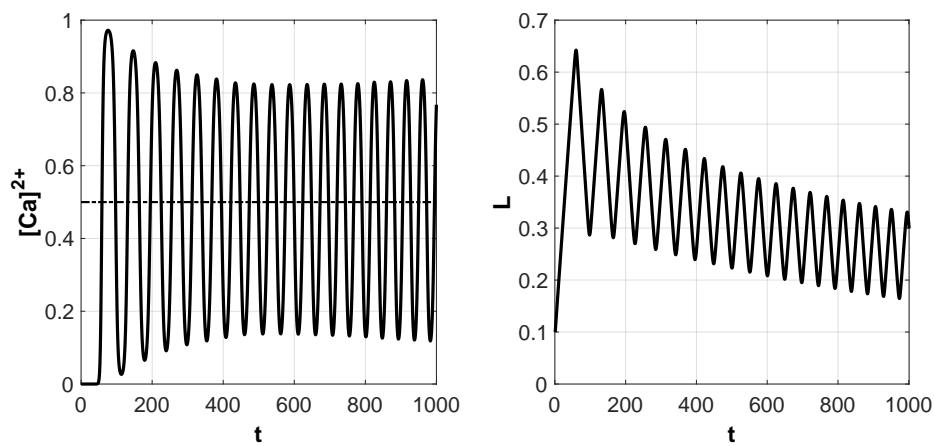
(a) $\tau = 10^4$.

(b) $\tau = 10^3$.

(c) $\tau = 10^2$.

Fig. 8.7 Inadequate timescale separation introduces fragility.

8.4   Chapter summary and concluding remarks

This chapter can be summarized in the following key points:

1. Synaptic scaling and activity-dependent growth can coexists where both mechanisms promote homeostasis of neuron activity. This was shown in Theorem 7.

2. An activity-dependent growth process improves the performance, by enhancing efficacy in individual synapses (Figure 8.5), and pushing the maximum allowable feedback gain $\bar{k}_G$ (Figure 8.6).

In this chapter we studied two distinct homeostatic mechanisms: synaptic scaling and structural plasticity by formulating a model of nonlinear dendritic trafficking with growth adaptation. We showed how the interplay between the fast transport and slow growth dynamics provides the mean to improve the overall performance in two ways. The first way was that growth adaptation guarantees homeostasis when synaptic scaling is insufficient. The second way was that growth adaptation compensate for pathological oscillations, allowing more robustness to tolerate aggressive synaptic scaling.

In connection to the **CLSS** model, activity-dependent growth can improve the neuron's performance. Specifically, a dynamic compartment size $c(t)$ can potentially improve the tradeoffs in Chapter 4 (Figure 4.13). The improvement is manifested through the increase of the upper bound on the feedback gain $\bar{k}_G$. We recall that k_G modulated between the robustness of the system and its convergence rate. The observations in this chapter also agrees with the observation made in Chapters 4-5,7 regarding the effect of neuron's size on performance: smaller neurons are more robust.

It is nontrivial to make a prediction on how the accuracy attribute of performance is affected in the new model. The difficulty arises from the modifications applied to the **CLSS** model; since, in the new model (8.1)-(8.7), information about the local activity is not explicitly expressed.

The principles and machinery applied here can be used to study more complex aspects of neurons' morphological development. These developments include initiation and differentiation, elongation, branching and shape formation [65]. Previous studies did not consider the effect feedback and regulation [108, 163, 76]. We believe that the framework adapted here could be adopted to study and verify a number of significant physiological observations surrounding neuron development.

8.5   Proof of theorem 7

We prove the stability of the closed loop system (8.1)-(8.7) by singular perturbation arguments, specifically invoking Theorem 2. To use this theorem, we prove the exponential stability of the equilibrium of the so-called boundary layer, or fast system. This is constructed from (8.1),(8.3)-(8.7). Furthermore we prove the exponential stability of the equilibrium of the so-called reduced system, constructed from (8.2), by relaxing the fast system at steady state. Part 1 and Part 2 below show that the fast system and the reduced system are both exponentially contractive systems, which entail exponential stability of their respective equilibria. In particular, the fast system is contractive for any feedback gain $0 \leq k_G < \bar{k}_G$, provided that $\bar{k}_G$ is sufficiently small. Thus, stability of the closed loop (8.1)-(8.7) follows from Theorem 2, under the assumption of sufficient time-scale separation $\tau \gg 1$.

Part 1: contraction / stability of the fast system

First we multiply equations (8.1)-(8.7) by $\varepsilon = \frac{1}{\tau}$. We start by proving the stability of the fast system (8.1),(8.3)-(8.7). The time derivative in the equations below refers to the scaled time $\tilde{t} = \frac{t}{\tau}$. In the fast timescale, the slow variable L is considered as constant. The linearized dynamics of the time-scaled fast system (8.1),(8.3)-(8.7) reads

$$\varepsilon \delta \dot{m} = \frac{\partial f}{\partial m} \delta m + B \delta u \tag{8.10}$$

$$\varepsilon \delta \dot{g} = S \delta m - \Omega_g \delta g$$

$$\varepsilon \delta \dot{u} = -k_G \frac{\partial h}{\partial g} \left(\frac{\mathbf{1}^T g}{n} \right) \frac{\mathbf{1}^T}{n} \delta g - \omega_u \delta u.$$

where $f(m, L)$ is the right-hand side of (8.1), $S = \text{diag}\{s\}$, $\Omega_g = \text{diag}\{\omega_g\}$, $m = [m_0, \ldots, m_n]^T$, $g = [g_1, \ldots, g_n]^T$ and $g_{avg} = \frac{1}{n} \sum_i^n g_i = \frac{\mathbf{1}^T g}{n}$, where $\mathbf{1}$ is a vector of ones.

We need to show that (8.10) is a contracting system, which implies the existence of a globally exponentially stable equilibrium when the contracting distance is a norm. We first note that $\frac{\partial f}{\partial m}^T + \frac{\partial f}{\partial m} \leq -2\omega_m I < 0$. Take the differential Lyapunov function $V = \frac{\rho_m}{2} \delta m^T \delta m + \frac{\rho_g}{2} \delta g^T \delta g + \frac{1}{2} \delta u^T \delta u$. The coefficients $\rho_m > 0$ and $\rho_g > 0$ will be defined later. Its time derivative reads

$$\dot{V} = \dot{V}_m + \dot{V}_g + \dot{V}_u \tag{8.11}$$

where

$$\dot{V}_m = \frac{\rho_m}{2}\left(\left[\frac{\partial f}{\partial m}\delta m + B\delta u\right]^T \delta m + \delta m^T\left[\frac{\partial f}{\partial m}\delta m + B\delta u\right]\right)$$
$$< -\rho_m \omega_m \delta m^T \delta m + \rho_m B\delta u^T \delta m \ ,$$

$$\dot{V}_g = \rho_g S\delta m^T \delta g - \rho_g \Omega_g \delta g^T \delta g,$$

and

$$\dot{V}_u = -k_G \frac{\partial h}{\partial g}\left(\frac{\mathbf{1}^T g}{n}\right)\frac{\mathbf{1}^T}{n}\delta g\delta u - \omega_u \delta u^T \delta u.$$

Therefore, (8.11) satisfies

$$\dot{V} < -\rho_m \omega_m \delta m^T \delta m + \rho_m B\delta u^T \delta m + \rho_g S\delta m^T \delta g \tag{8.12}$$
$$- \rho_g \Omega_g \delta g^T \delta g - k_G \frac{\partial h}{\partial g}\left(\frac{\mathbf{1}^T g}{n}\right)\frac{\mathbf{1}^T}{n}\delta g\delta u - \omega_u \delta u^T \delta u$$
$$< -\rho_m|\omega_m||\delta m|^2 + \rho_m|B||\delta u||\delta m| + \rho_g|S||\delta m||\delta g|$$
$$- \rho_g \lambda_{min}(\Omega_g)|\delta g|^2 + k_G\left|\frac{\partial h}{\partial g}\left(\frac{\mathbf{1}^T g}{n}\right)\frac{\mathbf{1}^T}{n}\right||\delta g||\delta u| - \omega_u|\delta u|^2.$$

The right-hand side of (8.12) is bounded by

$$\begin{bmatrix}|\delta m|\\|\delta g|\\|\delta u|\end{bmatrix}^T \underbrace{\begin{bmatrix} -\rho_m|\omega_m| & \frac{1}{2}\rho_g|S| & \frac{1}{2}\rho_m|B| \\ \frac{1}{2}\rho_g|S| & -\rho_g\lambda_{min}(\Omega_g) & \frac{1}{2}k_G\left|\frac{\partial h}{\partial g}\left(\frac{\mathbf{1}^T g}{n}\right)\frac{\mathbf{1}^T}{n}\right| \\ \frac{1}{2}\rho_m|B| & \frac{1}{2}k_G\left|\frac{\partial h}{\partial g}\left(\frac{\mathbf{1}^T g}{n}\right)\frac{\mathbf{1}^T}{n}\right| & -\omega_u \end{bmatrix}}_{-Q}\begin{bmatrix}|\delta m|\\|\delta g|\\|\delta u|\end{bmatrix}.$$

Next we show that $Q > 0$, using the Sylvester criterion. This guarantees contraction, therefore global exponential stability of the fast system equilibrium We start by finding conditions under which the leading principal minors of

$$\begin{bmatrix} \rho_m|\omega_m| & -\frac{1}{2}\rho_g|S| & -\frac{1}{2}\rho_m|B| \\ -\frac{1}{2}\rho_g|S| & \rho_g\lambda_{min}(\Omega_g) & -\frac{1}{2}k_G\left|\frac{\partial h}{\partial g}\left(\frac{\mathbf{1}^T g}{n}\right)\frac{\mathbf{1}^T}{n}\right| \\ -\frac{1}{2}\rho_m|B| & -\frac{1}{2}k_G\left|\frac{\partial h}{\partial g}\left(\frac{\mathbf{1}^T g}{n}\right)\frac{\mathbf{1}^T}{n}\right| & \omega_u \end{bmatrix} \tag{8.13}$$

are positive. We will use the following facts: $|\omega_m| = \omega_m$, $|S| = s$, $\lambda_{min}(\Omega_g) = \omega_g$, $|B| = 1$.

The first principal minor must satisfy $\rho_m \omega_m > 0$, which is true. The second principal minor must satisfy

$$\rho_m \rho_g \omega_m \omega_g - \frac{1}{4}\rho_g^2 s^2 > 0. \tag{8.14}$$

The last principal minor must satisfy

$$\rho_m \rho_g \omega_g \omega_g \omega_u - \frac{1}{4}\rho_g \rho_m s k_G \left| \frac{\partial h}{\partial g}\left(\frac{\mathbf{1}^T g}{n}\right)\frac{\mathbf{1}^T}{n} \right| +$$

$$-\frac{1}{4}\rho_m^2 \rho_g \omega_g - \frac{1}{4}\rho_m \omega_m k_u^2 \left| \frac{\partial h}{\partial g}\left(\frac{\mathbf{1}^T g}{n}\right)\frac{\mathbf{1}^T}{n} \right|^2 - \frac{1}{4}\rho_g^2 s^2 \omega_u > 0$$

which can be re-arranged as

$$\rho_m \rho_g \omega_g \omega_g \omega_u - \frac{1}{4}\rho_g^2 s^2 \omega_u - \frac{1}{4}\rho_m^2 \rho_g \omega_g$$

$$> \frac{k_G \rho_m}{4}\left| \frac{\partial h}{\partial g}\left(\frac{\mathbf{1}^T g}{n}\right)\frac{\mathbf{1}^T}{n} \right| \left(\rho_g s + \omega_m k_G \left| \frac{\partial h}{\partial g}\left(\frac{\mathbf{1}^T g}{n}\right)\frac{\mathbf{1}^T}{n} \right| \right) \tag{8.15}$$

In order for the above inequality to hold, we need the left-hand side to be positive and larger than the right hand side. So, (8.14) and (8.15) hold if we select

1. $\rho_g < \frac{2\rho_m \omega_m \omega_g}{s^2}$.

2. $\rho_m < 2\omega_u \omega_m$.

3. $0 \leq k_G < \bar{k}_G$ is sufficiently small.

Under these conditions, $\dot{V} \leq -\bar{\lambda}V$ for some $\bar{\lambda} > 0$.

The exponential decay of the differential Lyapunov function guarantees global incremental exponential stability of the fast system, [57, Theorem 1]. This implies global exponential stability of the equilibrium of the fast system.

Part 2: contraction / stability of the reduced system

We study the stability of the reduced system given by (8.2) for e computed from the fast system at steady state. Thus, as a first step, we study the monotonicity properties of the static relationship between e and L, denoted by $e = r(L)$.

Define $M := \sum_{i=1}^{n} m_i$ and $G := \sum_{i=1}^{n} g_i$. At steady state, $\dot{m}_0 = 0$, $\dot{M} = 0$, $\dot{G} = 0$, $\dot{u} = 0$, we have

$$
\begin{cases}
0 = u - m_0 \left(\dfrac{L}{n} - pM \right) - \omega_m m_0 \\[2mm]
0 = m_0 \left(\dfrac{L}{n} - pM \right) - \omega_m M \\[2mm]
0 = sM - \omega_g G \\[2mm]
0 = k_G e - \omega_u u \,,
\end{cases}
\tag{8.16}
$$

where we have written m_1 at steady state as $m_1 = pM$ with $0 < p < 1$. For simplicity, we use x to denote the vector $x = [m_0; M; G; u]^T$, and $R(x,L)$ to denote the right-hand side of (8.16).

The monotonicity of the static relationship $e = r(L)$ can be determined from the equation $R(x,L) = 0$. For instance, $\frac{\partial R}{\partial x} \delta x + \frac{\partial R}{\partial L} \delta L = 0$, which gives

$$
\delta x = - \left[\frac{\partial R}{\partial x} \right]^{-1} \frac{\partial R}{\partial L} \delta L \,.
\tag{8.17}
$$

We observe that the inverse $\left[\frac{\partial R}{\partial x} \right]^{-1}$ must exists since the fast system is contractive. Furthermore, the error $e_G = [Ca^{+2}]_{target} - h(G/n) =: E(x)$. Thus, we get

$$
\delta e_G = \frac{\partial E}{\partial x} \delta x = \underbrace{- \frac{\partial E}{\partial x} \left[\frac{\partial R}{\partial x} \right]^{-1} \frac{\partial R}{\partial L}}_{\partial r / \partial L} \delta L \,.
\tag{8.18}
$$

We observe that $\frac{\partial E}{\partial x} = [0 \, 0 \, \frac{\partial E}{\partial x_3} \, 0]$ and that $\frac{\partial E}{\partial x_3} < 0$ (as shown in Figure 8.3-left). Computing explicitly (8.18) we get

$$
\frac{\partial r}{\partial L} = \frac{\mu_1}{\mu_2 \mu_4 + \mu_3} \,,
\tag{8.19}
$$

where

$$
\begin{aligned}
\mu_1 &= s \omega_m \omega_u m_0 \frac{\partial E}{\partial x_3} < 0 \\[2mm]
\mu_2 &= \omega_m \omega_g \omega_u - k_G s \frac{\partial E}{\partial x_3} > 0 \\[2mm]
\mu_3 &= n \omega_m \omega_g \omega_u (\omega_m + m_0 p) > 0 \\[2mm]
\mu_4 &= L - npM > 0 \,.
\end{aligned}
\tag{8.20}
$$

The latter inequality follows from

$$npM = \frac{L}{c} \times \frac{m_1}{M} \times M = \frac{m_1}{c} L < L \ .$$

Thus, from (8.19) and (8.20), we get $\frac{\partial r}{\partial L} < 0$ for any $L > 0$.

From the argument above we conclude that $e_G = r(L)$ is strictly decreasing. This feature can be used to show contraction of the reduced system. The reduced system and its linearization read

$$\dot{L} = \phi(r(L)) - \omega_L L$$

$$\delta\dot{L} = \underbrace{\frac{\partial \phi}{\partial e}}_{>0} \underbrace{\frac{\partial r}{\partial L}}_{<0} \delta L - \omega_L \delta L \ . \tag{8.21}$$

(8.21) is a contractive dynamics, thus the equilibrium of the reduced system is globally exponentially stable.

Chapter 9

Conclusions

9.1 Recap

The dissertation studied homeostatic control of average neuronal activity in single neurons, where we focused on the effects of morphology. The main contributions can be summarized in the following key points:

- *Real neuronal morphology imposes an unavoidable tradeoff on performance.* We have seen how morphology imposes hard limits on the performance of homeostatic synaptic scaling. This is caused by the fact that AMPA receptor trafficking constrains the closed loop system. We have shown that, from an input-output perspective, the cell body "senses" an equivalent line rather than a complex network. Those input-output features inform and constrain the performance tradeoffs, from abstract, simple networks to real, complex morphologies.

  We started in Chapter 3 by developing a biophysical model that captured synthesis, transport, activation/inactivation, and regulation of AMPA receptors. The closed loop system's main goal was to achieve homeostasis of the neuron's average activity. In Section 3.4, we showed that the **CLSS** model exhibits a homeostatic scaling characteristic that is compatible with experimental recordings that studied Hebbian-like plasticity mechanisms, such as LTP/LTD processes.

  In Chapter 4 we inquired three fundamental attributes of neuron performance, namely convergence rate, system's robustness, and accuracy of scaling. We then showed that these three attributes are modulated by the system parameters: k_G, s_{-i}, and k_L, namely the gain of the global feedback, the rate of the activation mechanism, and the gain of the local feedback. Most importantly, we showed how these attributes are intrinsically

connected to one another, in such a way that improving one performance attribute is accompanied by a deteriorating effect on the other two, as shown in Figure 4.13.

In Chapter 5 we stepped away from toy neuron models to study the effects of real morphologies on synaptic scaling. Studying different morphologies revealed that shorter, less branched trees perform better with respect to convergence rate, system's robustness, and scaling accuracy. Just as in toy neuron models, the three attributes are balanced such that improving one always worsens the others.

We have shown that a simple reduced-order model, like the ball-stick model captures the input-output behavior of the real morphology with sufficient accuracy to make accurate predictions on the neuron stability and other attributes. By capturing the dynamics of a highly complex system in essentially a reduced set parameters, the ball-stick model presents itself as a valuable analysis and prediction tool. This also justifies the use of toy neuron models in Chapters 6-8, for studying more complex neuronal processes.

- *Activity-dependent degradation has a bidirectional effect on performance*. In Section 4.2.1 we saw how variation in the degradation rates had the most pronounced effect on the robustness of the **CLSS** model (Figure 4.5b). In Chapter 6 we took this further by modeling degradation to be an activity-dependent process. We have shown that an adaptive degradation process has both a stabilizing and a destabilizing effect. The nature of this effect depends on the global set-point, local set-point, and synapse location. The stabilizing effect is attributed to the increase of dissipation in the trafficking system, which attenuates the phase-lag caused by the trafficking process. The destabilizing effect arises from the competitions between distributed controllers, and the global controller.

It is interesting to develop a comparison between the local action in the degradation mechanism (6.8) and the local action in the activation mechanism (3.8) of the **CLSS** model. A difference appears between the two mechanisms when we consider the robustness and accuracy tradeoff mediated by k_L, as shown in Figure 4.13. For the activation mechanism (3.8), varying k_L always mediates between the robustness of the closed loop system and accuracy. Conversely, this is not necessarily the case for the activation degradation mechanism (6.8) . This is due to the fact that (6.8) can impose either a stabilizing or a destabilizing effect. Therefore, it is possible that increasing k_L might deteriorates both attributes.

Despite their difference with regards to their influence on the tradeoffs, the success of both schemes on satisfying local demands depends on the compartment's location with

respect to the soma. The reservoir or receptors pool size is the limiting factor. Bigger reservoir, and hence earlier spatial access to the dendritic pool, is advantageous. For both mechanisms, the global set-point *fixes* the average concentration of functional cargo. Then, for the activation mechanism (3.8), the local activity (mediated by c_i in the **CLSS** model) drives the compartment's steady-state concentration of functional cargo. On the other hand, for the degradation mechanism (6.8), the local set-point $\bar{g}_i$ drives the compartment's steady-state concentration of functional cargo.

- *Nonlinear trafficking and fast cargo synthesis do not drastically alter the behavior of the CLSS model.* We showed in Chapter 7 that replacing the linear transport with a nonlinear one produces the same qualitative behavior as the **CLSS** model. However, crowding effects and rapid cargo synthesis increases the sensitivity of the closed loop system. This is evident by the emergence of oscillations, which ultimately led to the failure of homeostasis in the form of pathological oscillations. Therefore, a fast production of cargo, and hence an aggressive synaptic scaling process, can destabilize the system.

  In the **CLSS** model, replacing the trafficking of AMPARs with a nonlinear trafficking model will exacerbate the tradeoffs. Firstly, a nonlinear trafficking rate $v_f(c_i - m_i)$ is always slower than a linear rate v_f, except when a compartment is empty. Therefore, the transport mechanism is slower and hence less robust in terms of the stability margins.

  To overcome the limitation imposed by the nonlinear transport process, we explored the effectiveness of varying the timescale of cargo production. This has revealed that a slow cargo production is necessary for a robust regulation process. At the same time, our analysis has revealed that the system can withstand a substantial variation in the timescale, which conforms to the observations made in [168].

- *Activity-dependent growth improves the neuron performance.* In Chapter 8 we showed that the slow timescale of the growth process resulted in a filtering characteristic that allowed the neuron to withstand more aggressive synaptic scaling. It also mitigated the nonlinearities' effects that prevented the neuron from achieving its set-point by expanding and increasing compartments' sizes. The latter corresponds, physiologically, to forming new spines to increase the strength of existing connections. The setting resembled a situation where two distinct plasticity mechanisms coexisted to serve one objective.

  The activity-dependent growth in this chapter is connected to the parameter c_i, presented in the **CLSS** model in Chapters 3-5, which captured the capacity of synapses.

There, we used those (constant) parameters to model LTP or LTD events in arbitrary synapses of the neuron. As a result, varying c_i leads to varying the steady-state concentration of active AMPARs, or g_i^* (increasing c_i leads to increasing g_i^*, and vice versa). In the closed loop model of Chapter 8, however, the synapses play an active role in achieving homeostasis. Their strength varies in an activity-dependent manner as a result of the dynamic nature of compartments, since $c_i = c_i(t)$.

A structurally dynamic synaptic compartment $c_i(t)$ can significantly improve the performance of the neuron with respect to the three performance attributes. Activity-dependent growth increases the robustness of the system. As a result, if implemented in the **CLSS** model, the system will be able to withstand more aggressive scaling (higher k_G). Firstly, this will decrease the settling time. Secondly, the stability margin will not deteriorate as in the **CLSS**.

9.2 Experimental validation and predictions

We have performed an analytical and a computational study of regulation in single neurons throughout this thesis, and we have established a number of results, observations, and predictions. In this section, we propose a few experimental studies that can validate and confirm some of the results presented in the previous chapters.

- *The balance between adaptive activation of AMPARs and cargo synthesis.* In Chapters 3-5, two of the three free parameters were k_G and k_L. Recall that k_G is the feedback gain associated with the replenishment of total cargo in the system, while k_L is the feedback gain associated with the activation of protein at synaptic synaptic sites. We have used those two as "free parameters" to sweep through the tradeoffs. An intriguing question is the following: to what extent does a particular cell depend on global and local mechanisms, i.e. do all neurons (with their different morphologies) have the same dependence on k_G and k_L? An intuitive prediction is that, in large and branched cells, local action is more dominant than global control. As we have shown in Chapter 4, large cells cannot regulate predominantly with global control or instability arises. Conversely, smaller cells depend more heavily on global control. This is based on the observations we made about correlations between size and accuracy of synaptic scaling.

  This can be experimentally monitored and measured using a combination of experimental techniques, namely confocal microscopy and Total Internal Reflection Fluorescence Microscopy (TIRFM). One can then measure changes in neurite surface fluorescence

over time. Confocal microscopy is suitable for measuring long-distanced transport (e.g. trafficking along the dendritic tree), which is associated predominantly to the global controller, and hence indicative of the value of k_G. On the other hand, local action is associated with short-term transport (e.g. trafficking from the dendritic pool to the synaptic sites), taking place place in synaptic neck. Therefore, TIRFM is a suitable technique of recording for such a fine resolution process.

By measuring and monitoring the trafficking and volume rates obtained from these two experimental recordings, and by comparing them across the different morphologies, we would be able to have an idea on the effect of morphology on the balance between local and global feedback. We might perform a comparative study between a large and small neuron. For instance, as hypothesized, the small cell might exhibit a twofold increase in global AMPA production and no change in local AMPA activation with stimulation. A larger cell, which risks instability with high global regulation, might have no change in global production and a twofold change in local AMPA activation. Moreover, such a study would allow us to understand where approximately on the 2-D tradeoff plots each cell would be located.

- *Location-dependent effect of LTP.* In Chapter 5, we made a prediction that was guided by Nyquist stability criterion. The analysis suggests that the effect of LTP processes on the robustness of closed loop system is location-dependent. Specifically, we expect distal LTP to a elicit a stronger destabilizing effect than proximal LTP. This can be experimentally validated by chemically inducing LTP events at synapses in different proximal and distal locations across the dendritic tree. We then can tag ion channels (e.g. AMPARs) with Green Fluorescent Protein (GFP) and track the perturbations to the surface and internal pool of receptors. A larger change would correspond to a stronger destabilizing effect. We can again use TIRFM and confocal microscopy to quantify the changes in surface and internal AMPAR expression over time.

- *Effects of varying the synthesis rate on neuron's activity.* We explored how variations in the timescale of cargo production affected the closed loop system. To further explore this in real neurons, we can use experimental methods including viral and chemical transfections. By transfecting a plasmid, which is a small strand of DNA or RNA, one can insert a gene for a protein product into a cell. By modifying the promoter region of the gene, one can control how much/quickly the construct is created. We can compare the effects of glutamate receptors (AMPA or NMDA) with weak and strong promoters to assess how neuron activity changes with varying excitability. Further,

we can perform NMDA receptor knockout to eliminate endogenous production of receptors to study neuron activity with no NMDA receptors.

These experiments (transfections and gene knockouts), can be repeated and combined with other excitatory and inhibitory receptors in the neuron. Then, we can measure the trafficking rates of ion channels by tagging them with fluorescent probes. In this way, we would be able to monitor the transport rates of cargo while we vary the synthesis rates at the soma. Finally, the instability is expected to manifest itself in a periodic response on the transport rates.

9.3 Future research directions

Throughout this dissertation, we have adopted the following (physiological) assumptions:

1. The effect of morphology on the (instantaneous) membrane potential is captured by a single compartment model. Furthermore, we obtained a static relation of this quantity by imposing a quasi-steady-state assumption on a leaky-integrator neuron model.

2. All the synapses have the same power of influence on the average activity. This is captured by the averaged readout of the feedback signal.

Regarding the first assumption, and specifically for passive neurons, Rall derived equivalent cylinders of dendritic trees using cable theory- a diffusive PDE equation used to study the conservation of electrical charge [126]. What are the implications of coupling the cargo trafficking network with another layer that captures the variations in membrane potential across the network? The timescale nature of the changes in membrane potential allowed us to make a quasi-steady-state assumption. However, this assumption is pertained to the temporal variation of the membrane potential, but what about its spatial variations and effects?

The second assumption resonates with what is referred to as "synaptic democracy" [73, 130], which mitigates the location-dependent impact of synapse on the postsynaptic response. In support of this idea, there has been a number experimental studies that recorded an increase in AMPA receptors in distal sites in CA1 pyramidal neurons [8, 102, 138]. However, it is hard to generalize the case to all neuron types, as it was recorded to be the other way in other experimental studies [162]. This partly involves the trafficking mechanism as we saw earlier, and also studied by others in an open loop setting in axons [23]. As a follow up to our study of the performance tradeoffs in Chapters 3-5, the next logical step is to investigate the effects of a weighted averaged readout of synaptic functional cargo on the scaling performance of neurons.

The nature of the proposed set of models, and the use of control theoretic tools, naturally guide us towards the following set of questions:

- *Transport bottlenecks:* it was shown in [161] that low trafficking rates between two neighboring compartments can have a deteriorating effect on the settling time and cause severe delays to demand sites. This was done in a linear model. This same effect can be modeled in a nonlinear model by setting the compartment's capacity very low compared to the rest of the compartments in the network. This was addressed in an open loop setting in [12]. In the presence of different feedback loops, what is the possible qualitative behavior, and how is the performance affected?

- *Transcription bursts:* transcription and translation are discrete phenomena. This affects the modeling assumption that cargo synthesis is a continuous process. However, this might not have major consequences on the observations and conclusions presented here. The case that needs particular attention is when the concentrations are low, i.e. where stochasticity effects are pronounced. In this case, mean-field approximations are no longer valid and a different framework is therefore needed.

- *Growth on real morphology:* in chapter 8 we studied activity-dependent growth on a simple $1-$dimensional line. Beside varying a synapse size, structural changes encompass elongation and retracting, dendritic arborization, morphogenesis and branching [50, 84]. These features of growth require more sophisticated mathematical models with different compartmental growth rates. A starting model could be similar to the one presented in Chapter 6. In such a model, there will be a centralized controller regulating average activity, and a set of distributed controllers modeling individual compartmental growth.

- *Multiple species:* we assumed that scaling is primarily dependent on a single functional cargo. We have shown that the qualitative behavior is not significantly altered if another species is incorporated in the scaling process, such as arc mRNA. However, this was done under the assumption that the synthesis machinery is the same and the production was always split between the two species. A more biologically-relevant setting is the one in which each species had an independent synthesis machinery. This significantly complexify the model by changing the representation to a multi-input single-output (MISO) system. This paves the way also to tackle other interesting questions. For example, the coordination between AMPA and NMDA receptors in synaptic plasticity can be studied.

References

[1] Abbott, L. and Regehr, W. G. (2004). Synaptic computation. *Nature*, 431(7010):796–803.

[2] Abraham, W. C. and Bear, M. F. (1996). Metaplasticity: the plasticity of synaptic plasticity. *Trends in neurosciences*, 19(4):126–130.

[3] Alberts, B. (2008). Molecular biology of the cell.

[4] Aljaberi, S., Bellotti, A., O'Leary, T., and Forni, F. (2021). Dendritic trafficking regulation: homeostasis and distributed adaptation. *arXiv preprint arXiv:2103.15001*.

[5] Aljaberi, S., O'Leary, T., and Forni, F. (2019). Qualitative behavior and robustness of dendritic trafficking. *IEEE 58th Annual Conference on Decision and Control (CDC)*.

[6] Aljaberi, S., O'Leary, T., and Forni, F. (2020). Dendritic trafficking: synaptic scaling and structural plasticity. *arXiv preprint arXiv:2011.12067*.

[7] Alvarez-Castelao, B. and Schuman, E. M. (2015). The regulation of synaptic protein turnover. *Journal of Biological Chemistry*, 290(48):28623–28630.

[8] Andrásfalvy, B. K. and Magee, J. C. (2001). Distance-dependent increase in ampa receptor number in the dendrites of adult hippocampal ca1 pyramidal neurons. *Journal of Neuroscience*, 21(23):9151–9159.

[9] Aoto, J., Nam, C. I., Poon, M. M., Ting, P., and Chen, L. (2008). Synaptic signaling by all-trans retinoic acid in homeostatic synaptic plasticity. *Neuron*, 60(2):308–320.

[10] Armstrong, N., Mayer, M., and Gouaux, E. (2003). Tuning activation of the ampa-sensitive glur2 ion channel by genetic adjustment of agonist-induced conformational changes. *Proceedings of the National Academy of Sciences*, 100(10):5736–5741.

[11] Åström, K. J. and Murray, R. M. (2010). *Feedback systems: an introduction for scientists and engineers*. Princeton university press.

[12] Bar-Shalom, E., Ovseevich, A., and Margaliot, M. (2020). Ribosome flow model with different site sizes. *SIAM Journal on Applied Dynamical Systems*, 19(1):541–576.

[13] Bastin, G. and Guffens, V. (2006). Congestion control in compartmental network systems. *Systems & control letters*, 55(8):689–696.

[14] Bellotti, A., Aljaberi, S., Forni, F., and O'Leary, T. (2020). Neuronal morphology imposes a tradeoff between stability, accuracy and efficiency of synaptic scaling. In *29th Annual Computational Neuroscience Meeting (CNS* 2020)*.

[15] Ben-Ari, Y., Cherubini, E., Corradetti, R., and Gaiarsa, J. (1989). Giant synaptic potentials in immature rat ca3 hippocampal neurones. *The Journal of physiology*, 416(1):303–325.

[16] Bernard, C. (1879). *Leçons sur les phénomènes de la vie commune aux animaux et aux végétaux*, volume 2. Baillière.

[17] Bernard, C. (1957). *An introduction to the study of experimental medicine*, volume 400. Courier Corporation.

[18] Boyd, S., El Ghaoui, L., Feron, E., and Balakrishnan, V. (1994). *Linear Matrix Inequalities in System and Control Theory*. SIAM.

[19] Branco, T. and Staras, K. (2009). The probability of neurotransmitter release: variability and feedback control at single synapses. *Nature Reviews Neuroscience*, 10(5):373–383.

[20] Brauer, F. (2008). Compartmental models in epidemiology. In *Mathematical epidemiology*, pages 19–79. Springer.

[21] Bressloff, P. C. (2009). Cable theory of protein receptor trafficking in a dendritic tree. *Physical Review E*, 79(4):041904.

[22] Bressloff, P. C. (2014). *Stochastic processes in cell biology*, volume 41. Springer.

[23] Bressloff, P. C. and Levien, E. (2015). Synaptic democracy and vesicular transport in axons. *Physical review letters*, 114(16):168101.

[24] Brooks, H. A. and Bressloff, P. C. (2017). Turing mechanism for homeostatic control of synaptic density during c. elegans growth. *Physical Review E*, 96(1):012413.

[25] Buonomano, D. V. (2005). A learning rule for the emergence of stable dynamics and timing in recurrent networks. *Journal of Neurophysiology*, 94(4):2275–2283.

[26] Burbea, M., Dreier, L., Dittman, J. S., Grunwald, M. E., and Kaplan, J. M. (2002). Ubiquitin and ap180 regulate the abundance of glr-1 glutamate receptors at postsynaptic elements in c. elegans. *Neuron*, 35(1):107–120.

[27] Butz, M., Wörgötter, F., and van Ooyen, A. (2009). Activity-dependent structural plasticity. *Brain research reviews*, 60(2):287–305.

[28] Cannon, J. and Miller, P. (2016). Synaptic and intrinsic homeostasis cooperate to optimize single neuron response properties and tune integrator circuits. *Journal of neurophysiology*, 116(5):2004–2022.

[29] Cannon, W. B. (1929). Organization for physiological homeostasis. *Physiological reviews*, 9(3):399–431.

[30] Chicone, C. (2006). *Ordinary differential equations with applications*, volume 34. Springer Science & Business Media.

[31] Chowdhury, S., Shepherd, J. D., Okuno, H., Lyford, G., Petralia, R. S., Plath, N., Kuhl, D., Huganir, R. L., and Worley, P. F. (2006). Arc/arg3. 1 interacts with the endocytic machinery to regulate ampa receptor trafficking. *Neuron*, 52(3):445–459.

[32] Citri, A. and Malenka, R. C. (2008). Synaptic plasticity: multiple forms, functions, and mechanisms. *Neuropsychopharmacology*, 33(1):18–41.

[33] Como, G. (2017). On resilient control of dynamical flow networks. *Annual Reviews in Control*, 43:80–90.

[34] Coogan, S. and Arcak, M. (2015). A compartmental model for traffic networks and its dynamical behavior. *IEEE Transactions on Automatic Control*, 60(10):2698–2703.

[35] Coombs, I. D., MacLean, D. M., Jayaraman, V., Farrant, M., and Cull-Candy, S. G. (2017). Dual effects of tarp γ-2 on glutamate efficacy can account for ampa receptor autoinactivation. *Cell reports*, 20(5):1123–1135.

[36] Costa-Mattioli, M., Sossin, W. S., Klann, E., and Sonenberg, N. (2009). Translational control of long-lasting synaptic plasticity and memory. *Neuron*, 61(1):10–26.

[37] Cuntz, H., Forstner, F., Borst, A., and Häusser, M. (2010). One rule to grow them all: a general theory of neuronal branching and its practical application. *PLoS Comput Biol*, 6(8):e1000877.

[38] De Vos, K. J., Grierson, A. J., Ackerley, S., and Miller, C. C. (2008). Role of axonal transport in neurodegenerative diseases. *Annu. Rev. Neurosci.*, 31:151–173.

[39] Desai, N. S., Cudmore, R. H., Nelson, S. B., and Turrigiano, G. G. (2002). Critical periods for experience-dependent synaptic scaling in visual cortex. *Nature neuroscience*, 5(8):783–789.

[40] Desai, N. S., Rutherford, L. C., and Turrigiano, G. G. (1999). Plasticity in the intrinsic excitability of cortical pyramidal neurons. *Nature neuroscience*, 2(6):515–520.

[41] Desoer, C. and Vidyasagar, M. (1975). *Feedback Systems: Input-Output Properties*, volume 55 of *Classics in Applied Mathematics*. Society for Industrial and Applied Mathematics.

[42] DiAntonio, A., Haghighi, A. P., Portman, S. L., Lee, J. D., Amaranto, A. M., and Goodman, C. S. (2001). Ubiquitination-dependent mechanisms regulate synaptic growth and function. *Nature*, 412(6845):449–452.

[43] Dorrbaum, A. R., Kochen, L., Langer, J. D., and Schuman, E. M. (2018). Local and global influences on protein turnover in neurons and glia. *Elife*, 7:e34202.

[44] Doyle, M. and Kiebler, M. A. (2011). Mechanisms of dendritic mrna transport and its role in synaptic tagging. *The EMBO journal*, 30(17):3540–3552.

[45] Earnshaw, B. A. and Bressloff, P. C. (2006). Biophysical model of ampa receptor trafficking and its regulation during long-term potentiation/long-term depression. *Journal of Neuroscience*, 26(47):12362–12373.

[46] Earnshaw, B. A. and Bressloff, P. C. (2008). Modeling the role of lateral membrane diffusion in ampa receptor trafficking along a spiny dendrite. *Journal of computational neuroscience*, 25(2):366–389.

[47] Ehlers, M. D. (2000). Reinsertion or degradation of ampa receptors determined by activity-dependent endocytic sorting. *Neuron*, 28(2):511–525.

[48] Ehlers, M. D. (2003). Activity level controls postsynaptic composition and signaling via the ubiquitin-proteasome system. *Nature neuroscience*, 6(3):231–242.

[49] Eisenbach, M. (2007). Chemotaxis. *Wiley Encyclopedia of Chemical Biology*, pages 1–8.

[50] Emoto, K. (2012). Signaling mechanisms that coordinate the development and maintenance of dendritic fields. *Current opinion in neurobiology*, 22(5):805–811.

[51] Ewers, H., Tada, T., Petersen, J. D., Racz, B., Sheng, M., and Choquet, D. (2014). A septin-dependent diffusion barrier at dendritic spine necks. *PloS one*, 9(12):e113916.

[52] Farina, L. and Rinaldi, S. (2000). *Positive linear systems: theory and applications*. Pure and applied mathematics (John Wiley & Sons). Wiley.

[53] Félix, M.-A. and Wagner, A. (2008). Robustness and evolution: concepts, insights and challenges from a developmental model system. *Heredity*, 100(2):132–140.

[54] Fernandes, D. and Carvalho, A. L. (2016). Mechanisms of homeostatic plasticity in the excitatory synapse. *Journal of neurochemistry*, 139(6):973–996.

[55] Fernandez-Moya, S. M., Bauer, K. E., and Kiebler, M. A. (2014). Meet the players: local translation at the synapse. *Frontiers in molecular neuroscience*, 7:84.

[56] Fonkeu, Y., Kraynyukova, N., Hafner, A.-S., Kochen, L., Sartori, F., Schuman, E. M., and Tchumatchenko, T. (2019). How mRNA localization and protein synthesis sites influence dendritic protein distribution and dynamics. *Neuron*, 103(6):1109–1122.

[57] Forni, F. and Sepulchre, R. (2013). A differential Lyapunov framework for contraction analysis. *IEEE Transactions on Automatic Control*, 59(3):614–628.

[58] Forni, F. and Sepulchre, R. (2019). Differential dissipativity theory for dominance analysis. *IEEE Transactions on Automatic Control*, 64(6):2340–2351.

[59] Giachello, C. N. and Baines, R. A. (2017). Regulation of motoneuron excitability and the setting of homeostatic limits. *Current opinion in neurobiology*, 43:1–6.

[60] Glock, C., Heumüller, M., and Schuman, E. M. (2017). mrna transport & local translation in neurons. *Current opinion in neurobiology*, 45:169–177.

[61] Goel, A., Jiang, B., Xu, L. W., Song, L., Kirkwood, A., and Lee, H.-K. (2006). Cross-modal regulation of synaptic ampa receptors in primary sensory cortices by visual experience. *Nature neuroscience*, 9(8):1001–1003.

[62] Goldberg, A. L. et al. (1998). Proteasome inhibitors: valuable new tools for cell biologists. *Trends in cell biology*, 8(10):397–403.

[63] Golowasch, J., Casey, M., Abbott, L., and Marder, E. (1999). Network stability from activity-dependent regulation of neuronal conductances. *Neural Computation*, 11(5):1079–1096.

[64] Golub, G. H. et al. (1996). Cf vanloan, matrix computations. *The Johns Hopkins*.

[65] Graham, B. P. and Van Ooyen, A. (2006). Mathematical modelling and numerical simulation of the morphological development of neurons. *BMC neuroscience*, 7(S1):S9.

[66] Grant, M. and Boyd, S. (2014). Cvx: Matlab software for disciplined convex programming, version 2.1.

[67] Greengard, P. (2001). The neurobiology of slow synaptic transmission. *Science*, 294(5544):1024–1030.

[68] Greenhill, S. D., Ranson, A., and Fox, K. (2015). Hebbian and homeostatic plasticity mechanisms in regular spiking and intrinsic bursting cells of cortical layer 5. *Neuron*, 88(3):539–552.

[69] Greer, P. L., Hanayama, R., Bloodgood, B. L., Mardinly, A. R., Lipton, D. M., Flavell, S. W., Kim, T.-K., Griffith, E. C., Waldon, Z., Maehr, R., et al. (2010). The angelman syndrome protein ube3a regulates synapse development by ubiquitinating arc. *Cell*, 140(5):704–716.

[70] Haddad, W. M., Chellaboina, V., and Hui, Q. (2010). *Nonnegative and compartmental dynamical systems*. Princeton University Press.

[71] Hancock, W. O. (2014). Bidirectional cargo transport: moving beyond tug of war. *Nature reviews Molecular cell biology*, 15(9):615–628.

[72] Harris, K. M. (1999). Calcium from internal stores modifies dendritic spine shape. *Proceedings of the National Academy of Sciences*, 96(22):12213–12215.

[73] Häusser, M. (2001). Synaptic function: dendritic democracy. *Current Biology*, 11(1):R10–R12.

[74] Hebb, D. O. (1949). *The organization of behavior: a neuropsychological theory*. J. Wiley; Chapman & Hall.

[75] Hegde, A. N., Inokuchi, K., Pei, W., Casadio, A., Ghirardi, M., Chain, D. G., Martin, K. C., Kandel, E. R., and Schwartz, J. H. (1997). Ubiquitin c-terminal hydrolase is an immediate-early gene essential for long-term facilitation in aplysia. *Cell*, 89(1):115–126.

[76] Hely, T. A., Graham, B., and Van Ooyen, A. (2001). A computational model of dendrite elongation and branching based on map2 phosphorylation. *Journal of theoretical biology*, 210(3):375–384.

[77] Henley, J. M. and Wilkinson, K. A. (2013). Ampa receptor trafficking and the mechanisms underlying synaptic plasticity and cognitive aging. *Dialogues in clinical neuroscience*, 15(1):11.

[78] Henley, J. M. and Wilkinson, K. A. (2016). Synaptic ampa receptor composition in development, plasticity and disease. *Nature Reviews Neuroscience*, 17(6):337–350.

[79] Ho, V. M., Lee, J.-A., and Martin, K. C. (2011). The cell biology of synaptic plasticity. *Science*, 334(6056):623–628.

[80] Huang, Y.-Y., Colino, A., Selig, D. K., and Malenka, R. C. (1992). The influence of prior synaptic activity on the induction of long-term potentiation. *Science*, 255(5045):730–733.

[81] Ibata, K., Sun, Q., and Turrigiano, G. G. (2008). Rapid synaptic scaling induced by changes in postsynaptic firing. *Neuron*, 57(6):819–826.

[82] Jacob, F. and Monod, J. (1961). Genetic regulatory mechanisms in the synthesis of proteins. *Journal of molecular biology*, 3(3):318–356.

[83] Jacquez, J. A. and Simon, C. P. (1993). Qualitative theory of compartmental systems. *Siam Review*, 35(1):43–79.

[84] Jan, Y.-N. and Jan, L. Y. (2010). Branching out: mechanisms of dendritic arborization. *Nature Reviews Neuroscience*, 11(5):316–328.

[85] Jiang, Y.-h., Armstrong, D., Albrecht, U., Atkins, C. M., Noebels, J. L., Eichele, G., Sweatt, J. D., and Beaudet, A. L. (1998). Mutation of the angelman ubiquitin ligase in mice causes increased cytoplasmic p53 and deficits of contextual learning and long-term potentiation. *Neuron*, 21(4):799–811.

[86] Jones, R. (2012). *Principles of biological regulation: an introduction to feedback systems*. Elsevier.

[87] Kaneko, M., Stellwagen, D., Malenka, R. C., and Stryker, M. P. (2008). Tumor necrosis factor-α mediates one component of competitive, experience-dependent plasticity in developing visual cortex. *Neuron*, 58(5):673–680.

[88] Kapitein, L. C. and Hoogenraad, C. C. (2011). Which way to go? cytoskeletal organization and polarized transport in neurons. *Molecular and Cellular Neuroscience*, 46(1):9–20.

[89] Kater, S. B., Mattson, M. P., Cohan, C., and Connor, J. (1988). Calcium regulation of the neuronal growth cone. *Trends in neurosciences*, 11(7):315–321.

[90] Khalil, H. K. (2002). Nonlinear systems. *Upper Saddle River*.

[91] Khan, S., Reese, T. S., Rajpoot, N., and Shabbir, A. (2012). Spatiotemporal maps of camkii in dendritic spines. *Journal of computational neuroscience*, 33(1):123–139.

[92] Kitano, H. and Oda, K. (2006). Robustness trade-offs and host–microbial symbiosis in the immune system. *Molecular systems biology*, 2(1):2006–0022.

[93] Kneussel, M. and Wagner, W. (2013). Myosin motors at neuronal synapses: drivers of membrane transport and actin dynamics. *Nature Reviews Neuroscience*, 14(4):233–247.

[94] Kullmann, D. M. and Lamsa, K. P. (2007). Long-term synaptic plasticity in hippocampal interneurons. *Nature Reviews Neuroscience*, 8(9):687–699.

[95] Lee, I. and Kesner, R. P. (2004). Differential contributions of dorsal hippocampal subregions to memory acquisition and retrieval in contextual fear-conditioning. *Hippocampus*, 14(3):301–310.

[96] LeMasson, G., Marder, E., and Abbott, L. (1993). Activity-dependent regulation of conductances in model neurons. *Science*, 259(5103):1915–1917.

[97] Li, L., Gainey, M. A., Goldbeck, J. E., and Feldman, D. E. (2014). Rapid homeostasis by disinhibition during whisker map plasticity. *Proceedings of the National Academy of Sciences*, 111(4):1616–1621.

[98] Lindsay, K., Ogden, J., Halliday, D., and Rosenberg, J. (1999). An introduction to the principles of neuronal modelling. In *Modern techniques in neuroscience research*, pages 213–306. Springer.

[99] Lisman, J. (2017). Glutamatergic synapses are structurally and biochemically complex because of multiple plasticity processes: long-term potentiation, long-term depression, short-term potentiation and scaling. *Philosophical Transactions of the Royal Society B: Biological Sciences*, 372(1715):20160260.

[100] Lissin, D. V., Gomperts, S. N., Carroll, R. C., Christine, C. W., Kalman, D., Kitamura, M., Hardy, S., Nicoll, R. A., Malenka, R. C., and Von Zastrow, M. (1998). Activity differentially regulates the surface expression of synaptic ampa and nmda glutamate receptors. *Proceedings of the National Academy of Sciences*, 95(12):7097–7102.

[101] Lu, H. E., MacGillavry, H. D., Frost, N. A., and Blanpied, T. A. (2014). Multiple spatial and kinetic subpopulations of camkii in spines and dendrites as resolved by single-molecule tracking palm. *Journal of Neuroscience*, 34(22):7600–7610.

[102] Magee, J. C. and Cook, E. P. (2000). Somatic epsp amplitude is independent of synapse location in hippocampal pyramidal neurons. *Nature neuroscience*, 3(9):895–903.

[103] Malenka, R. C. and Bear, M. F. (2004). Ltp and ltd: an embarrassment of riches. *Neuron*, 44(1):5–21.

[104] Malenka, R. C. and Nicoll, R. A. (1999). Long-term potentiation–a decade of progress? *Science*, 285(5435):1870–1874.

[105] Malinow, R. and Malenka, R. C. (2002). Ampa receptor trafficking and synaptic plasticity. *Annual review of neuroscience*, 25(1):103–126.

[106] May, R. M. (2019). *Stability and complexity in model ecosystems*. Princeton university press.

[107] McAllister, A. K. (2000). Cellular and molecular mechanisms of dendrite growth. *Cerebral cortex*, 10(10):963–973.

[108] McLean, D. R., van Ooyen, A., and Graham, B. P. (2004). Continuum model for tubulin-driven neurite elongation. *Neurocomputing*, 58:511–516.

[109] Miranda-Villatoro, F. A., Forni, F., and Sepulchre, R. J. (2018). Analysis of lur'e dominant systems in the frequency domain. *Automatica*, 98:76–85.

[110] Müller, M. J., Klumpp, S., and Lipowsky, R. (2008). Tug-of-war as a cooperative mechanism for bidirectional cargo transport by molecular motors. *Proceedings of the National Academy of Sciences*, 105(12):4609–4614.

[111] Murphey, R. K. and Godenschwege, T. A. (2002). New roles for ubiquitin in the assembly and function of neuronal circuits. *Neuron*, 36(1):5–8.

[112] Nakazawa, K., Sun, L. D., Quirk, M. C., Rondi-Reig, L., Wilson, M. A., and Tonegawa, S. (2003). Hippocampal ca3 nmda receptors are crucial for memory acquisition of one-time experience. *Neuron*, 38(2):305–315.

[113] Nash, J. E., Appleby, V. J., Corrêa, S. A., Wu, H., Fitzjohn, S. M., Garner, C. C., Collingridge, G. L., and Molnár, E. (2010). Disruption of the interaction between myosin vi and sap97 is associated with a reduction in the number of ampars at hippocampal synapses. *Journal of neurochemistry*, 112(3):677–690.

[114] Newpher, T. M. and Ehlers, M. D. (2008). Glutamate receptor dynamics in dendritic microdomains. *Neuron*, 58(4):472–497.

[115] O'Leary, T., van Rossum, M. C., and Wyllie, D. J. (2010). Homeostasis of intrinsic excitability in hippocampal neurones: dynamics and mechanism of the response to chronic depolarization. *The Journal of physiology*, 588(1):157–170.

[116] O'Leary, T., Williams, A. H., Caplan, J. S., and Marder, E. (2013). Correlations in ion channel expression emerge from homeostatic tuning rules. *Proceedings of the National Academy of Sciences*, 110(28):E2645–E2654.

[117] O'Leary, T., Williams, A. H., Franci, A., and Marder, E. (2014). Cell types, network homeostasis, and pathological compensation from a biologically plausible ion channel expression model. *Neuron*, 82(4):809–821.

[118] O'Leary, T. and Wyllie, D. J. (2011). Neuronal homeostasis: time for a change? *The Journal of physiology*, 589(20):4811–4826.

[119] Osterweil, E., Wells, D. G., and Mooseker, M. S. (2005). A role for myosin vi in postsynaptic structure and glutamate receptor endocytosis. *The Journal of cell biology*, 168(2):329–338.

[120] O'Brien, R. J., Kamboj, S., Ehlers, M. D., Rosen, K. R., Fischbach, G. D., and Huganir, R. L. (1998). Activity-dependent modulation of synaptic ampa receptor accumulation. *Neuron*, 21(5):1067–1078.

[121] Padoan, A., Forni, F., and Sepulchre, R. (2019). The h infinity,p norm as the differential gain of a p-dominant system. *Accepted, 58th IEEE Annual Conference on Decision and Control (CDC)*.

[122] Park, H. Y., Lim, H., Yoon, Y. J., Follenzi, A., Nwokafor, C., Lopez-Jones, M., Meng, X., and Singer, R. H. (2014). Visualization of dynamics of single endogenous mrna labeled in live mouse. *Science*, 343(6169):422–424.

[123] Pérez-Otaño, I. and Ehlers, M. D. (2005). Homeostatic plasticity and nmda receptor trafficking. *Trends in neurosciences*, 28(5):229–238.

[124] Pozo, K. and Goda, Y. (2010). Unraveling mechanisms of homeostatic synaptic plasticity. *Neuron*, 66(3):337–351.

[125] Rajewsky, N., Santen, L., Schadschneider, A., and Schreckenberg, M. (1998). The asymmetric exclusion process: Comparison of update procedures. *Journal of statistical physics*, 92(1-2):151–194.

[126] Rall, W. (1962). Theory of physiological properties of dendrites. *Annals of the New York Academy of Sciences*, 96(4):1071–1092.

[127] Reuveni, S., Meilijson, I., Kupiec, M., Ruppin, E., and Tuller, T. (2011). Genome-scale analysis of translation elongation with a ribosome flow model. *PLoS computational biology*, 7(9):e1002127.

[128] Rittenhouse, C. D., Shouval, H. Z., Paradiso, M. A., and Bear, M. F. (1999). Monocular deprivation induces homosynaptic long-term depression in visual cortex. *Nature*, 397(6717):347–350.

[129] Rose, T., Jaepel, J., Hübener, M., and Bonhoeffer, T. (2016). Cell-specific restoration of stimulus preference after monocular deprivation in the visual cortex. *Science*, 352(6291):1319–1322.

[130] Rumsey, C. C. and Abbott, L. F. (2006). Synaptic democracy in active dendrites. *Journal of Neurophysiology*, 96(5):2307–2318.

[131] Ryu, J., Liu, L., Wong, T. P., Wu, D. C., Burette, A., Weinberg, R., Wang, Y. T., and Sheng, M. (2006). A critical role for myosin iib in dendritic spine morphology and synaptic function. *Neuron*, 49(2):175–182.

[132] Sajikumar, S., Morris, R. G., and Korte, M. (2014). Competition between recently potentiated synaptic inputs reveals a winner-take-all phase of synaptic tagging and capture. *Proceedings of the National Academy of Sciences*, 111(33):12217–12221.

[133] Schilling, K., Dickinson, M. H., Connor, J. A., and Morgan, J. I. (1991). Electrical activity in cerebellar cultures determines purkinje cell dendritic growth patterns. *Neuron*, 7(6):891–902.

[134] Schnell, E., Sizemore, M., Karimzadegan, S., Chen, L., Bredt, D. S., and Nicoll, R. A. (2002). Direct interactions between psd-95 and stargazin control synaptic ampa receptor number. *Proceedings of the National Academy of Sciences*, 99(21):13902–13907.

[135] Schwanhausser, B., Busse, D., Li, N., Dittmar, G., Schuchhardt, J., Wolf, J., Chen, W., and Selbach, M. (2011). Global quantification of mammalian gene expression control. *Nature*, 473(7347):337–342.

[136] Siegel, M., Marder, E., and Abbott, L. (1994). Activity-dependent current distributions in model neurons. *Proceedings of the National Academy of Sciences*, 91(24):11308–11312.

[137] Smith, H. L. (2008). *Monotone dynamical systems: an introduction to the theory of competitive and cooperative systems: an introduction to the theory of competitive and cooperative systems*. Number 41. American Mathematical Soc.

[138] Smith, M. A., Ellis-Davies, G. C., and Magee, J. C. (2003). Mechanism of the distance-dependent scaling of schaffer collateral synapses in rat ca1 pyramidal neurons. *The Journal of physiology*, 548(1):245–258.

[139] Sorra, K. E. and Harris, K. M. (2000). Overview on the structure, composition, function, development, and plasticity of hippocampal dendritic spines. *Hippocampus*, 10(5):501–511.

[140] Spohn, H. (2012). *Large scale dynamics of interacting particles*. Springer Science & Business Media.

[141] Steward, O., Farris, S., Pirbhoy, P. S., Darnell, J., and Driesche, S. J. V. (2015). Localization and local translation of arc/arg3. 1 mrna at synapses: some observations and paradoxes. *Frontiers in molecular neuroscience*, 7:101.

[142] Steward, O., Wallace, C. S., Lyford, G. L., and Worley, P. F. (1998). Synaptic activation causes the mrna for the ieg arc to localize selectively near activated postsynaptic sites on dendrites. *Neuron*, 21(4):741–751.

[143] Sulston, J. E. and Horvitz, H. R. (1977). Post-embryonic cell lineages of the nematode, caenorhabditis elegans. *Developmental biology*, 56(1):110–156.

[144] Suszkiw, J., O'leary, M., Murawsky, M., and Wang, T. (1986). Presynaptic calcium channels in rat cortical synaptosomes: fast-kinetics of phasic calcium influx, channel inactivation, and relationship to nitrendipine receptors. *Journal of Neuroscience*, 6(5):1349–1357.

[145] Tailby, C., Wright, L. L., Metha, A. B., and Calford, M. B. (2005). Activity-dependent maintenance and growth of dendrites in adult cortex. *Proceedings of the National Academy of Sciences*, 102(12):4631–4636.

[146] Tetzlaff, C., Kolodziejski, C., Markelic, I., and Wörgötter, F. (2012). Time scales of memory, learning, and plasticity. *Biological cybernetics*, 106(11):715–726.

[147] Thiagarajan, T. C., Lindskog, M., and Tsien, R. W. (2005). Adaptation to synaptic inactivity in hippocampal neurons. *Neuron*, 47(5):725–737.

[148] Triesch, J., Vo, A. D., and Hafner, A.-S. (2018). Competition for synaptic building blocks shapes synaptic plasticity. *Elife*, 7:e37836.

[149] Turrigiano, G. (2011). Too many cooks? intrinsic and synaptic homeostatic mechanisms in cortical circuit refinement. *Annual review of neuroscience*, 34:89–103.

[150] Turrigiano, G., Abbott, L., and Marder, E. (1994). Activity-dependent changes in the intrinsic properties of cultured neurons. *Science*, 264(5161):974–977.

[151] Turrigiano, G. G. (2008). The self-tuning neuron: synaptic scaling of excitatory synapses. *Cell*, 135(3):422–435.

[152] Turrigiano, G. G., Leslie, K. R., Desai, N. S., Rutherford, L. C., and Nelson, S. B. (1998). Activity-dependent scaling of quantal amplitude in neocortical neurons. *Nature*, 391(6670):892–896.

[153] Turrigiano, G. G. and Nelson, S. B. (2004). Homeostatic plasticity in the developing nervous system. *Nature reviews neuroscience*, 5(2):97–107.

[154] Tushev, G., Glock, C., Heumuller, M., Biever, A., Jovanovic, M., and Schuman, E. M. (2018). Alternative 3 utrs modify the localization, regulatory potential, stability, and plasticity of mrnas in neuronal compartments. *Neuron*, 98(3):495–511.

[155] van der Schaft, A. (1999). *L_2-Gain and Passivity in Nonlinear Control*. Springer-Verlag New York, Inc., Secaucus, N.J., USA, second edition.

[156] Van Huizen, F., Romijn, H., and Habets, A. (1985). Synaptogenesis in rat cerebral cortex cultures is affected during chronic blockade of spontaneous bioelectric activity by tetrodotoxin. *Developmental Brain Research*, 19(1):67–80.

[157] van Ooyen, A. (2017). Network formation through activity-dependent neurite outgrowth: a review of a simple model of homeostatic structural plasticity. In *The Rewiring Brain*, pages 95–121. Elsevier.

[158] Wallace, C. S., Lyford, G. L., Worley, P. F., and Steward, O. (1998). Differential intracellular sorting of immediate early gene mrnas depends on signals in the mrna sequence. *Journal of Neuroscience*, 18(1):26–35.

[159] Wang, H. and Wagner, J. J. (1999). Priming-induced shift in synaptic plasticity in the rat hippocampus. *Journal of neurophysiology*, 82(4):2024–2028.

[160] Watt, A. J., Van Rossum, M. C., MacLeod, K. M., Nelson, S. B., and Turrigiano, G. G. (2000). Activity coregulates quantal ampa and nmda currents at neocortical synapses. *Neuron*, 26(3):659–670.

[161] Williams, A. H., O'donnell, C., Sejnowski, T. J., and O'leary, T. (2016). Dendritic trafficking faces physiologically critical speed-precision tradeoffs. *Elife*, 5:e20556.

[162] Williams, S. R. and Stuart, G. J. (2002). Dependence of epsp efficacy on synapse location in neocortical pyramidal neurons. *Science*, 295(5561):1907–1910.

[163] Willshaw, D. and Price, D. (2003). Models for topographic map formation. *Modeling Neural Development*, pages 213–244.

[164] Wilson, S. M., Bhattacharyya, B., Rachel, R. A., Coppola, V., Tessarollo, L., Householder, D. B., Fletcher, C. F., Miller, R. J., Copeland, N. G., and Jenkins, N. A. (2002). Synaptic defects in ataxia mice result from a mutation in usp14, encoding a ubiquitin-specific protease. *Nature genetics*, 32(3):420–425.

[165] Wu, H., Nash, J. E., Zamorano, P., and Garner, C. C. (2002). Interaction of sap97 with minus-end-directed actin motor myosin vi: implications for ampa receptor trafficking. *Journal of Biological Chemistry*, 277(34):30928–30934.

[166] Yeung, L. C., Shouval, H. Z., Blais, B. S., and Cooper, L. N. (2004). Synaptic homeostasis and input selectivity follow from a calcium-dependent plasticity model. *Proceedings of the National Academy of Sciences*, 101(41):14943–14948.

[167] Zarai, Y., Margaliot, M., and Tuller, T. (2017). A deterministic mathematical model for bidirectional excluded flow with langmuir kinetics. *PloS one*, 12(8):e0182178.

[168] Zenke, F. and Gerstner, W. (2017). Hebbian plasticity requires compensatory processes on multiple timescales. *Philosophical Transactions of the Royal Society B: Biological Sciences*, 372(1715):20160259.

[169] Zhang, W., Robert, A., Vogensen, S. B., and Howe, J. R. (2006). The relationship between agonist potency and ampa receptor kinetics. *Biophysical Journal*, 91(4):1336–1346.

[170] Zhou, K., Doyle, J., and Glover, K. (1995). *Robust and optimal control*. Prentice Hall.